PRIMA DDL & AOS Project

ARC
EPFL
CSEM
MPIA Heidelberg
Observatoire de Genève
Landessternwarte Heidelberg

Astrometric Survey for Extra-Solar Planets with PRIMA

Astrometric Dispersion Correction

Doc. No.	UL-TRE-AOS-15753-0010
Issue	1.2.311
Date	November 7, 2007

Prepared Richard J. Mathar November 7, 2007

Signature

Approved

Signature

Released

Signature

This page was intentionally left almost blank

Change Record

Issue	Date	Section/Parag. affected	Reason/Initiation/Documents/Remarks
0.1	07-Jun-2004	all	created
1.1.127	7-May-2006	Tab. 4	added
1.1.129	9-May-2006	Tab. 2, Ref. [181]	added
1.1.134	14-May-2006	Tab. 6	added
		Sec. 2	removed literature to liquid and solid state
1.1.304	31-Oct-2006	Ref. [103]	added; removed equivalent parts of Sec 2
1.1.313	9-Nov-2006	Tab. 5	added
1.1.326	22-Nov-2006	cover page logo	changed
1.1.341	7-Dec-2006	Ref. [170]	added
1.2.079	20-Mar-2007	Fig. 33,34,35	updated,added
1.2.228	16-Aug-2007	Fig. 34	updated
1.2.232	20-Aug-2007	Fig. 45	added
1.2.233	21-Aug-2007	Fig. 46,47	added
1.2.236	24-Aug-2007	Sec. 6.3	added from [104]
		Refs. [104, 105]	added
1.2.242	30-Aug-2007	Ref. [147]	added
1.2.248	5-Sep-2007	Ref. [61]	added
1.2.248	7-Nov-2007	Sec. 6.5	back in from [104]

Contents

List of Figures

List of Tables

1 OVERVIEW

1.1 Scope of the Document

PRIMA [30, 31, 54, 73, 128, 129, 130] at the VLTI [37][177, §4.8] aims at measuring relative distances on the sky down to the order of 10 μarcsec ($7.7 \cdot 10^{-12}$ of the full circle). This tilt angle scales to relative optical path differences of the order of 5 nm at prototypical baselines between two apertures [8][113, Fig. 2], and eventually it is the knowledge of the optical path differences in the earth-bound interferometric laboratory to this precision which allows to reduce any fringe packet location to (relative) positions on the sky.

Other instruments envisage to remove disturbing effects of micro-turbulence, wavelength-dependent indexes of refraction by placing much of the beams from the telescopes to the detector in vacuum tubes [132]; turbulent layers in the atmosphere [133] are not under active control unless the interferometer is space-based [165]. With the VLTI, however, the entire path of the PS and SS leads through air except, optionally, some fraction of a meter of the DDL vacuum vessels [72, 74, 168].

The PRIMA metrology laser system provides real-time information at a wavelength of 1.319 μm [82, 83, 84, 139] (similar to [56]), and its optical path length is to be extrapolated to the K band. Since the closed loop online monitoring of the DDL positions is based on HeNe metrology at 633 nm [168], extrapolation into the VIS may be needed for the ICS.

Sec. 2 is a terse review of air refractivity with some attention paid to the variable water content. The conclusions are the same as drawn before [164].

Sec. 3 summarizes the simple (linear) error theory for the error in the optical path difference due to refractivity of the non-evacuated delay lines (see [72] for the refractivity of the DDL windows), and calculates the parabolic beam bending in the light ducts and in the delay line tunnel [48] induced by transverse air density gradients.

Sec. 4 summarizes the basics of the K-prism design in terms of depolarization, both with respect to introducing phase changes designed to be 90° and with respect to rotations of the plane of polarization of the electrical field vector.

Sec. 5 looks at effects caused by the "lateral" atmospheric diffraction and earth curvature [58]. It includes some comments how formulas like $D = b \sin z$ inherited from planar trigonometry loose their meaning in interferometry for non-infinite earth radii, because the concept of a local zenith angle z becomes fuzzy. It also calculates prototypical atmospheric magnification factors as the geometric baseline on the ground is "lifted" to the equivalent "effective" baseline above the atmosphere.

Some closely related themes are left aside:

- Equivalent errors from subtleties of precision motion of the DDL (thermal expansion, noise and nonlinearities in the actuators...) are discussed elsewhere [29, 112, 168]. See [137] on the theme of loss of polarization through the atmosphere, [34, 49, 50, 51, 70, 77, 83] for a characterization of the tunnel seeing, [43, 68, 69] for parameters of the anticipated structural stability of the ATs.
- The influence of dispersion on the visibility estimate is not discussed here; it might become important if one tries to calibrate the baseline by drawing a visibility curve over time, as the visibility measured under wide-band conditions may be squeezed as a function of the star's altitude [75, 159].

- The possibility of working in the H band, [13, p. 8], will be ignored for what follows.

New versions of this text are made available at the URL http://www.strw.leidenuniv.nl/~mathar/public/UL-TRE-AOS-15753-0010.pdf.

This work has been supported by the NWO VICI grant of 15-6-2003 "Optical Interferometry: A new Method for Studies of Extrasolar Planets" to AQ.

1.2 Tools and Technologies Required

1.2.1 Data products

The raw FITS files [9, 65] should contain one "average" snapshot of both metrology readings (path lengths in the metrology laser light) per detector readout. Temporary storage somewhere in a computer memory as foreseen in [78] is insufficient for postprocessing.

The PSD covering the frequency domain above these detector readout cycles should be provided a few times per night, at a frequency where the micro-climate in the air paths is supposed to change. These ought be derived from the high frequent metrology readings to include the air turbulence and all movements of optical surfaces. Low-frequent PSDs (for instance reaching to a cutoff at 0.01 Hz [98]) are probably of no interest.

1.2.2 Baseline calibration

The atmospheric effects on the effective interferometric baseline described in Sec. 5 ought already be well known by the ongoing VLTI baseline calibration programs, since they are by no means special to PRIMA. We request that the available results are provided by ESO through documentation. The available description in a conference proceeding [31] is to fuzzy to be of any value, or seems to ignore these effects altogether.

1.3 Documents

[1] Akeson, R. L., Swain, M. R., & Colavita, M. M. 2000, in Interferometry in Optical Astronomy, edited by P. J. Lena, & A. Quirrenbach (Int. Soc. Optical Engineering), vol. 4006 of Proc. SPIE, 321

[2] Albrecht, S. 2004, GENIE T/RH sensor project, Installation of the Humidity Sensors at the VLTI. VLT-TRE-NEV-15846-xxxx

[3] Albrecht, S., Bakker, E. J., de Jong, J. A., Tubbs, R. N., Meisner, J., & le Poole, R. 2004, in New Frontiers in Stellar Interferometry, edited by W. A. Traub (Int. Soc. Optical Engineering), vol. 5491 of Proc. SPIE, 1266

[4] Andolfato, L., & Karban, R. 2007, VLTI PRIMA Supervisor Software Interface Control Document. VLT-ICD-ESO-15736-3060

[5] Auer, L. H., & Standish, E. M. 2000, AJ, 119, 2472

[6] Azzam, R. M. A. 2004, J. Opt. Soc. Am. A, 21, 1559

[7] Baillis, D., Pilon, L., Randrianalisoa, H., Gomez, R., & Viskanta, R. 2004, J. Opt. Soc. Am. A, 21, 149. Note the sign error in front of the first Sellmeier term in Eq. (15)

[8] Bakker, E. J., et al. 2004, Astrometric Survey for Extra-Solar Planets with PRIMA, PRIMA Astrometry Operations and Software: technical proposal. VLT-PLA-AOS-15750-0001

[9] Ballester, P., & Sabet, C. 2002, VLT Interferometer VLTI Data Interface Control Document. VLT-SPE-ESO-15000-2764

[10] Barrell, H., & Sears, J. E. 1939, Phil. Trans. R. Soc. A, 238, 1

[11] Birch, K. P. 1991, J. Opt. Soc. Am. A, 8, 647

[12] Birch, K. P., Downs, M. J., & Ferriss, D. H. 1988, J. Phys. E, 21, 690

[13] Bogo, W., Busso, A., Mottini, S., Nicolini, G., & Massone, G. 2003, PRIMA FSU, Design and analysis report. VLT-TRE-ALS-15740-0004. The abscissa units in Fig 4.3-11 should be μm, not nm.

[14] Bönsch, G., & Potulski, E. 1998, Metrologia, 35, 133

[15] Born, M., & Wolf, E. 1999, Principles of Optics (Cambridge: Cambridge University Press), 7th ed.

[16] Bouché, C., Leitner, A., & Sass, F. 1955, Dubbels Taschenbuch für den Maschinenbau (Berlin, Göttingen: Springer)

[17] Brunthaler, A. 2004, Ph.D. thesis, Rheinische Friedrich-Wilhelms-Universität Bonn

[18] Brunthaler, A., Reid, M. J., & Falcke, H. 2005, in Future Directions in High Resolution Astronomy: the 10th Anniversary of the VLBA (Astronomical Society of the Pacific), no. 340 in ASP Conference Series, 455

[19] Chan, W. F., Cooper, G., Guo, X., & Brion, C. E. 1992, Phys. Rev. A, 45, 1420

[20] Chan, W. F., Cooper, G., Guo, X., Burton, G. R., & Brion, C. E. 1992, Phys. Rev. A, 46, 149. E: [21]

[21] — 1993, Phys. Rev. A, 48, 858

[22] Ciddor, P. E. 1996, Appl. Opt., 35, 1566

[23] Cissik, J. H., Johnson, R. E., & Rokosch, D. K. 1972, J. Appl. Physiology, 32, 155

[24] Colavita, M. M., Shao, M., & Staelin, D. H. 1987, Appl. Opt., 26, 4113

[25] Colavita, M. M., Swain, M. R., Akeson, R. L., Koresko, C. D., & Hill, R. J. 2004, Publ. Astron. Soc. Pac., 116, 876

[26] Cooperative Atmospheric Data Integration Project 2003, GLOBALVIEW-CO_2, Tech. rep., NOAA/CMDL. URL ftp://ftp.cmdl.noaa.gov/ccg/co2/GLOBALVIEW

[27] Delplancke, F. 2003, Performance and technical requirement specifications for PRIMA Star Separator (Auxiliary Telescopes). VLT-SPE-ESO-15710-2590

[28] — 2003, PRIMA, the Phase Referenced Imaging and Microarcsecond Astrometry facility: High Level Requirements & System Description. VLT-SPE-ESO-15700-3051

[29] — 2005, Prima Differential Delay Line (DDL), Performance & Technical Requirement Specifications. VLT-SPE-ESO-15720-2209

[30] Delplancke, F., Derie, F., Paresce, F., Glindemann, A., Lévy, F., Lévêque, S., & Ménardi, S. 2003, Astrophys. Space Sci., 286, 99

[31] Delplancke, F., Lévêque, S., Kervella, P., Glindemann, A., & d'Arcio, L. 2000, in Interferometry in Optical Astronomy, edited by P. J. Lena, & A. Quirrenbach (Int. Soc. Optical Engineering), vol. 4006 of Proc. SPIE, 365

[32] Delplancke, F., Nijenhuis, J., de Man, H., Andolfato, L., Treichel, R., & anf F. Derie, J. H. 2004, in New Frontiers in Stellar Interferometry, edited by W. A. Traub (Int. Soc. Optical Engineering), vol. 5491 of Proc. SPIE, 1528

[33] Derr, V. E. 1984, Atmospheric Handbook: Atmospheric Data Tables Available on Computer Tape (Boulder, CO: World Data Center A for Solar-Terrestrial Physics)

[34] Di Folco, E., Koehler, B., Kervella, P., Sarazin, M., Coudé du Foresto, V., Schöller, M., & Wittkowski, M. 2003, in Interferometry for Optical Astronomy II, edited by W. A. Traub (Int. Soc. Optical Engineering), vol. 4838 of Proc. SPIE, 1115

[35] Edlén, B. 1953, J. Opt. Soc. Am., 43, 339

[36] Eggarter, E. 1975, J. Chem. Phys., 62, 833

[37] Énard, D., Maréchal, A., & Espiard, J. 1996, Rep. Prog. Phys., 59, 601

[38] Fernández, D. P., Mulev, Y., Goodwin, A. R. H., & Levelt Sengers, J. M. H. 1995, J. Phys. Chem. Ref. Data, 24, 33

[39] Ferrari, M., Lemaître, G., Mazzanti, S., Lanzoni, P., Derie, F., Gitton, P., & Ménardi, S. 2000, in Interferometry in Optical Astronomy, edited by P. J. Lena, & A. Quirrenbach (Int. Soc. Optical Engineering), vol. 4006 of Proc. SPIE, 104

[40] Fiebig, N. 2007, Wind Monitoring System, Software Design. VLT-SPE-ESO-15760-4386

[41] — 2007, Wind Monitoring System, Software User Manual & Installation Guide. VLT-MAN-ESO-15760-4388

[42] Filippenko, A. V. 1982, Publ. Astron. Soc. Pac., 94, 715

[43] Flebus, C., Gloesener, P., Pirnay, O., Ninane, N., & Koehler, B. 2003, in Interferometry for Optical Astronomy II, edited by W. A. Traub (Int. Soc. Optical Engineering), vol. 4838 of Proc. SPIE, 759

[44] Fleury, M. 2005, DDL Vacuum System, Design, Analysis and Performance Report. VLT-TRE-DDL-15721-0001

[45] Folsch, N., Péronnet, F., Péan, M., Massicotte, D., & Lavoie, C. 2005, Metabolism, 54, 1428

[46] Gai, M., Menardi, S., Cesare, S., Bauvir, B., Bonino, D., Corcione, L., Dimmler, M., Massone, G., Reynaud, F., & Wallander, A. 2004, in New Frontiers in Stellar Interferometry, edited by W. A. Traub (Int. Soc. Optical Engineering), vol. 5491 of Proc. SPIE, 528

[47] Galliano, E., Schöller, M., Fischer, M., Hummel, C., Morel, S., Rantakyrö, F., & Vannier, M. 2004, in New Frontiers in Stellar Interferometry, edited by W. A. Traub (Int. Soc. Optical Engineering), vol. 5491 of Proc. SPIE, 1540

[48] Gitton, P. 2000, Results of May '00 tilt measurement campaign for the VLTI. VLT-TRE-ESO-15000-2261

[49] — 2003, VLTI Commissioning Part II: Effect of internal optical path on UT image stability, Test Report. VLT-TRE-ESO-15000-3083

[50] Gitton, P., Cantzler, M., Koehler, B., & Kervella, P. 2003, in Interferometry for Optical Astronomy II, edited by W. A. Traub (Int. Soc. Optical Engineering), vol. 4838 of Proc. SPIE, 1182

[51] Gitton, P., Koehler, B., Lévêque, S., & Glindemann, A. 2000, in Astronomical Telescopes and Instrumentation: Ground-Based Telescopes, edited by W. A. Traub (Int. Soc. Optical Engineering), vol. 4004 of Proc. SPIE, 222

[52] Gitton, P., Lévêque, S., Avila, G., & Duc, T. P. 2004, in New Frontiers in Stellar Interferometry, edited by W. A. Traub (Int. Soc. Optical Engineering), vol. 5491 of Proc. SPIE, 944

[53] Gitton, P., Wilhelm, R., Glindemann, A., & Paresce, F. 2003, Determination of the field and pupil rotation in the VLTI laboratory. VLT-TRE-ESO-15000-3092

[54] Glindemann, A. 2000, PRIMA, the Phase Referenced Imaging and Microarcsecond Astrometry facility: System Description. VLT-SPE-ESO-15700-2207

[55] Glindemann, A., Algomedo, J., Amestica, R., Ballester, P., Bauvir, B., Bugueño, E., Correia, S., Delgado, F., Delplancke, F., Derie, F., Duhoux, P., di Folco, E., Gennai, A., Gilli, B., Giordano, P., Gitton, P., Guisard, S., Housen, N., Huxley, A., Kervella, P., Kiekebusch, M., Koehler, B., Lévêque, S., Longinotti, A., Ménardi, S., Morel, S., Paresce, F., Phan Duc, T., Richichi, A., Schöller, M., Tarenghi, M., Wallander, A., Wittkowski, M., & Wilhelm, R. 2003, Astrophysics and Space Science, 286, 35

[56] Goullioud, R., & Azizi, A. 2000, in Interferometry in Optical Astronomy, edited by P. J. Lena, & A. Quirrenbach (Int. Soc. Optical Engineering), vol. 4006 of Proc. SPIE, 788

[57] Green, R. M. 1985, Spherical Astronomy (Cambridge, London: Cambridge University Press)

[58] Gubler, J., & Tytler, D. 1998, Publ. Astron. Soc. Pac., 110, 738

[59] Hill, R. J., Clifford, S. F., & Lawrence, R. S. 1980, J. Opt. Soc. Am., 70, 1192

[60] Hill, R. J., & Lawrence, R. S. 1986, Infrared Phys., 26, 371

[61] Hlubina, P. 2003, Optik, 114, 185

[62] Hobiger, T., Boehm, J., Todorova, S., & Schuh, H. 2003, in 16th Working Meeting on European VLBI for Geodesy and Astrometry, edited by W. Schwegmann, & V. Thorandt (Bundesamt für Kartographie und Goedäsie), vol. 16, 291

[63] Hou, W., & Thalmann, R. 1994, Measurement, 13, 307

[64] Ince, E. C. 1956, Ordinary Differential Equations (Dover: Dover Publications)

[65] Jaffe, W. J. 2005, Astrometric Survey for Extra-Solar Planets with PRIMA, Astrometric Raw Data Specifications. VLT-SPE-AOS-15750-0003

[66] Jones, F. E. 1980, Appl. Opt., 19, 4129

[67] Kane, R. P., & de Paula, E. R. 1996, J. Atmosp. Terr. Phys., 58, 1673

[68] Koehler, B., & Flebus, C. 2000, in Interferometry in Optical Astronomy, edited by P. J. Lena, & A. Quirrenbach (Int. Soc. Optical Engineering), vol. 4006 of Proc. SPIE, 13

[69] Koehler, B., Kraus, M., Moresmau, J. M., Wirenstrand, K., Duchateau, M., Duhoux, P., Karban, R., Flebus, C., Gabriel, E., & Pirnay, O. 2004, in New Frontiers in Stellar Interferometry, edited by W. A. Traub (Int. Soc. Optical Engineering), vol. 5491 of Proc. SPIE, 600

[70] Koehler, B., Lévêque, S., & Gitton, P. 2003, in Interferometry for Optical Astronomy II, edited by W. A. Traub (Int. Soc. Optical Engineering), vol. 4838 of Proc. SPIE, 846

[71] Labit, P. 1998, Meteorological Prediction Software, User and Maintenance Manual. VLT-TRE-ESO-17443-1678

[72] Launhardt, R. 2005, Dispersion in DDL vacuum windows. MPIA-TRE-DDL-15722-0003

[73] Launhardt, R., Henning, T., Queloz, D., Quirrenbach, A., Bakker, E., Baumeister, H., Bizenberger, P., Bleuler, H., Delplancke, F., Derie, F., Fleury, M., Glindemann, A., Gillet, D., Hanenburg, H., Jaffe, W. J., de Jong, J. A., Maire, C., Mathar, R. J., Mullhaupt, P., Murakawa, K., Pepe, F., le Poole, R., Pragt, J., Reffert, S., Sache, L., Scherler, O., Ségransan, D., Setiawan, J., Sosnowska, D., Tubbs, R. N., Venema, L. B., Wagner, K., Weber, L., & Wüthrich, R. 2005, in Astrometry in the age of the next generation of large telescopes, edited by P. K. Seidelmann, & A. K. B. Monet (Astron. Soc. Pacific), vol. CS-338 of ASP Conf. Ser., 167

[74] Launhardt, R., Segransan, D., & Delplancke, F. 2004, PRIMA-DDL Optics, Technical Note about the issue of exchangeable vacuum windows. MPIA-TRE-DDL-15722-0001

[75] Lawson, P. R. 1996, Appl. Opt., 35, 5122

[76] Lévêque, S. 2000, in Interferometry in Optical Astronomy, edited by P. J. Lena, & A. Quirrenbach (Int. Soc. Optical Engineering), vol. 4006 of Proc. SPIE, 388

[77] — 2000, Results of environmental tests for the VLTI at Paranal, May 11–21/00. VLT-TRE-ESO-15000-2259

[78] — 2000, Technical Specification for the PRIMA Metrology System. VLT-SPE-ESO-15730-2211

[79] — 2002, Commissioning of the VLTI: Characterization of the internal environmental parameters. VLT-TRE-ESO-15000-2696

[80] — 2002, Temperature sensor network for the VLTI. VLT-TRE-ESO-15000-2532

[81] Leveque, S. 2004, Results of the Delay Line Metrology Test Campaign of November '03. VLT-TRE-ESO-15210-3267

[82] Lévêque, S., Salvadé, Y., Dandliker, R., & Scherler, O. 2002, Laser Focus World

[83] Lévêque, S., Salvadé, Y., Wilhelm, R., & Rabeling, D. 2002, PRIMA Metrology Test Campaign 27/4/02 to 5/5/02. VLT-TRE-ESO-15730-2827

[84] Lévêque, S., Wilhelm, R., Salvadé, Y., Scherler, O., & Dändliker, R. 2003, in Interferometry for Optical Astronomy II, edited by W. A. Traub (Int. Soc. Optical Engineering), vol. 4838 of Proc. SPIE, 983

[85] Ligtenberg, R. C. G., van der Burgt, P. J. M., Renwick, S. P., Westerveld, W. B., & Risley, J. S. 1994, Phys. Rev. A, 49, 2363

[86] Livengood, T. A., Fast, K. E., Kostiuk, T., Espenak, F., Buhl, D., Goldstein, J. J., Hewagama, T., & Ro, K. H. 1999, Publ. Astron. Soc. Pac., 111, 512

[87] Loiseau, S., & Malbet, F. 1996, Astron. Astrophys. Suppl., 116, 373

[88] Longueteau, E., Delage, L., & Reynaud, F. 2002, Appl. Opt., 41, 5835

[89] — 2003, in Interferometry for Optical Astronomy II, edited by W. A. Traub (Int. Soc. Optical Engineering), vol. 4838 of Proc. SPIE, 546

[90] Maire, C. 2006, Astrometric Survey for Extra-Solar Planets with PRIMA, DDL Instrument Control Hardware Design, Analysis and Performance Report. VLT-TRE-DDL-15727-0001

[91] Maisinger, K., Hobson, M. P., Saunders, R. D. E., & Grainge, K. J. B. 2004, Month. Not. Roy. Astron. Soc., 345, 800

[92] Malitson, I. H. 1965, J. Opt. Soc. Am., 55, 1205

[93] Malyuot, V., & Meinel, M. 2000, Astron. Astrophys. Suppl., 142, 457

[94] Manduca, A., & Bell, R. A. 1979, Publ. Astron. Soc. Pac., 91, 848

[95] Marchetti, S., & Simili, R. 2006, Infr. Phys. Techn., 47, 263. Presumbably, the factor 10^{-4} ought read 10^{+4} and the temperature 296 °C read 23 °C in Table 1.

[96] Margoliash, D. J., & Meath, W. J. 1978, J. Chem. Phys., 68, 1426

[97] Mariotti, J.-M., Denise, C., Dérie, F., Ferrari, M., Glindemann, A., Koehler, B., Levêque, S., Paresce, F., Schöller, M., Tarenghi, M., & Verola, M. 1998, in Astronomical Interferometry, edited by R. D. Reasenberg (Kona: Int. Soc. Optical Engineering), vol. 3350 of Proc. SPIE, 800

[98] Masson, C. R. 1994, in Astronomy with Millimeter and Submillimeter Wave Interferometry, edited by M. Ishiguro, & W. J. Welch (Astron. Soc. Pacific), vol. 59 of ASP Conf. Ser., 87

[99] Mathar, R. J. 2004, arXiv:astro-ph/0411384

[100] — 2004, Appl. Opt., 43, 928

[101] — 2005, Astrometric Survey for Extra-Solar Planets with PRIMA, Requirements on Medium-Term Stability of Air Parameters in VLTI Ducts and Delay Lines. VLT-SPE-AOS-15753-0003

[102] — 2005, Baltic Astronomy, 14, 277

[103] — 2006, arXiv:physics/0610256

[104] — 2007, Correlation of MIDI Phase Fluctuations with Fluctuations of Water and Carbon Dioxide, Paranal June 2007. UL-TRE-MID-15829-0113

[105] Mathar, R. J., Jaffe, W. J., & Poole, R. S. L. 2007, High Frequency Fluctuations of Water and Carbon Dioxide, Paranal July 25–27, 2007. UL-TRE-ESO-15000-0836

[106] Matsumoto, H. 1982, Metrologia, 18, 49. We assume that the f-value in Table 2 is 1333, not 133 Pa, and that the three values refer to three different wavelengths—those in Table 1—not two.

[107] — 1984, Opt. Commun., 50, 356

[108] McCartney, E. J. 1976, Optics of the atmosphere: scattering by molecules and particles (London, Sydney, Toronto: Wiley)

[109] Meisner, J. A., & Le Poole, R. S. 2003, in Interferometry for Optical Astronomy II, edited by W. A. Traub (Int. Soc. Optical Engineering), vol. 4838 of Proc. SPIE, 609

[110] Meisner, J. A., Tubbs, R. N., & Jaffe, W. J. 2004, in New Frontiers in Stellar Interferometry, edited by W. A. Traub (Int. Soc. Optical Engineering), vol. 5491 of Proc. SPIE, 725

[111] Menardi, S. 2000, Interferometric Laboratory, Optical Layout. VLT-DWG-ESO-15000-1738

[112] Michellod, Müllhaupt, P., & Gillet 2006, Astrometric Survey for Extra-Solar Planets with PRIMA, DDL Translation Control, Design, Analysis and Performance Report. VLT-TRE-DDL-15725-0001

[113] Milman, M. H., & Turyshev, S. G. 2000, in Interferometry in Optical Astronomy, edited by P. J. Lena, & A. Quirrenbach (Int. Soc. Optical Engineering), vol. 4006 of Proc. SPIE, 828

[114] Moran, J. M., & Dhawan, V. 1995, in Very Long Baseline Interfermoetry and the VLBA, edited by J. A. Zensus, P. J. Diamond, & P. J. Napier, vol. 82 of ASP Conference Series, 161

[115] Nijenhuis, J. R. 2003, PRIMA Star Separater (STS), Design and Analysis Report. VLT-TRE-TNO-15710-0001

[116] Nir, S., Adams, S., & Rein, R. 1973, J. Chem. Phys., 59, 3341

[117] Old, J. G., Gentili, K. L., & Peck, E. R. 1971, J. Opt. Soc. Am., 61, 89

[118] Ott, J. 2006, VLT, FINITO WS Software, Design Description. VLT-SPE-4DE-15430-2695

[119] Owens, J. C. 1967, Appl. Opt., 6, 51

[120] Padial, N., Csanak, G., McKoy, B. V., & Langhoff, P. W. 1981, J. Chem. Phys., 74, 4581

[121] — 1981, Phys. Rev. A, 23, 218

[122] Pardo, J. R., Wiedner, M. C., Serabyn, E., Wilson, C. D., Cunningham, C., Hills, R. E., & Cernicharo, J. 2004, Astron. Astrophys. Suppl. Ser., 153, 363

[123] Peck, E. R. 1986, Appl. Opt., 25, 3597

[124] Peck, E. R., & Khanna, B. N. 1962, J. Opt. Soc. Am., 52, 416

[125] Peck, E. R., & Reeder, K. 1972, J. Opt. Soc. Am., 62, 958

[126] Phan Duc, T., & Gitton, P. 2005, VLTI Software, Infra-red Image Sensor, Control Software Design Description. VLT-SPE-ESO-15450-3196

[127] Puech, F., & Gitton, P. 2005, Interface Control Document between VLTI and its Instruments. VLT-ICD-ESO-15000-1826. On page 110, f_c^{-2} should read $f_c^{-8/3}$, $f < f$ should read $f < f_c$, and $1.38\,10^{-3}$ should read 1.38×10^{-3}.

[128] Quirrenbach, A. 2003, Astroph. Space Science, 286, 277

[129] Quirrenbach, A., du Foresto, V. C., Daigne, G., Hofmann, K.-H., Hofmann, R., Lattanzi, M., Osterbart, R., le Poole, R., Queloz, D., & Vakili, F. 1998, in Astronomical Interferometry, edited by R. D. Reasenberg (Int. Soc. Optical Engineering), vol. 3350 of Proc. SPIE, 807

[130] Quirrenbach, A., Henning, T., Queloz, D., Albrecht, S., Bakker, E., Baumeister, H., Bizenberger, P., Bleuler, H., Dändliker, R., de Jong, J., Fleury, M., Frink, S., Gillet, D., Jaffe, W. J., Hanenburg, S. H., Hekker, S., Launhardt, R., le Poole, R., Maire, C., Mullhaupt, P., Murakawa, K., Pepe, F., Pragt, J., Sache, L., Scherler, O., Ségransan, D., Setiawan, J., Sosnowska, D., Tubbs, R., Venema, L., Wagner, K., Weber, L., & Wüthrich, R. 2004, in New Frontiers in Stellar Interferometry, edited by W. A. Traub (Int. Soc. Optical Engineering), vol. 5491 of Proc. SPIE, 424

[131] Rank, D. H., Saksena, G. D., & McCubbin, T. K., Jr. 1958, J. Opt. Soc. Am., 48, 455

[132] Ridgway, S. T., Bagnuolo, W. G., Blakley, R., ten Brummelaar, T., Ferrell, D. R., McAliaster, H. A., Shure, M. A., Simison, E. J., Sturmann, L., & Turner, N. H. 2000, in Interferometry in Optical Astronomy, edited by P. J. Lena, & A. Quirrenbach (Int. Soc. Optical Engineering), vol. 4006 of Proc. SPIE, 696

[133] Roddier, F. 1981 (Amsterdam: North Holland), vol. XIX of Prog. Opt., 281–376

[134] Rothman, L. S., Barbe, A., Benner, D. C., Brown, L. R., Camy-Peyret, C., Carleer, M. R., Chance, K., Clerbaux, C., Dana, V., Devi, V. M., Fayt, A., Flaud, J.-M., Gamache, R. R., Goldman, A., Jacquemart, D., Jucks, K. W., Lafferty, W. J., Mandin, J.-Y., Massie, S. T., Nemtchinov, V., Newnham, D. A., Perrin, A., Rinsland, C. P., Schroeder, J., Smith, K. M., Smith, M. A. H., Tang, K., Toth, R. A., Vander Auwera, J., Varanasi, P., & Yoshino, K. 2003, J. Quant. Spectrosc. Radiat. Transfer, 82, 5

[135] Rozanov, V. V., Buchwitz, M., Eichmann, K.-U., de Beck, R., & Burrows, J. P. 2002, Adv. Space Res., 29, 1831

[136] Rüeger, J. M. 1999, Report of the Ad-Hoc Working Party on "Refractive indices of light, infrared and radio waves in the atmosphere" of the IAG Special Commission SC3–Fundamental Constants (SCFC), Tech. rep., International Association of Geodesy. URL http://www.gfy.ku.dk/~iag/Travaux_99/wp51.htm

[137] Salem, M., Korotkova, O., Dogariu, A., & Wolf, E. 2004, Waves Random Media, 14, 513

[138] Salvadé, Y., & Courteville, A. 2000, PRIMA Metrology, Rider study, Final report. VLT-TRE-IMT-15700-0001

[139] Salvadé, Y., & Scherler, O. 2002, Feasibility study for the frequency stabilization of the PRIMA metrology laser. VLT-TRE-IMT-15731-2868

[140] Sampson, R. D., Lozowski, E. P., & Machel, H. G. 2005, Appl. Opt., 44, 5652

[141] Sarazin, M. 2002, in IAU Technical workshop "Astronomical Site evaluation in the visible and radio range", edited by J. Vernin, Z. Benkhaldoun, & C. M. noz Tuñón (Astron. Soc. Pacific), vol. 266 of ASP Conf. Ser., 532

[142] — 2003, Astroclimatology of Paranal, Tech. rep., European Southern Observatory. URL http://www.eso.org/gen-fac/pubs/astclim/paranal

[143] — 2005. Priv. commun., attributed to A. Erasmus

[144] Sault, R. J., Carrad, G. J., Hall, P. J., & Crofts, J. 2007, arXiv:astro-ph/0701016

[145] Schiebener, P., Straub, J., Levelt Sengers, J. M. H., & Gallagher, J. S. 1990, J. Phys. Chem. Ref. Data, 19, 1617

[146] — 1990, J. Phys. Chem. Ref. Data, 19, 677. E: [145]

[147] Schödel, R., Walkov, A., & Abou-Zeid, A. 2006, Opt. Lett., 31, 1979

[148] Schöller, M., Gitton, P., Argomedo, J., Ballester, P., Bauvier, B., van Boekel, R., Cantzler, M., Correia, S., Cotton, W., Delplancke, F., Derie, F., Duhoux, P., Eerm, T., di Folco, E., du Foresto, V. C., et al. 2003, in Interferometry for Optical Astronomy II, edited by W. A. Traub (Int. Soc. Optical Engineering), vol. 4838 of Proc. SPIE, 870

[149] Shaklan, S., Milman, M., Catanzarite, J., Basdogan, I., Papalexandris, M., Sievers, L., & Swartz, R. 2003, in Interferometry in Space, edited by M. Shao (Int. Soc. Optical Engineering), vol. 4852 of Proc. SPIE, 623

[150] Simmons, A. C. 1978, Opt. Commun., 25, 211

[151] Smith, K. M., Ptashnik, I., Newnham, D. A., & Shine, K. P. 2004, J. Quant. Spectrosc. Radiat. Transfer, 83, 735

[152] Sovers, O. J., Fanselow, J. L., & Jacobs, C. S. 1998, Rev. Mod. Phys., 70, 1391

[153] Spitzer, W. G., & Kleinman, D. A. 1961, Phys. Rev., 121, 1324

[154] Stanghellini, S., & Michel, A. 1998, The Messenger, 94, 10

[155] Stewart, H. S., & Hopfield, R. F. 1965, Atmospheric Effects (New York, London: Academic Press), vol. 1, 133

[156] Stirling, A., Otárola, A., Rivera, R., & Bravo, J. R. 2006, Horizontal temperature variations at Chajnantor, ALMA Memo 541

[157] Stone, R. C. 1996, Publ. Astron. Soc. Pac., 108, 1051

[158] Tan, C. Z., & Arndt, J. 2000, J. Phys. Chem. Solids, 61, 1315

[159] Tango, W. J. 1990, Appl. Opt., 29, 516

[160] Thomas, M. E., & Joseph, R. I. 1996, Johns Hopkins Apl. Technical Digest, 17, 279

[161] Trott 2004, ISO/IEC CD 18026, Information technology —computer graphics and image processing— spatial reference model. Annex D: RDs associated with celestial objects, Tech. rep., ISO/IEC JTC 1/SC 24, Working Group 8 on Environmental Representation. URL http://www.sedris.org/wg8home/document.htm

[162] Tubbs, R. N., & Mathar, R. J. 2006, Astrometric Survy for Extra-Solar Planets with PRIMA, Astrometric Error Budget. VLT-TRE-AOS-15753-0001 in the version of Dec. 2006

[163] Tubbs, R. N., Meisner, J. A., Bakker, E. J., & Albrecht, S. 2004, in Astronomical Telescopes and Instrumentation, edited by W. A. Traub (Int. Soc. Optical Engineering), vol. 5491 of Proc. SPIE, 588

[164] Tubbs, R. N., Quirrenbach, A., Le Poole, R., Bakker, E. J., & Jaffe, W. J. 2003, PRIMA Astrometric System Analysis, STC PRIMA DDL Proposal. VLT-TYP-DDL-ABCDE-NNNN

[165] Unwin, S. C., & Shao, M. 2000, in Interferometry in Optical Astronomy, edited by P. J. Lena, & A. Quirrenbach (Int. Soc. Optical Engineering), vol. 4006 of Proc. SPIE, 754

[166] van der Werf, S. Y. 2003, Appl. Opt., 42, 354

[167] Velsko, S. P., & Eimerl, D. 1986, Appl. Opt., 25, 1344

[168] Venema, L. B., et al. 2003, Astrometric Survey of Extra-Solar Planets with PRIMA, Technical Proposal. Planets-PRI-TEC-0002

[169] Visser, M. 1999, Very Large Telescope Interferometer, Delay Lines, Control Design and Simulation Report. VLT-TRE-FOK-15210-0013

[170] Wagner, T., Heland, J., Zöger, M., & Platt, U. 2003, Atmos. Chem. Phys., 3, 651

[171] Wagner, W., & Pruß, A. 2002, J. Phys. Chem. Ref. Data, 31, 387

[172] Wallace, P. T. 2005, IPHASE, Interferometer Optial-Path-Length Analysis System. Http://www.tpsoft.demon.co.uk

[173] Wallander, A. 2004, Final Lay-out of VLTI Control LANs. VLT-SPE-ESO-15410-1957

[174] — 2005, VLTI Supervisor Software (ISS) Design Description. VLT-SPE-ESO-15410-2114

[175] Wary, J. H., & Neu, J. T. 1969, J. Opt. Soc. Am., 59, 774

[176] Wiedner, M. C., Hills, R. E., Calstrom, J. E., & Lay, O. P. 2001, Astrophys. J., 553, 1036

[177] Wilhelm, R., Koehler, B., & Gitton, P. 2002, Functional Description of the VLTI. VLT-ICD-ESO-15000-1918. The radii of curvature of M2, M5 and M7 in Table 4-1 are wrong. See [154] for M2.

[178] Yan, M., Sadeghpour, H. R., & Dalgarno, A. 1998, Astrophys. J., 496, 1044. E: [179]

[179] — 2001, Astrophys. J., 559, 1194. http://dx.doi.org/10.1086/322775

[180] Yang, Z., Toon, G. C., Margolis, J. S., & Wennberg, P. O. 2002, Geophys. Res. Lett., 29, 53

[181] Zhang, J., Lu, Z. H., & Wang, L. J. 2005, Opt. Lett., 30, 3314

[182] Zhenhui, W., & Peichang, Z. 2004, J. Quant. Spectrosc. Radiat. Transfer, 83, 423

1.4 Acronyms

ARC Ecole d'ingenieurs de l'arc Jurassie http://www.eiaj.ch/

ASTRON Stichting Astronomisch Onderzoek in Nederland http://www.astron.nl

AT Auxiliary Telescope (of the VLTI)
http://www.eso.org/projects/vlti/AT/index_at.html

BC Beam Combiner

BC Beam Compressor

CMM Configuration Management Module
http://www.eso.org/projects/vlt/sw-dev/wwwdoc/dockit.html

DDL Differential Delay Line http://www.mpia-hd.mpg.de/PRIMA-DDL/

DL Delay Line

DOPD differential OPD

DRS Data Reduction System

EPFL École Polytechnique Fédérale de Lausanne http://www.epfl.ch

ESO European Southern Observatory http://www.eso.org

FINITO Fringe-Tracking Facility of Nice and Torino

FITS Flexible Image Transport System http://fits.gsfc.nasa.gov

FOV field of view

FSU Fringe Sensing Unit

FT Fourier Transform

GENIE Ground based European Nulling Interferometry Experiment
http://www.strw.leidenuniv.nl/~nevec/GENIE/

ICS Instrument Control Software

IR Infrared

IRIS Infrared Image Sensor http://www.eso.org/projects/vlti/iris/

ISS Interferometric Supervisor-Software

mas milli-arcsecond

MDL main delay line
http://www.eso.org/outreach/press-rel/pr-2000/phot-26-00.html

MIDI Mid-Infrared Interferometric Instrument http://www.mpia.de/MIDI

MPIA Max-Planck Institut für Astronomie, Heidelberg http://www.mpia.de

NOVA Nederlandse Onderzoekschool voor Astronomie
http://www.strw.leidenuniv.nl/nova/

OPD optical path difference

OPL optical path length

ppmv parts-per-million of volume

PRIMA Phase-Reference Imaging and Microarcsecond Astrometry
http://obswww.unige.ch/Instruments/PRIMA

PS primary star

PSD power spectral density

PSF point spread function

PWV precipitable water vapor

SS secondary star

STS star separator

TAD transverse atmospheric dispersion

TCCD technical CCD

TIR total internal reflection

UT Unit Telescope (of the VLTI) http://www.eso.org/projects/vlt/unit-tel/

UTC Universal Time Coordinated

VCM variable curvature mirror

VINCI VLT Interferometer Comissioning Instrument

VIS visible (part of the electromagnetic spectrum)

VLTI Very Large Telescope Interferometer http://www.eso.org/vlti

VLTSW VLT Software Problem Report http://www.eso.org/vlt/vlt-sw

ZOPD zero OPD

See http://www.strw.leidenuniv.nl/~mathar/abbrev.html for more.

2 CHARACTERISATION OF AIR DISPERSION

2.1 Available Literature

Knowledge of the refractive index of moist air includes,

1. experiments on moist air in the VIS [10, 14, 147]
2. experiments on water vapor at 3.4 and 10.6 μm [106, 107]
3. experiments on dry air and its molecular constituents in the VIS [11, 35, 63, 181], at 1.064 μm [123, 167] up to 2.0 μm [124], up to 1.7 μm [117, 125], at 10.6 μm [95, 150],
4. implicit verification of N band dispersion with MIDI [163]
5. review formulas [22, 66, 116, 119, 146],
6. theoretical summation of electronic transitions [25, 59, 60, 100, 103],
7. the microwave regions [182] and static limit [38].

Fig. 1 visualizes the prototypical humid air dispersion on the mountain, 3.94 hPa of water and a total pressure of 750.58 hPa at 12 °C. The calculation adopts a standard of 370 ppmv of CO_2 [26, 67, 180] and are based on HITRAN [134] (see [151] for critical reviews) and other sources of transition line strengths. The values differ from [100, Fig. 3] as the oxygen contents has been increased from 20.1% to 20.983% and agree with experiments to $4 \cdot 10^{-8}$ [103]. FINITO works in the H band (1.5–1.8 μm) [46, 55, 118]. The values of the refractivity shown in [138, Fig 1] are about 2 % smaller, because the temperature was chosen 1 % higher, the pressure 1 % lower and also the humidity lower than here.

The refractive index

$$n = \sqrt{1 + \chi} \tag{1}$$

is chromatic (the phase shift depends on the wavelength λ and wave number $\tilde{\nu} = 1/\lambda$) since

$$dn/d\lambda = -\tilde{\nu}^2 \frac{dn}{d\tilde{\nu}} \tag{2}$$

is not a constant but depends itself on λ (Fig. 3). The negative of this parameter, measured in radian and divided by the areal molar gas density, has been baptized "normalized dispersion constant" K in [109, 110].

2.2 Completion With Respect to Residual Gases

Fig. 1 shows a calculation which includes oscillator strengths of the major components of air, N_2, O_2, CO_2, H_2O, for O_3, CH_4 and CO the transitions as far as they are listed in HITRAN [134], and Ar and Ne as listed in [19, 20, 36]. An estimate of the combined contribution of residual gases that would also be on the list of molecules sorted with respect to abundance under the rather clean environmental Atacama conditions is in Fig. 4. The electromagnetic line lists are taken from [85, 178] for He, [96, 134] for CH_4, [20] for Kr, [96] for H_2, [96, 134] for N_2O, [134] for SO_2, [120, 134] for O_3 and [96, 134] for NH_3.

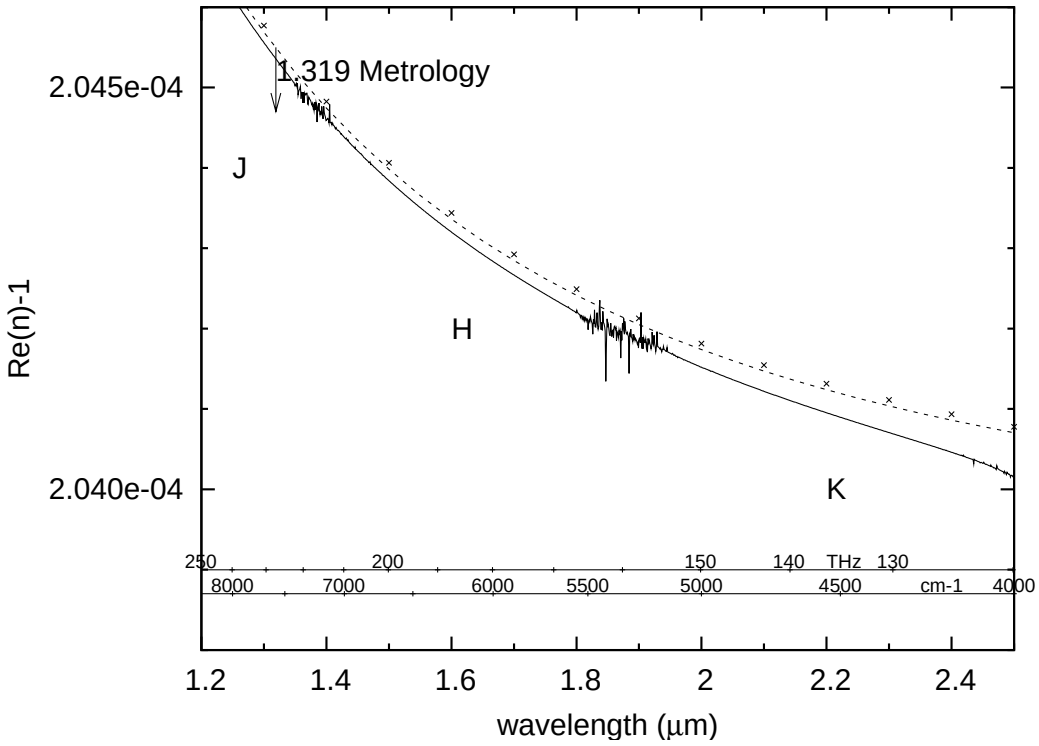

Figure 1: Air refractive index at standard Paranal composition (humidity, temperature and pressure) in the H, J and K band, based on the 2006 edition of the HITRAN database calculated according to [100]. The corrections described in [103] are incorporated. Crosses represent a fit due to Ciddor [22, App. B][136]. The dashed line is the Owens fit [119].

The change in refractivity across the near-IR bands of these dilute gases is about four orders of magnitude smaller than the change induced by the major air components shown in Fig. 1, and therefore negligible.

The role of aerosols in this scenario remains undefined, because nothing is known about their densities on Paranal. If one would scale the bulk refractive index of solid quartz [153, Fig. 4] to a density of 10^{18} molecules per m^3, it would add $n-1 \approx 1.7 \cdot 10^{-11}$ to the refractivity, with a drop of about $2.4 \cdot 10^{-13}$ between 2 μm and 2.5 μm. Assuming a quartz particle count of $10^6/m^3$ with particle diameters of 0.5 μm [142] yields only $1.7 \cdot 10^{15}$ molecules/m^3, and a particle count of $10^3/m^3$ with particle diameters of 5 μm [142] another $1.7 \cdot 10^{15}$ molecules/m^3, such that their effects on the refractivity should remain negligible.

A lesson from Fig. 5 is that the water lines near to the metrology laser wavelength are only of interest if one tries to obtain accuracies of the order of $2 \cdot 10^{-10}$.

2.3 Infrared Fits

A bold least squares fit to the data of Figs. 1 looks as follows [103]:

$$n-1 \quad = \quad \sum_{i=0,1,\ldots} c_i(T,p,H)\,(\tilde{\nu}-\tilde{\nu}_{\rm ref})^i\,; \tag{3}$$

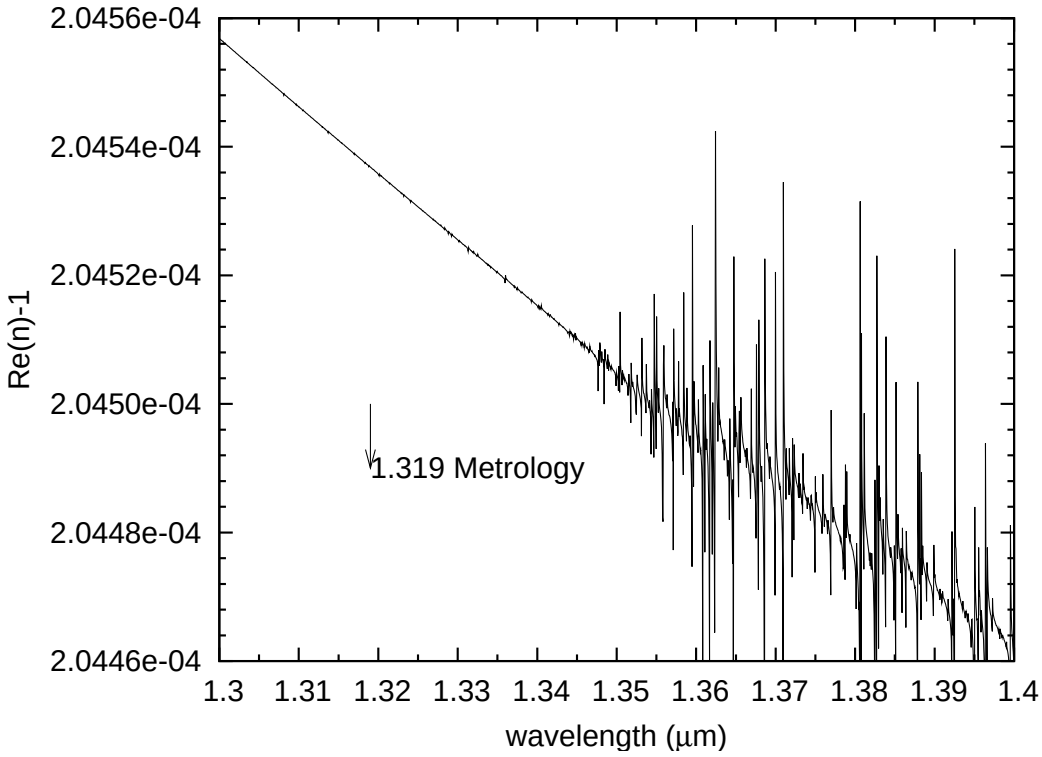

Figure 2: A magnified view into Fig. 1 and into the neighborhood of the PRIMA metrology wavelength.

$$
\begin{aligned}
c_i(T,p,H) \;=\; & c_{i\mathrm{ref}} + c_{iT}\left(\frac{1}{T}-\frac{1}{T_{\mathrm{ref}}}\right) + c_{iTT}\left(\frac{1}{T}-\frac{1}{T_{\mathrm{ref}}}\right)^2 + c_{iH}\,(H-H_{\mathrm{ref}}) + c_{iHH}\,(H-H_{\mathrm{ref}})^2 \\
& + c_{ip}\,(p-p_{\mathrm{ref}}) + c_{ipp}\,(p-p_{\mathrm{ref}})^2 + c_{iTH}\left(\frac{1}{T}-\frac{1}{T_{\mathrm{ref}}}\right)(H-H_{\mathrm{ref}}) \\
& + c_{iTp}\left(\frac{1}{T}-\frac{1}{T_{\mathrm{ref}}}\right)(p-p_{\mathrm{ref}}) + c_{iHp}\,(H-H_{\mathrm{ref}})\,(p-p_{\mathrm{ref}})\,. \qquad (4)
\end{aligned}
$$

Here, T is the absolute temperature with a reference value of T_{ref}, p is the air pressure with a reference value set at p_{ref}, H the relative humidity between 0 and 100 with a reference value set at H_{ref}, and $\tilde{\nu}$ the wavenumber $1/\lambda$ with a reference value set at $\tilde{\nu}_{\mathrm{ref}}$. The 1.3–2.5 μm range is covered by Table 1, the 2.8–4.2 μm range by Table 2, the 4.35–5.3 μm range by Table 3, the 7.5–14.1 μm range by Tables 4 and 5, and the 16–20 μm range by Table 6. The tables assume a CO_2 content of 370 ppmv with the exception of Table 5 which is calculated at 450 ppmv. The web site `http://www.strw.leidenuniv.nl/~mathar/progs/prWaterWeb.html` contains an on-line calculator of this fit. [103] shows tables based on the same methodology fitted to a wider range of parameters, hence less recommended to predict refractivities of the VLTI tunnel air.

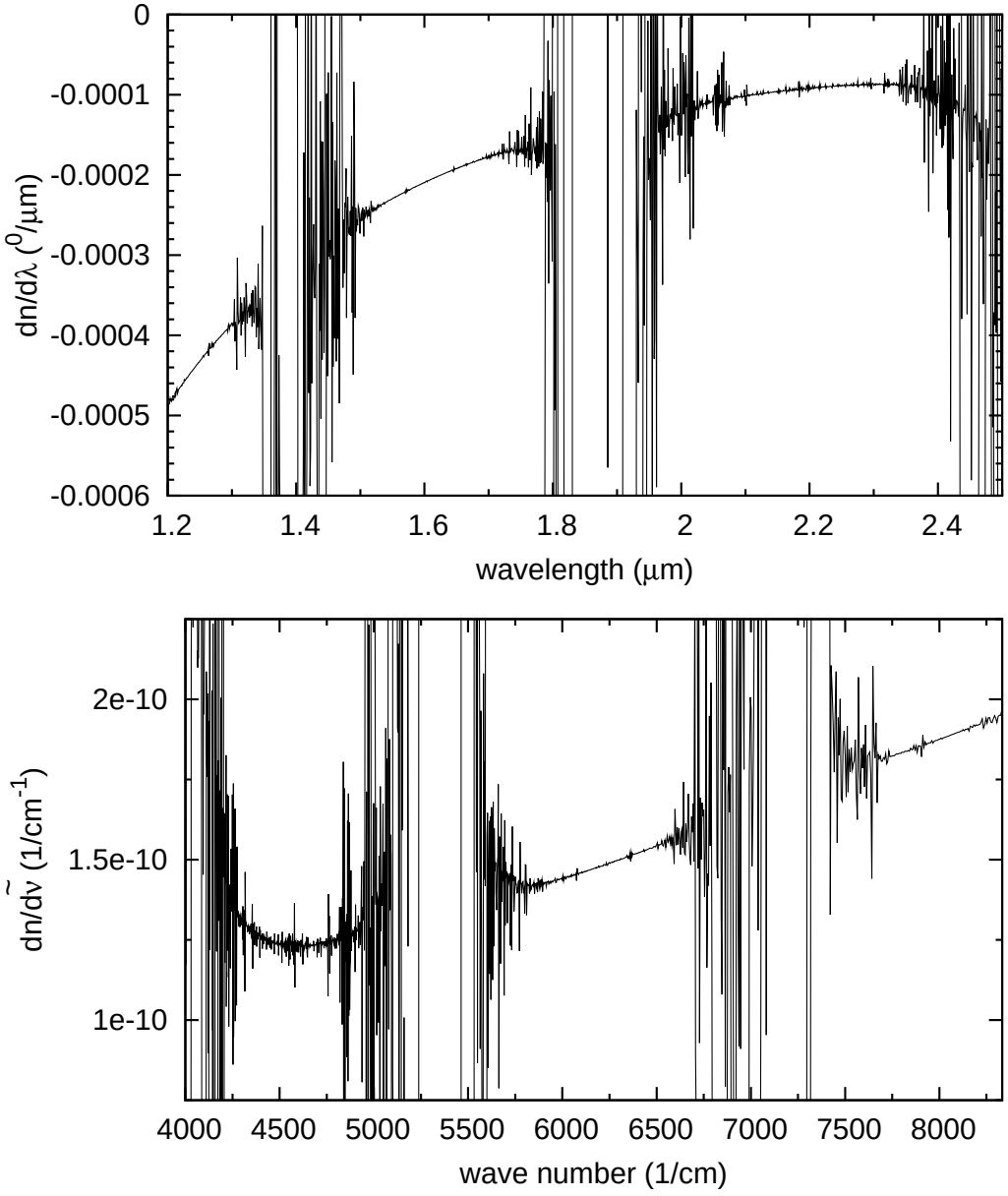

Figure 3: Top: The chromatic phase shift $dn/d\lambda$ in units of degrees per μm wavelength is the first derivative of Fig. 1 multiplied by 360°. Bottom: the equivalent derivative for the (spectroscopic) wave number, $dn/d\tilde{\nu}$, without the factor of 360. The relevant numbers are obtained by further multiplication with the baseline length.

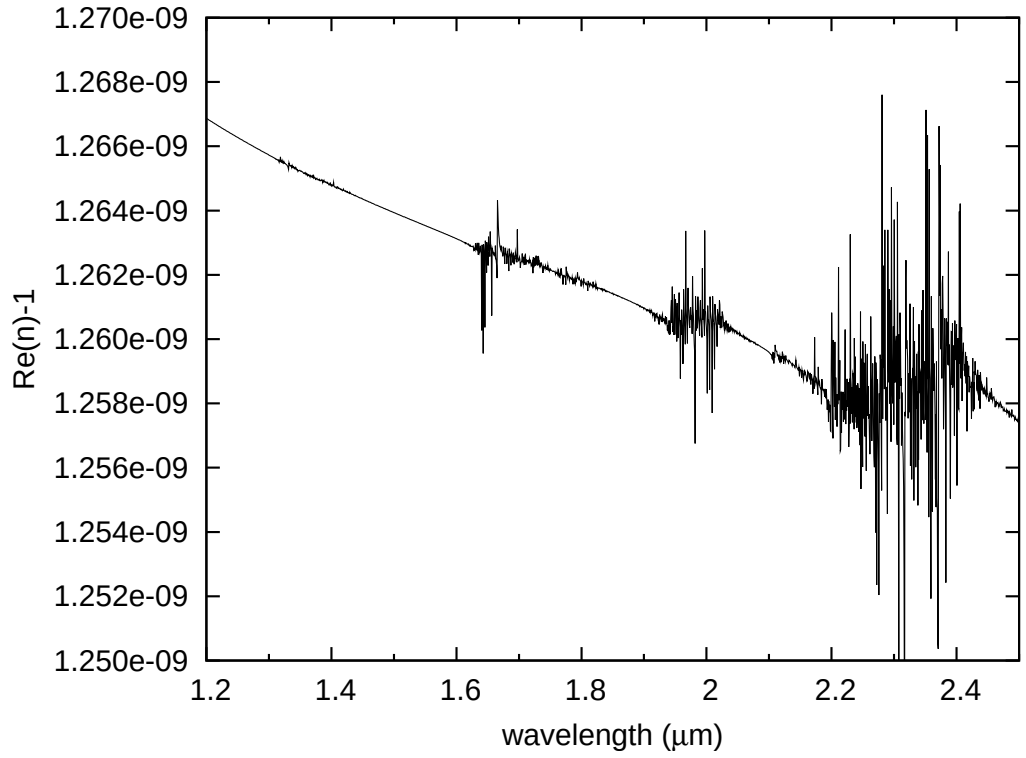

Figure 4: The combined refractivity of 0.39 Pa He, 0.12 Pa CH_4, 0.075 Pa Kr, 0.038 Pa H_2, 0.022 Pa N_2O, $3.8 \cdot 10^{-5}$ Pa SO_2, $8.8 \cdot 10^{-3}$ Pa O_3, 0.03 Pa NH_3 is $\approx 10^{-9}$ at 12 °C, but the dispersion (change in the refractivity) across the relevant bands in the near-IR only $\approx 10^{-11}$.

i	c_{iref} / cm^i	c_{iT} / cm^{i}K	c_{iTT} / [cm^{i}K^2]	c_{iH} / [cm^i/%]	c_{iHH} / [cm^i/%^{2}]
0	$0.199622 \cdot 10^{-3}$	$0.583386 \cdot 10^{-1}$	-2.01596	$-0.903724 \cdot 10^{-8}$	$0.397847 \cdot 10^{-12}$
1	$0.113213 \cdot 10^{-9}$	$-0.322796 \cdot 10^{-7}$	$0.272176 \cdot 10^{-3}$	$0.118891 \cdot 10^{-11}$	$0.135161 \cdot 10^{-16}$
2	$-0.432319 \cdot 10^{-14}$	$0.804729 \cdot 10^{-10}$	$-0.344397 \cdot 10^{-6}$	$-0.148391 \cdot 10^{-14}$	$-0.164684 \cdot 10^{-19}$
3	$0.101321 \cdot 10^{-16}$	$-0.512187 \cdot 10^{-13}$	$0.229488 \cdot 10^{-9}$	$0.978598 \cdot 10^{-18}$	$0.108771 \cdot 10^{-22}$
4	$-0.294544 \cdot 10^{-20}$	$0.150236 \cdot 10^{-16}$	$-0.676185 \cdot 10^{-13}$	$-0.285699 \cdot 10^{-21}$	$-0.317570 \cdot 10^{-26}$
5	$0.308689 \cdot 10^{-24}$	$-0.157540 \cdot 10^{-20}$	$0.712756 \cdot 10^{-17}$	$0.298251 \cdot 10^{-25}$	$0.331548 \cdot 10^{-30}$
i	c_{ip} / [cm^i/Pa]	c_{ipp} / [cm^i/Pa^2]	c_{iTH} / [cm^{i}K/%]	c_{iTp} / [cm^{i}K/Pa]	c_{iHp} / [cm^i/(% Pa)]
0	$0.268473 \cdot 10^{-8}$	$0.277778 \cdot 10^{-15}$	$0.435203 \cdot 10^{-4}$	$0.778497 \cdot 10^{-6}$	$0.115942 \cdot 10^{-14}$
1	$0.136651 \cdot 10^{-14}$	$-0.185198 \cdot 10^{-21}$	$-0.576493 \cdot 10^{-8}$	$0.395720 \cdot 10^{-12}$	$-0.386473 \cdot 10^{-21}$
2	$0.135999 \cdot 10^{-18}$	$0.696092 \cdot 10^{-26}$	$0.723925 \cdot 10^{-11}$	$0.394125 \cdot 10^{-16}$	$-0.108889 \cdot 10^{-23}$
3	$0.822207 \cdot 10^{-23}$	$-0.417765 \cdot 10^{-29}$	$-0.479632 \cdot 10^{-14}$	$0.242058 \cdot 10^{-20}$	$0.739131 \cdot 10^{-27}$
4	$-0.224102 \cdot 10^{-26}$	$0.323484 \cdot 10^{-35}$	$0.140605 \cdot 10^{-17}$	$-0.682449 \cdot 10^{-24}$	$-0.148792 \cdot 10^{-30}$
5	$0.251184 \cdot 10^{-30}$	$0.922516 \cdot 10^{-37}$	$-0.147421 \cdot 10^{-21}$	$0.771620 \cdot 10^{-28}$	$0.264734 \cdot 10^{-34}$

Table 1: Fitting coefficients for the multivariate Taylor expansion (4) to the real part of the index of refraction over the $1.3 \leq 1/\tilde{\nu} \leq 2.5$ μm range. $T_{\mathrm{ref}} = (273.15 + 16)$ K, $p_{\mathrm{ref}} = 74400$ Pa, $H_{\mathrm{ref}} = 10$ %, and $\tilde{\nu}_{\mathrm{ref}} = 10^4/2.25$ cm^{-1}.

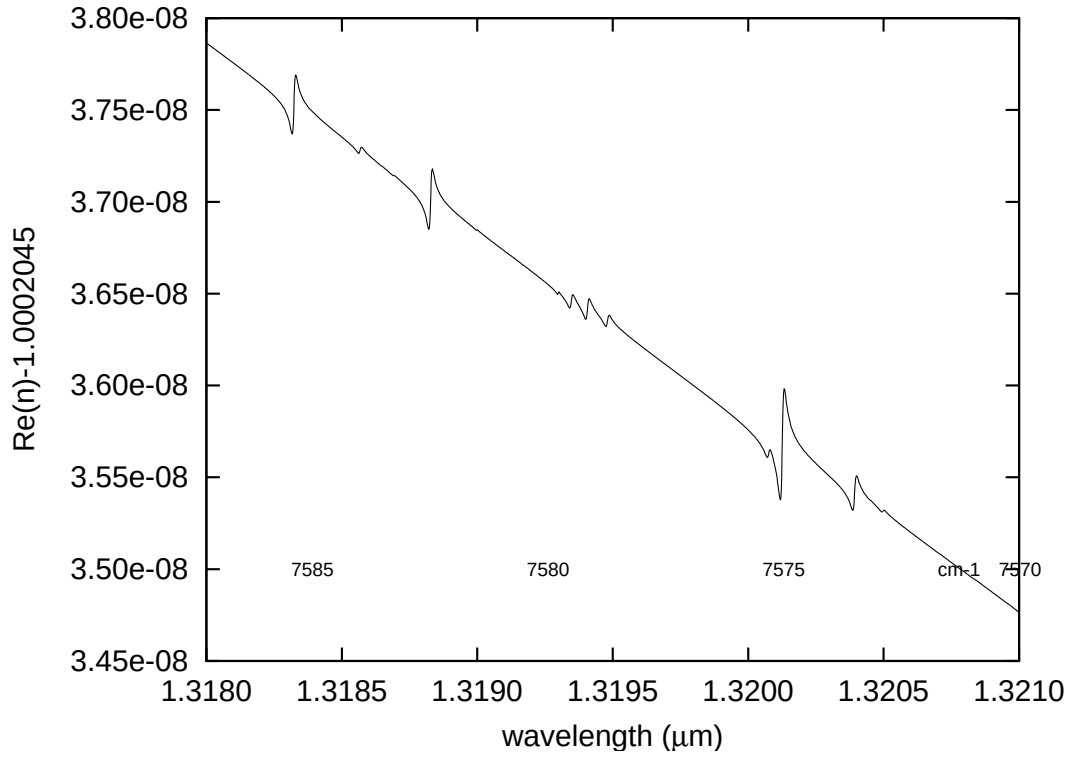

Figure 5: An even deeper view into the vicinity of the metrology wavelength, zooming further into Fig. 2.

i	$c_{i\mathrm{ref}}$ / cm^i	c_{iT} / cm^{i}K	c_{iTT} / [cm^{i}K^2]	c_{iH} / [cm^i/%]	c_{iHH} / [cm^i/%^{2}]
0	$0.199479 \cdot 10^{-3}$	$0.583174 \cdot 10^{-1}$	-2.09719	$-0.940190 \cdot 10^{-8}$	$0.399042 \cdot 10^{-12}$
1	$0.144868 \cdot 10^{-9}$	$-0.716175 \cdot 10^{-7}$	$0.464399 \cdot 10^{-3}$	$0.199559 \cdot 10^{-11}$	$0.224994 \cdot 10^{-16}$
2	$0.249753 \cdot 10^{-12}$	$0.129198 \cdot 10^{-9}$	$-0.334406 \cdot 10^{-6}$	$-0.133256 \cdot 10^{-14}$	$-0.141565 \cdot 10^{-19}$
3	$-0.743028 \cdot 10^{-15}$	$0.175930 \cdot 10^{-13}$	$-0.767442 \cdot 10^{-9}$	$-0.274414 \cdot 10^{-17}$	$-0.322987 \cdot 10^{-22}$
4	$-0.160749 \cdot 10^{-17}$	$-0.692212 \cdot 10^{-15}$	$0.139833 \cdot 10^{-11}$	$0.541857 \cdot 10^{-20}$	$0.563560 \cdot 10^{-25}$
5	$0.351580 \cdot 10^{-20}$	$-0.790598 \cdot 10^{-19}$	$0.390862 \cdot 10^{-14}$	$0.148830 \cdot 10^{-22}$	$0.174229 \cdot 10^{-27}$
i	c_{ip} / [cm^i/Pa]	c_{ipp} / [cm^i/Pa^2]	c_{iTH} / [cm^{i}K/%]	c_{iTp} / [cm^{i}K/Pa]	c_{iHp} / [cm^i/(% Pa)]
0	$0.268289 \cdot 10^{-8}$	$0.462964 \cdot 10^{-16}$	$0.452883 \cdot 10^{-4}$	$0.778081 \cdot 10^{-6}$	$-0.260870 \cdot 10^{-14}$
1	$0.168954 \cdot 10^{-14}$	$0.138867 \cdot 10^{-21}$	$-0.975525 \cdot 10^{-8}$	$0.445736 \cdot 10^{-12}$	$0.222222 \cdot 10^{-20}$
2	$0.354461 \cdot 10^{-17}$	$0.416683 \cdot 10^{-24}$	$0.671485 \cdot 10^{-11}$	$0.781399 \cdot 10^{-15}$	$-0.454106 \cdot 10^{-23}$
3	$-0.966907 \cdot 10^{-20}$	$-0.324037 \cdot 10^{-27}$	$0.147527 \cdot 10^{-13}$	$-0.194402 \cdot 10^{-17}$	$0.743961 \cdot 10^{-26}$
4	$-0.224031 \cdot 10^{-22}$	$-0.925993 \cdot 10^{-30}$	$-0.276539 \cdot 10^{-16}$	$-0.541417 \cdot 10^{-20}$	$0.173913 \cdot 10^{-28}$
5	$0.454992 \cdot 10^{-25}$	$0.231463 \cdot 10^{-32}$	$-0.773420 \cdot 10^{-19}$	$0.103230 \cdot 10^{-22}$	$-0.241546 \cdot 10^{-31}$

Table 2: Fitting coefficients for the multivariate Taylor expansion (4) to the real part of the index of refraction over the $2.8 \le 1/\tilde\nu \le 4.2$ μm range. $T_{\mathrm{ref}} = (273.15 + 16)$ K, $p_{\mathrm{ref}} = 74400$ Pa, $H_{\mathrm{ref}} = 10$ %, and $\tilde\nu_{\mathrm{ref}} = 10^4/3.4$ cm^{-1}.

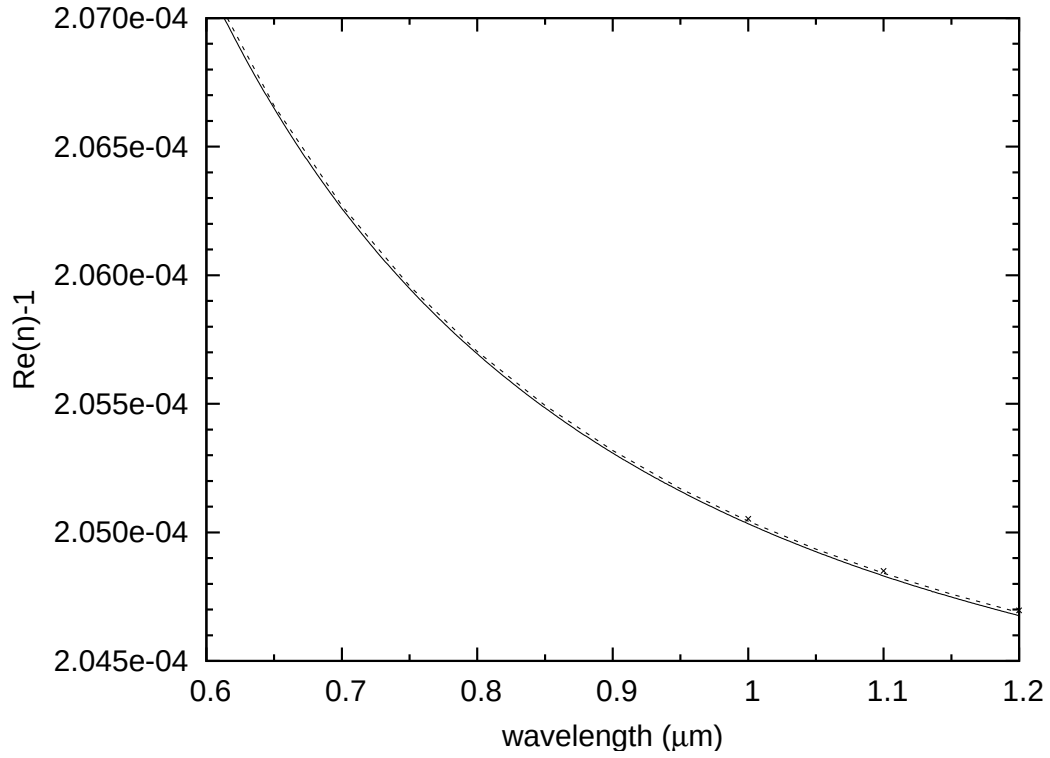

Figure 6: Figure 1 continued into the VIS. The gap between the theory (solid line) and the Owens formula (dashed line) is $1.5{\cdot}10^{-8}$ in this wavelength range. The optical path length difference between the vacuum and non-vacuum operation of the DDL over up to 0.12 m is up to 24 μm.

i	c_{iref} / cm^i	c_{iT} / cm^{i}K	c_{iTT} / [cm^{i}K^2]	c_{iH} / [cm^i/%]	c_{iHH} / [cm^i/%^{2}]
0	$0.199451 \cdot 10^{-3}$	$0.584622 \cdot 10^{-1}$	-2.73956	$-0.122106 \cdot 10^{-7}$	$0.393068 \cdot 10^{-12}$
1	$0.274669 \cdot 10^{-9}$	$-0.335923 \cdot 10^{-6}$	$0.167548 \cdot 10^{-2}$	$0.728848 \cdot 10^{-11}$	$0.814814 \cdot 10^{-16}$
2	$0.326247 \cdot 10^{-12}$	$0.139856 \cdot 10^{-9}$	$0.136584 \cdot 10^{-6}$	$-0.189949 \cdot 10^{-14}$	$-0.201792 \cdot 10^{-19}$
3	$-0.687937 \cdot 10^{-14}$	$0.113400 \cdot 10^{-11}$	$-0.422392 \cdot 10^{-8}$	$-0.967569 \cdot 10^{-17}$	$-0.125366 \cdot 10^{-21}$
4	$0.272177 \cdot 10^{-17}$	$0.457417 \cdot 10^{-13}$	$-0.205625 \cdot 10^{-9}$	$-0.768123 \cdot 10^{-18}$	$-0.850886 \cdot 10^{-23}$
5	$0.336833 \cdot 10^{-18}$	$-0.168448 \cdot 10^{-15}$	$0.846853 \cdot 10^{-12}$	$0.311207 \cdot 10^{-20}$	$0.353441 \cdot 10^{-25}$
i	c_{ip} / [cm^i/Pa]	c_{ipp} / [cm^i/Pa^2]	c_{iTH} / [cm^{i}K/%]	c_{iTp} / [cm^{i}K/Pa]	c_{iHp} / [cm^i/(% Pa)]
0	$0.268287 \cdot 10^{-8}$	$0.231482 \cdot 10^{-15}$	$0.589036 \cdot 10^{-4}$	$0.779064 \cdot 10^{-6}$	$-0.676329 \cdot 10^{-15}$
1	$0.274672 \cdot 10^{-14}$	$-0.801540 \cdot 10^{-25}$	$-0.354291 \cdot 10^{-7}$	$0.593088 \cdot 10^{-12}$	$0.502416 \cdot 10^{-20}$
2	$0.466067 \cdot 10^{-17}$	$0.277771 \cdot 10^{-24}$	$0.362433 \cdot 10^{-11}$	$0.144315 \cdot 10^{-14}$	$-0.676328 \cdot 10^{-23}$
3	$-0.915997 \cdot 10^{-19}$	$-0.509239 \cdot 10^{-26}$	$0.676280 \cdot 10^{-13}$	$0.499107 \cdot 10^{-17}$	$0.840580 \cdot 10^{-25}$
4	$0.137211 \cdot 10^{-21}$	$0.150716 \cdot 10^{-28}$	$0.402329 \cdot 10^{-14}$	$0.333296 \cdot 10^{-19}$	$-0.743479 \cdot 10^{-27}$
5	$0.413880 \cdot 10^{-23}$	$0.277737 \cdot 10^{-30}$	$-0.164076 \cdot 10^{-16}$	$0.127005 \cdot 10^{-21}$	$-0.231884 \cdot 10^{-29}$

Table 3: Fitting coefficients for the multivariate Taylor expansion (4) to the real part of the index of refraction over the $4.35 \leq 1/\tilde{\nu} \leq 5.3$ μm range. $T_{\mathrm{ref}} = (273.15 + 16)$ K, $p_{\mathrm{ref}} = 74400$ Pa, $H_{\mathrm{ref}} = 10$ %, and $\tilde{\nu}_{\mathrm{ref}} = 10^4/4.8$ cm^{-1}.

i	$c_{i\mathrm{ref}}$ / cm^i	c_{iT} / cm^{i}K	c_{iTT} / [cm^{i}K^2]	c_{iH} / [cm^i/%]	c_{iHH} / [cm^i/%^{2}]
0	$0.199315\cdot10^{-3}$	$0.588100\cdot10^{-1}$	-4.35744	$-0.192949\cdot10^{-7}$	$0.408600\cdot10^{-12}$
1	$0.345469\cdot10^{-9}$	$-0.155501\cdot10^{-5}$	$0.695383\cdot10^{-2}$	$0.301563\cdot10^{-10}$	$0.335127\cdot10^{-15}$
2	$-0.275079\cdot10^{-12}$	$0.215124\cdot10^{-8}$	$-0.934212\cdot10^{-5}$	$-0.404488\cdot10^{-13}$	$-0.449017\cdot10^{-18}$
3	$0.394628\cdot10^{-15}$	$-0.346113\cdot10^{-11}$	$0.147345\cdot10^{-7}$	$0.638909\cdot10^{-16}$	$0.709015\cdot10^{-21}$
4	$-0.568440\cdot10^{-17}$	$0.262426\cdot10^{-14}$	$-0.181787\cdot10^{-10}$	$-0.777591\cdot10^{-19}$	$-0.875601\cdot10^{-24}$
5	$0.164566\cdot10^{-19}$	$-0.137275\cdot10^{-16}$	$0.839618\cdot10^{-13}$	$0.326926\cdot10^{-21}$	$0.366678\cdot10^{-26}$
i	c_{ip} / [cm^i/Pa]	c_{ipp} / [cm^i/Pa^2]	c_{iTH} / [cm^{i}K/%]	c_{iTp} / [cm^{i}K/Pa]	c_{iHp} / [cm^i/(% Pa)]
0	$0.268194\cdot10^{-8}$	$-0.462961\cdot10^{-16}$	$0.932062\cdot10^{-4}$	$0.778082\cdot10^{-6}$	$0.676328\cdot10^{-15}$
1	$0.699105\cdot10^{-15}$	$-0.509592\cdot10^{-21}$	$-0.146713\cdot10^{-6}$	$0.219582\cdot10^{-12}$	$0.205797\cdot10^{-19}$
2	$0.160109\cdot10^{-17}$	$0.661976\cdot10^{-26}$	$0.196925\cdot10^{-9}$	$0.581470\cdot10^{-15}$	$-0.447923\cdot10^{-22}$
3	$-0.306913\cdot10^{-20}$	$-0.962125\cdot10^{-27}$	$-0.310258\cdot10^{-12}$	$-0.187918\cdot10^{-17}$	$0.587601\cdot10^{-25}$
4	$-0.665006\cdot10^{-22}$	$-0.509172\cdot10^{-29}$	$0.380521\cdot10^{-15}$	$-0.198580\cdot10^{-19}$	$-0.164252\cdot10^{-28}$
5	$0.179278\cdot10^{-24}$	$0.138849\cdot10^{-31}$	$-0.167780\cdot10^{-17}$	$0.587499\cdot10^{-22}$	$-0.125604\cdot10^{-30}$

Table 4: Fitting coefficients for the multivariate Taylor expansion (4) to the real part of the index of refraction over the $7.5 \le 1/\tilde\nu \le 14.1$ μm range. $T_{\mathrm{ref}} = (273.15+16)$ K, $p_{\mathrm{ref}} = 74400$ Pa, $H_{\mathrm{ref}} = 10$ %, and $\tilde\nu_{\mathrm{ref}} = 10^4/10.1$ cm^{-1}.

i	$c_{i\mathrm{ref}}$ / cm^i	c_{iT} / cm^{i}K	c_{iTT} / [cm^{i}K^2]	c_{iH} / [cm^i/%]	c_{iHH} / [cm^i/%^{2}]
0	$0.199325\cdot10^{-3}$	$0.588128\cdot10^{-1}$	-4.35385	$-0.192953\cdot10^{-7}$	$0.354836\cdot10^{-12}$
1	$0.351920\cdot10^{-9}$	$-0.155280\cdot10^{-5}$	$0.695337\cdot10^{-2}$	$0.301547\cdot10^{-10}$	$0.335173\cdot10^{-15}$
2	$-0.251950\cdot10^{-12}$	$0.215994\cdot10^{-8}$	$-0.934426\cdot10^{-5}$	$-0.404545\cdot10^{-13}$	$-0.449218\cdot10^{-18}$
3	$0.342939\cdot10^{-15}$	$-0.349269\cdot10^{-11}$	$0.147416\cdot10^{-7}$	$0.639037\cdot10^{-16}$	$0.709130\cdot10^{-21}$
4	$-0.674683\cdot10^{-17}$	$0.229638\cdot10^{-14}$	$-0.181063\cdot10^{-10}$	$-0.774951\cdot10^{-19}$	$-0.874946\cdot10^{-24}$
5	$0.193462\cdot10^{-19}$	$-0.127486\cdot10^{-16}$	$0.837474\cdot10^{-13}$	$0.326208\cdot10^{-21}$	$0.367001\cdot10^{-26}$
i	c_{ip} / [cm^i/Pa]	c_{ipp} / [cm^i/Pa^2]	c_{iTH} / [cm^{i}K/%]	c_{iTp} / [cm^{i}K/Pa]	c_{iHp} / [cm^i/(% Pa)]
0	$0.268214\cdot10^{-8}$	$-0.185185\cdot10^{-15}$	$0.932105\cdot10^{-4}$	$0.779014\cdot10^{-6}$	$-0.154589\cdot10^{-14}$
1	$0.786389\cdot10^{-15}$	$-0.466289\cdot10^{-22}$	$-0.146705\cdot10^{-6}$	$0.245635\cdot10^{-12}$	$0.354590\cdot10^{-19}$
2	$0.191406\cdot10^{-17}$	$0.628533\cdot10^{-24}$	$0.196952\cdot10^{-9}$	$0.691332\cdot10^{-15}$	$-0.310628\cdot10^{-22}$
3	$-0.376823\cdot10^{-20}$	$-0.729100\cdot10^{-27}$	$-0.310317\cdot10^{-12}$	$-0.230009\cdot10^{-17}$	$0.544928\cdot10^{-25}$
4	$-0.808732\cdot10^{-22}$	$-0.370284\cdot10^{-29}$	$0.379246\cdot10^{-15}$	$-0.241429\cdot10^{-19}$	$-0.408192\cdot10^{-34}$
5	$0.218365\cdot10^{-24}$	$-0.400643\cdot10^{-35}$	$-0.167435\cdot10^{-17}$	$0.716419\cdot10^{-22}$	$-0.579708\cdot10^{-31}$

Table 5: The coefficients as in Table 4 with the CO_2 contents increased to 450 ppmv.

i	$c_{i\mathrm{ref}}$ / cm^i	c_{iT} / cm^{i}K	c_{iTT} / [cm^{i}K^2]	c_{iH} / [cm^i/%]	c_{iHH} / [cm^i/%^{2}]
0	$0.198865 \cdot 10^{-3}$	$0.613218 \cdot 10^{-1}$	-15.5515	$-0.670279 \cdot 10^{-7}$	$-0.222224 \cdot 10^{-12}$
1	$0.300829 \cdot 10^{-8}$	$-0.159446 \cdot 10^{-4}$	$0.724229 \cdot 10^{-1}$	$0.300121 \cdot 10^{-9}$	$0.333050 \cdot 10^{-14}$
2	$-0.219393 \cdot 10^{-10}$	$0.135071 \cdot 10^{-6}$	$-0.672405 \cdot 10^{-3}$	$-0.231011 \cdot 10^{-11}$	$-0.254988 \cdot 10^{-16}$
3	$0.145838 \cdot 10^{-12}$	$-0.848985 \cdot 10^{-9}$	$0.417406 \cdot 10^{-5}$	$0.144901 \cdot 10^{-13}$	$0.160280 \cdot 10^{-18}$
4	$0.128297 \cdot 10^{-14}$	$-0.864198 \cdot 10^{-11}$	$0.489660 \cdot 10^{-7}$	$0.128340 \cdot 10^{-15}$	$0.140405 \cdot 10^{-20}$
5	$-0.119166 \cdot 10^{-16}$	$0.805312 \cdot 10^{-13}$	$-0.436679 \cdot 10^{-9}$	$-0.124101 \cdot 10^{-17}$	$-0.136231 \cdot 10^{-22}$
i	c_{ip} / [cm^i/Pa]	c_{ipp} / [cm^i/Pa^2]	c_{iTH} / [cm^{i}K/%]	c_{iTp} / [cm^{i}K/Pa]	c_{iHp} / [cm^i/(% Pa)]
0	$0.268216 \cdot 10^{-8}$	$0.743978 \cdot 10^{-21}$	$0.327197 \cdot 10^{-3}$	$0.778496 \cdot 10^{-6}$	$-0.579710 \cdot 10^{-15}$
1	$0.121619 \cdot 10^{-14}$	$-0.648495 \cdot 10^{-20}$	$-0.148970 \cdot 10^{-5}$	$0.496563 \cdot 10^{-12}$	$0.946862 \cdot 10^{-19}$
2	$0.528001 \cdot 10^{-17}$	$-0.320666 \cdot 10^{-22}$	$0.124790 \cdot 10^{-7}$	$0.271761 \cdot 10^{-14}$	$-0.152174 \cdot 10^{-20}$
3	$0.771914 \cdot 10^{-19}$	$-0.230138 \cdot 10^{-24}$	$-0.781931 \cdot 10^{-10}$	$-0.622421 \cdot 10^{-16}$	$0.130821 \cdot 10^{-22}$
4	$0.750481 \cdot 10^{-21}$	$0.748180 \cdot 10^{-28}$	$-0.789636 \cdot 10^{-12}$	$-0.160509 \cdot 10^{-18}$	$0.975847 \cdot 10^{-25}$
5	$-0.872808 \cdot 10^{-25}$	$0.102061 \cdot 10^{-28}$	$0.734001 \cdot 10^{-14}$	$0.789747 \cdot 10^{-20}$	$-0.104734 \cdot 10^{-26}$

Table 6: Fitting coefficients for the multivariate Taylor expansion (4) to the real part of the index of refraction over the $16 \le 1/\tilde{\nu} \le 28$ μm range. $T_{\mathrm{ref}} = (273.15 + 16)$ K, $p_{\mathrm{ref}} = 74400$ Pa, $H_{\mathrm{ref}} = 10$ %, and $\tilde{\nu}_{\mathrm{ref}} = 10^4/20$ cm^{-1}.

3 REFRACTIVE INDEX IN THE DELAY LINE TUNNEL

3.1 Precision in the "Theory"

For the theory [100], the refractive index drops by $4.392 \cdot 10^{-7}$ from $\lambda = 1.32$ to 2.2 μm, for the fit [22], it drops slightly less, $4.249 \cdot 10^{-7}$, which is already apparent from Fig. 1.

Not knowing a priori which of these numbers is more appropriate would introduce an uncertainty of about $1.4 \cdot 10^{-8}$ in the refractive index as one tries to tries to "extrapolate" the OPD seen by the metrology to the OPD seen by the star light, and this relative uncertainty is already about 300 times the relative change in the path difference of $4.8 \cdot 10^{-11}$ [8, §2.2.3], induced by a 10 μarcsec tilt. (Since the absolute error in the OPD scales proportional to the baseline and the differential path difference between the PS and the SS scales proportional to the *projected* baseline, it is convenient to look at the relative errors here, because the actual baseline length approximately drops out in this case. From the instrument control point of view the following numbers can be relaxed a bit, if the star is not at the zenith.)

Let us use the relative accuracy of $4.8 \cdot 10^{-11}$ as a guidance for the estimates below, keeping in mind that

- this may be too optimistic since the full error budget sets the bounds, and some of the allowable error is already claimed by other, uncorrelated sources.
- this may be too pessimistic since it focuses on a nominally frozen setup of a single baseline, and does does not acknowledge any statistical cancellation of errors by repeated measurements.

This sets the stage of what precision is required in the knowledge about the "generic" refraction indexes of the molecules in the tunnel air. To quote [22]: "*precise modern interferometric refractometers have been found to have uncertainties (at the 1σ level) of 1–3$\times 10^{-8}$ and disagree by approximately the same amount when the same sample of air is measured. These results suggest that absolute uncertainties of better than 5×10^{-8} are unlikely to be achievable by direct measurement, especially over long or nonuniform paths.*"

Since [22] models the entire dry air component, including CO_2, by two resonances at 65 and 132 nm, is is interesting to see that an exchange of each CO_2 molecule by an O_2 molecule in the theory of [100] would already account for $2 \cdot 10^{-9}$ of the aforementioned discrepancy of $1.5 \cdot 10^{-8}$, which means that the drag of the CO_2 resonances in the infrared cannot be neglected.

Rank et al. [131] measured $(27785.6 - 27321.9) \cdot 10^{-8} = 4.637 \cdot 10^{-6}$ for the difference of the refractive index of dry, CO_2 free air between 546.2249 nm and 1.529977 μm at a pressure of 760 mm Hg and 15°C. The theory presented here produces a value of $4.624 \cdot 10^{-6}$ for the same parameters.

The refractivity measurements of pure carbon dioxide by Old et al. [117] are $\approx 30\%$ larger than the theory used here (which is based on the HITRAN database and [121]). Because the CO_2 molecule has a $\approx 58\%$ larger refractivity than the average air molecule in the H band and builds 370 ppmv of the air, an ad-hoc correction would increase the theory of Fig. 1 by $\approx 4.4 \cdot 10^{-8}$.

3.2 Requirements on the Knowledge of Ambient Parameters

3.2.1 Principles of Measurement

The susceptibility $n-1$ is itself (to the precision needed here) built of sums over products of the molecule concentrations by the "intrinsic" physical properties (dynamic polarizabilities) of the molecules. Excellent knowledge of the optical properties of the gases can easily become futile if not matched by the same relative precision in the metrology of the gas densities (since the relative error in the products is the sum of the relative errors in the factors). This point has already been stressed by Ciddor [22].

From the outset, the relative error in the molecule concentrations is (from the ideal gas equation) the sum of the relative errors in the (partial) pressure p and in the temperature T.

As an alternative to this way of extrapolation of the index of refraction via computation from a formula, in which measured concentrations are an input, one could think of an implicit measurement of the tunnel gas densities with the other laser systems, exploiting their inherent accuracy:

- The gas densities at the PRIMA DDL table can be measured since the the PRIMA laser of the DDL control loop surveys a very local air path close to the table of the Differential Delay Line http://www.mpia-hd.mpg.de/PRIMA-DDL/s (DDLs). This is done by (ab)use of the vacuum equipment and means to measure the differential delay between the DDLs once in vacuum and once in the ambient air. Some obstacles to this are
  1. such a pressure cycle may be unrealistic for various reasons (too slow, or producing itself turbulence and convection).
  2. the accuracy of the results depends on the quality of the "reference" state (here, the vacuum), and is only reproducible to the degree that the vacuum pressure is well known. Since only a moderate vacuum is foreseen, the vacuum pressure might be known no better than the actual ambient pressure, and no advantage be left [29, §4.10.2.4].
  3. Extrapolation from the few centimeters of air path close to the PRIMA DDL to the tens of meter in the DL tunnel seems adventurous.
- use the third wavelength of the VLTI metrology laser system [81], and use the relative OPD at the third and the PRIMA metrology wavelength, which also becomes proportional to the gas filling, to deduce the air density from knowledge of the refractive index at this third frequency. An inherent problem of using any VLTI DL metrology information is that it covers a path between the VLTI DL mirrors and the primary or secondary, whereas the PRIMA metrology starts from a point on the PRIMA sensor table in the interferometric laboratory, and therefore includes (integrates over) some additional environment. Also, the super-heterodyne phase detection of the PRIMA metrology and the associated software is only tuned to measure the differential optical path length, but not the two individual paths [76]. There are two variants of this idea:
  1. One "defines" two fixed points in the delay line tunnel, for example by two light barriers that run perpendicular to the DL rails. (The "coarse" metrology of the VLTI Delay Lines (DLs) could serve the same purpose but is not providing a resolution better than 30 μm [169].) One then measures the optical path length at the actual (variable) ambient conditions by running with the DL carriages through these and counting the VLTI DL metrology fringes. The advantages are
     - this can span a large portion of the actual, relevant air path

  - the computer infrastructure ought to be already there (in form of the reflective memory network [173, Fig 2.1])

  and the disadvantages

  - this is correlated to any error labeled as "tunnel concrete structure instability" in the PRIMA error budget. Fortunately it seems as there is some automated cancellation here: if the vacuum path between the light barriers is extended in the course of some ground movement, a new measurement will actually "see" the higher areal density, though it does not know whether this means a higher air pressure or a change of the geometry.

2. One drives the VLTI delay line over some typical range and monitors the optical path difference at the same time with the PRIMA and the VLTI metrology lasers. The ratio of these path differences is proportional to the air density. The disadvantages are

   - The "signal" of this measurement is good (larger) if the difference between the wavelengths of the lasers is large, but this may put more stress on the theory since the contributions (dispersions) of the air constituents to the total diffraction are not the same at all wavelengths.

   and the advantages

   - One can (in principle) detect even gradients in the refractive index along the path accessible with the VLTI carriages.

   The idea of transforming the entire facility to an expensive hygrometer by using two different laser wavelengths is not new [1].

A third alternative is the use of the delay line systems themselves as Michelson interferometers. The finite stroke of the PRIMA DDLs, 6.5 cm mechanically and 13 cm in OPD, gives it a resolution of $\lambda/\Delta\lambda \approx 1 \cdot 10^5$ at 2.2 μm, which allows a measurement of the susceptibility with a relative precision of only 0.04; the large OPD of the VLTI DLs, however, provides any desirable resolution we may call for, if one manages to move a gas cell with a well known reference gas (which could be the vacuum) at a well known pressure in and out of the beams.

3.2.2 PRIMA's differential point of view

Supposed one would face the problem of calculating the OPL or OPD in one of the VLTI beams from knowledge typically acquired with the 1.3 μm laser of the PRIMA metrology and auxiliary sensors. (I assume that the value of 1.7 μm quoted on page 14 of [8] is wrong.) This would be

- equivalent to defining the zenith angle of a star as sketched in Fig. 7,
- and equivalent to the task of blind tracking a K band star assuming that the ZOPD is given (tracked) at the same time for a J-Band star,
- and may resurface in the baseline calibration program [31], which is relaxed with respect to the requirement of $\Delta b \approx 50$ μm, a relative accuracy of $2.5 \cdot 10^{-8}$, but (apparently) wants to reduce this from some metrology measurements to the vacuum. Since this baseline calibration will probably be based on an external calibration "on the sky" [87, 91, 149], this issue is not touched here further.

As $n-1$ is of the order of $2\cdot 10^{-4}$, an absolute precision of 5 nm over 100 m would require a relative precision in $n-1$ of $\approx 5\cdot 10^{-11}$, which could only be achieved if the molecular concentrations (of the dominant gas species) were known to $2\cdot 10^{-7}$, which is illusory in both p and T.

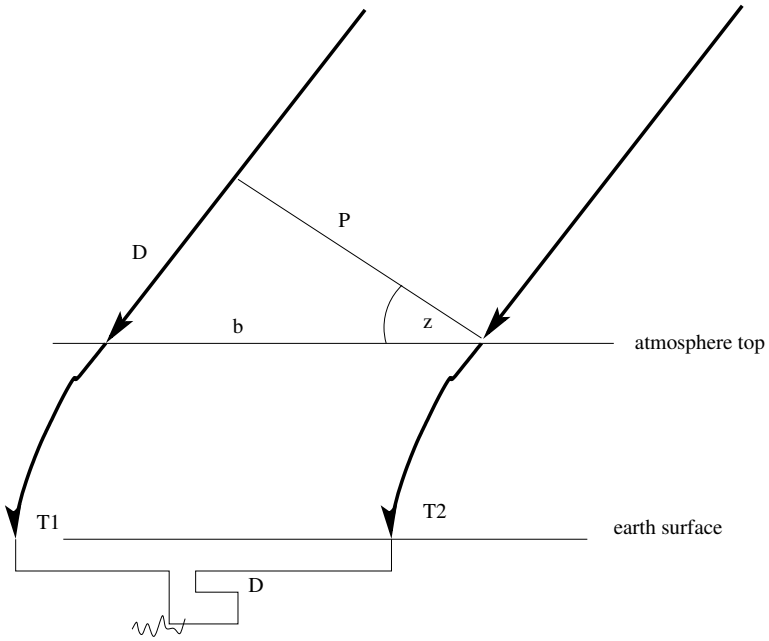

Figure 7: The standard model of delay line correction for a star at zenith angle z: The optical path difference D shows up once in the vacuum above telescope 1, and is added for telescope 2 on the ground (at some local index of refraction). The atmosphere is horizontally homogeneous and the earth flat; therefore there is no correction needed for the ray path curvature induced by any vertical gradient of the index of refraction through the atmosphere, because these two paths match each other at each height above ground.

The philosophy of the astrometric approach is to determine a difference in these angles between a primary (reference) star and a science (secondary) star rather than to determine the absolute angles, which relaxes the requirements tremendously, overall by a typical factor of X/D, where $|X| \le 11.7$ cm is the differential optical delay and D the OPD of any one of the two stars. (This maximum value of $X=\tau b$ corresponds to the maximum baseline of $b=202$ m between AT station B5 and J6 in conjunction with the maximum star separation of $\tau = 2$ arcmin $= 5.8\cdot 10^{-4}$ rad admitted by the STS, observed at one of the two "favorable" times of the day that maximize the X amplitude. This implies that the field rotation induced by a "hybrid" mixture of telescopes north and south of the DLs is of no concern [53, 127]. The proposal of [47] has baselines no longer than 145 m.) This does not actually add any new aspect to the error budget, and we recall the estimates of the previous section in a more formal way. Δ denotes the absolute error or difference in a parameter, and $0<\varepsilon\le 1$ (but not ϵ) the relative error. "Error" and "correction" are synonymous to some degree (the error in the correction is what generates a term in the error budget).

The measurement principle and reconstruction of the external delay D is to localize the fringe maximum on the ground, changing the tunnel geometric path length D_t such that the phase $n(k)kD_t - kD$ becomes zero, aiming at $n(k)D_t = D$ in

$$I(D_t) = \int e(k)\{1+\cos[n(k)kD_t - kD]\}dk, \tag{5}$$

Astrometry in the K band wants to determine the differential OPD $D_{\rm PS} - D_{\rm SS} = n_{\rm PS}(K)D_{t\rm PS} - n_{\rm SS}(K)D_{t\rm SS}$, where the argument of n represents the infrared band. The IR metrology counts fringes in the J-band and measures $2[n_{\rm PS}(J)D_{t\rm PS} - n_{\rm SS}(J)D_{t\rm SS}]$, where the factor of 2 indicates the round trip from the FSU to the RR3 and back. The dispersion correction assesses the difference—assuming the factor of 2 is exact which means that the asymmetric beam bending of Sect. 3.3 does not play a role etc—which is

$$[n_{\rm PS}(K) - n_{\rm PS}(J)]D_{t\rm PS} - [n_{\rm SS}(K) - n_{\rm SS}(J)]D_{t\rm SS}. \tag{6}$$

The refractivity can be expanded to lowest order at some wave number chromatically, $n_{\rm PS}(K) = n_{\rm PS}(J) + \Delta k \partial n_{\rm PS}/\partial k$, where $\Delta k \partial n_{\rm PS}/\partial k \approx 4.4 \cdot 10^{-7}$ with an error of less than $5 \cdot 10^{-8}$ (Fig. 1). This allows us to write the correction as $\Delta k[\partial n_{\rm PS}(K)/\partial k D_{t\rm PS} - \partial n_{\rm SS}(K)/\partial k D_{t\rm SS}]$. Furthermore there may be a lateral spatial gradient, most probably implied by a temperature gradient, $n_{\rm SS}(K) = n_{\rm PS}(K) - d\nabla n(K)$, where $d = 0.24$m is the beam separation. This re-writes the correction as $X\Delta k \partial n_{\rm PS}(K)/\partial k + D_{t\rm SS} d\Delta k \nabla \partial n_{\rm SS}(K)/\partial k$.

This splits the correction into a chromatic term proportional to the DOPD X of up to 12 cm, and a "lateral" gradient term proportional to the full delay D of a single beam.

3.2.2.1 Chromatic Term The error in the optical path differences for the primary or secondary star is

$$\Delta D = \Delta n L, \tag{7}$$

where L is the vacuum path length difference. The error in the differential optical delay is (neglecting all turbulence effects)

$$\Delta X_{2.2} = \Delta(nl) = l\Delta n_{2.2} + n_{2.2}\Delta l, \tag{8}$$

where the error Δl in the mechanical position of the DDLs is either 5 nm according to the specifications of the mechanical precision if the DDLs are operating in vacuum, or it is the error $\varepsilon_l = \varepsilon_{X_{0.64}} + \varepsilon_{n_{0.64}}$ induced by estimating it from the optical path difference of the internal feedback operating at the HeNe wavelength if the DDLs are operating under ambient air [74]. Here the indices indicate the wavelengths of the laser or science lights. Because it is more difficult to estimate the absolute refractive index of the ambient air at the HeNe wavelength than to interpolate from $\lambda = 1.3$ to 2.2 μm, $\varepsilon_{n_0.64} \gg \varepsilon_{n_{2.2}/n_{1.3}}$, we assume that the differential optical delay is computed from the four path lengths of the IR metrology laser, with the advantage that this includes all breathing modes of the tunnel system induced by seismic activities, and the snapshot of all (relative) turbulences in the beams:

$$\Delta X_{2.2} = \Delta(n_{2.2}X_{1.3}/n_{1.3}), \tag{9}$$

$$\varepsilon_{X_{2.2}} = \varepsilon_{n_{2.2}/n_{1.3}} + \varepsilon_{X_{1.3}}. \tag{10}$$

Leaving aside the relative error from the IR metrology system, which is not discussed here, the total relative error becomes

$$\varepsilon_{X_{2.2}} = \frac{1}{2}\Delta(\chi_{1.3} - \chi_{2.2}), \tag{11}$$

half of the absolute error in the difference between the susceptibilities. (The correction would go beyond this linear order in the differences.) The susceptibilities are sums over gas species g, which contribute by products of wavelength-independent number densities and what we roughly may call molecular dynamic polarizabilies α,

$$\chi = \sum_g f_g \alpha_g, \tag{12}$$

$$\varepsilon_{X_{2.2}} = \frac{1}{2}\sum_g \Delta(f_g(\alpha_{g1.3}-\alpha_{g2.2})) = \frac{1}{2}\sum_g [(\alpha_{g1.3}-\alpha_{g2.2})f_g\varepsilon_{f_g} + f_g\Delta(\alpha_{g1.3}-\alpha_{g2.2})]. \quad (13)$$

The first term $\propto \varepsilon_{f_g}$ is an error from the available measured densities, due to errors in the partial pressures p and common temperature T,

$$\varepsilon_{f_g} = \varepsilon_{p_g} + \varepsilon_T \quad (14)$$

and the second $\propto \Delta(\alpha_{g1.3}-\alpha_{g2.2})$ an error in the "theory."

A maximum error of 5 nm over $X = 13$ cm demands $\varepsilon_{X_{2.2}} < 3.8\cdot 10^{-8}$, and one would like to keep both terms individually below $1.9\cdot 10^{-8}$. Since $\frac{1}{2}\sum_g(\alpha_{g1.3}-\alpha_{g2.2})f_g$ is of the order of $4.4\cdot 10^{-7}$ as already stated in Sec. 3.1, and all important $\alpha_{g1.3}-\alpha_{g2.2}$ have the same sign, this can definitely be enforced for the first, "experimental" term by keeping the sum of all relative errors ε_{f_g} below 0.04, for example. Actually, the contributions to the dispersions are of different importance, as shown in the global accounting of "dry" and "water" constituents in the previous paragraph; in these cases one can trade some errors for others, and should demand that the relative errors are inversely proportional to the weights $(\alpha_{g1.3}-\alpha_{g2.2})f_g$. The outcome for the extrapolation of the J-band optical path difference to the K band is that the relative error in the humidity (water vapor density) is allowed to be about 10 to 20 times as large as the relative error in the remaining density (pressure).

Characteristic numbers are given in Tab. 7: The correction in the relative OPD position of the differential delay line is of the order of 53 nm (maximum, since referring to the full differential stroke) to adapt to the different wavelengths of the metrology and science beam, and varies by a few nanometer if the ambient parameters change within reasonable bounds. In the first part of the table, increase of the temperature at constant pressure means to decrease the molecule density, resulting in smaller ΔX. In the second part, exchange of the average dry air molecule by a water molecule and increase of the humidity results in an increase of the correction (meaning the dispersion of the single water molecule is stronger than the dispersion of the average air molecule in this spectral region, recall the factor 0.14 mentioned above). In the third part, increase of the pressure at constant temperature increases the molecule densities and therefore increases ΔX.

One may switch from relative to absolute humidity and fit the change in the refractive index difference from 1.3 to 2.25 μm as given in Tab. 8.

The calculations shown above must be replaced by an equivalent calculation on the dispersion in the DDL window material, if the DDL uses its "vacuum" option [12, 72].

Remark: The transition from the IR laser wavelength to the science wavelength with (6) does *not* need an input in form of the temperature/humidity gradients like shown in Fig. 8. The delays $D_{t\mathrm{PS}}$ and $D_{t\mathrm{SS}}$ are actually path length differences to telescope 1 and 2, and (6) should be split into

$$\underbrace{[n_{1\mathrm{PS}}(K)L_{t1\mathrm{PS}} - n_{2\mathrm{PS}}(K)L_{t2\mathrm{PS}}]}_{n_{PS}(K)D_{tPS}} - \underbrace{[n_{1\mathrm{SS}}(K)L_{t1\mathrm{SS}} - n_{2\mathrm{SS}}(K)L_{t2\mathrm{SS}}]}_{n_{SS}(K)D_{tSS}} - [K\to J] \quad (15)$$

to investigate this point. We see that at each piece along the way to each telescope, the terms $n_{1\mathrm{PS}}(K)L_{t1\mathrm{PS}} - n_{1\mathrm{SS}}(K)L_{t1\mathrm{SS}}$ and $n_{2\mathrm{PS}}(K)L_{t2\mathrm{PS}} - n_{2\mathrm{SS}}(K)L_{t2\mathrm{SS}}$ cancel for any temperature/humidity profile along the path, and only the local correction $\propto X$, the differential delay near the DDL remains as already discussed above. (It is not clear whether the temperature sensors of the DDL [44, 90] will be funneled into the raw data set and made available to the DRS.) The same cancellation happens within the term in the J band (IR metrology). This means that *purely longitudinal* gradients in the refractivity do *not* need a color correction of the IR metrology reading for dual-beam astrometry.

T / °C	P / hPa	H / %	ΔX / nm
12	747	10	-53.2
14	747	10	-52.9
16	747	10	-52.7
18	747	10	-52.5
16	747	5	-52.2
16	747	10	-52.7
16	747	20	-53.6
16	747	40	-55.4
16	747	50	-56.3
16	736	20	-52.8
16	741	20	-53.2
16	746	20	-53.5
16	751	20	-53.9
16	756	20	-54.2

Table 7: Estimated optical path difference ΔX between $\lambda = 1.319$ μm and $\lambda = 2.25$ μm observed at an optical path difference $X = 12$ cm as a function of temperature T, total air pressure p, and humidity H. Seasonal temperature variations are reported in Figs. 31 to 34, [79] and [70, Fig. 8]. Pressures below 0.726 atm (736 hPa) are indicative of storm.

derivative		units
$\partial(n_{2.25} - n_{1.3})/\partial T$	$1.5 \cdot 10^{-9}$	1/K
$\partial(n_{2.25} - n_{1.3})/\partial f_w$	$-1.0 \cdot 10^{-7}$	$1/(\mathrm{mol/m^3})$
$\partial(n_{2.25} - n_{1.3})/\partial p$	$-5.8 \cdot 10^{-12}$	1/Pa

Table 8: First partial derivatives of the difference of the indices of refraction at 1.32 and 2.25 μm w.r.t. temperature, absolute humidity and air pressure near typical Paranal tunnel values.

3.2.2.2 Lateral Gradient Term This term produces an error if lateral temperature/humidity gradients lead to a bias over the distance of $d = 0.24$ m where $D < 202\mathrm{m} \cdot \sin 60° \approx 174$ m for baselines up to 202 m and zenith angles up to 60 deg. (The actual maximum delay is smaller, roughly 150 m with the G1-J6 baseline, because the finite range of the MDL positions does not allow access to all sky positions of the B5-J6 baseline; see the `issgui*` files in http://www.strw.leidenuniv.nl/~mathar/vlti/.) For each Kelvin difference in the beam temperatures, $\Delta T/T \approx 1/280$, and $n - 1 \approx 2 \cdot 10^{-4}$, we have $d\Delta k \partial \nabla n/\partial k \approx \Delta T/T \Delta k \partial n/\partial k$, which remains smaller than $\Delta T \cdot 5 \cdot 10^{-8}/(280\ \mathrm{K})$. (For simplicity we may assume a homogeneous gas chemistry and no pressure gradients, $d\nabla n = \Delta T \partial n/\partial T \approx (n-1)\Delta T/T$.) The error in the correction of the differential OPD is smaller than $\Delta T/\mathrm{K} \cdot 5 \cdot 10^{-8}/280 \cdot 174\mathrm{m} \approx 31\ \mathrm{nm} \Delta T/K$: A persistent beam temperature difference of 1°C along the entire dual beam path adds 31 nm.

This error term favors the use of small baselines. Assuming that modeling of the local temperature gradients is difficult, beam swapping (which adds two terms of different sign in ∇n but the same D) is a valuable technique to cancel this term to high degree.

3.2.3 Implications To Temperature/Humidity Sensor Network

Each change in the humidity by 1 mole/m^3 changes the refractivity in the K band by $5.2{\cdot}10^{-6}$ to $5.3{\cdot}10^{-6}$, depending on where in the K band one actually looks at. Typical variations of the humidity

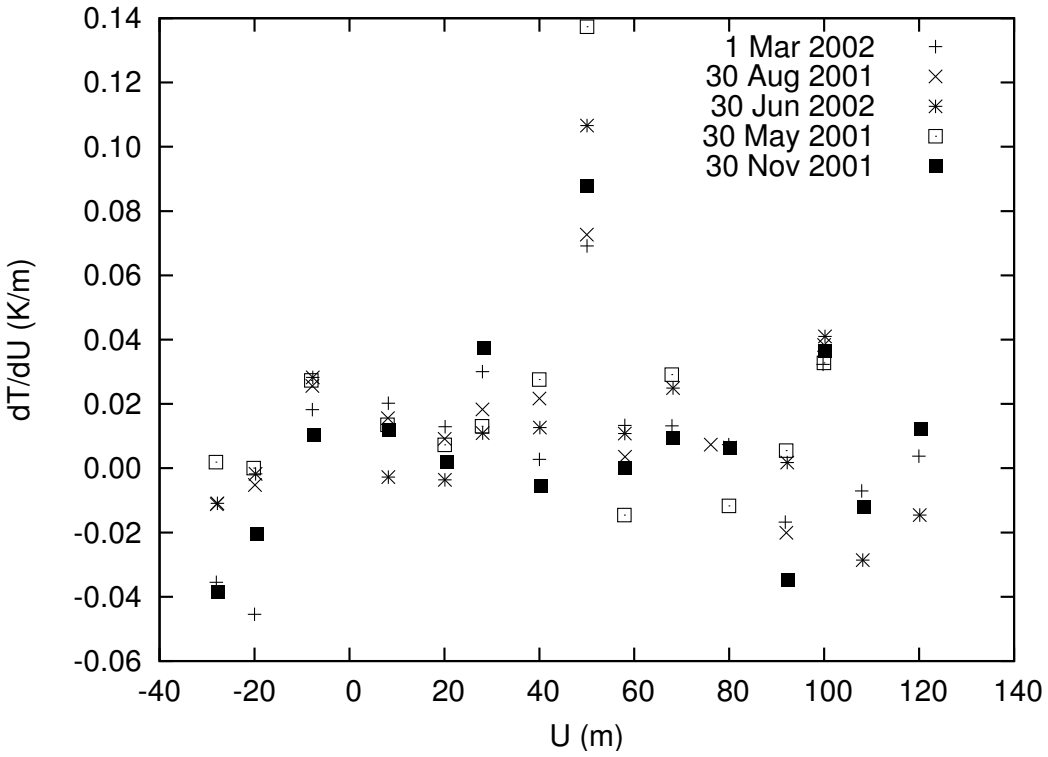

Figure 8: These temperature gradients in units of K/m along the VLTI tunnel U-coordinate in meter are the divided differences of the data plotted in Fig. 8 of [79].

in the VLTI tunnel are of the order of 0.001 to 0.004 mole/m^3 within time intervals of 10 min (Fig. 40). At delays D of up to 170 m (baseline $b = 202$ m at $z = 60$ deg zenith with Eq. (34)) these fluctuations induce changes in the OPD of 900 nm–3.6 μm within 10 min, and even larger changes within 30 min. Temperatures are of similar importance: a typical variation in temperature of 0.04°C in 10 minutes changes the air density by a factor of $1.4{\cdot}10^{-4}$, therefore the refractivity by $3{\cdot}10^{-8}$ and the OPD by up to 5 μm.

The astrometric data reduction requires DOPD accuracies of typically 5 nm. Each change in the humidity of 1 mole/m^3 changes the water-induced refractivity between the metrology laser and the K band by $1.8{\cdot}10^{-7}$ or $0.8{\cdot}10^{-7}$, depending on which place in the K band one looks at. Assuming the case of $1.8{\cdot}10^{-7}$ at $\lambda = 2.4$ μm, a change in humidity of 0.004 mole/m^3 within 10 minutes, and $D = 170$ m, we get a correction of the IR metrology scale of 122 nm. In this case, reading humidities and temperatures must be done more frequently than once every 10 minutes. The sensor near M12 shown in Fig. 42 had a median of fluctuations of $8 \cdot 10^{-4}$ mole/m^3 in 5 min intervals, equivalent to corrections of 25 nm to the IR metrology, indicating again that the readings would have to be done faster than once every 5 minutes.

The cancellation effect of the longitudinal density gradients discussed with Eq. (15) does not apply to the color correction of the baseline calibration, which adds the term

$$[n_{1\mathrm{PS}}(K)L_{t1\mathrm{PS}} - n_{2\mathrm{PS}}(K)L_{t2\mathrm{PS}}] - [n_{1\mathrm{PS}}(J)L_{t1\mathrm{PS}} - n_{2\mathrm{PS}}(J)L_{t2\mathrm{PS}}] \tag{16}$$

to a single-beam measurement, here chosen to be the PS. The color correction $n_{1\mathrm{PS}}(K) - n_{1\mathrm{PS}}(J)$ changes by $\approx 1.8 \cdot 10^{-9}$ for each temperature difference of 1 K—the term $\Delta T/T \Delta k \partial n/\partial k$ from

Sec. 3.2.2.2. Eq. (16) integrates this value independently over the paths from the FSU to the two telescopes. The correction becomes larger if the D_t itself becomes larger and/or if the air/water density (temperature or humidity) along the path to one of the two telescopes differs from the parameters on the other path. (The one-way path lengths from the UT and AT stations to the PRIMA FSU are plotted in Fig. 9.) Supposed one would err in the temperature along the maximum path of

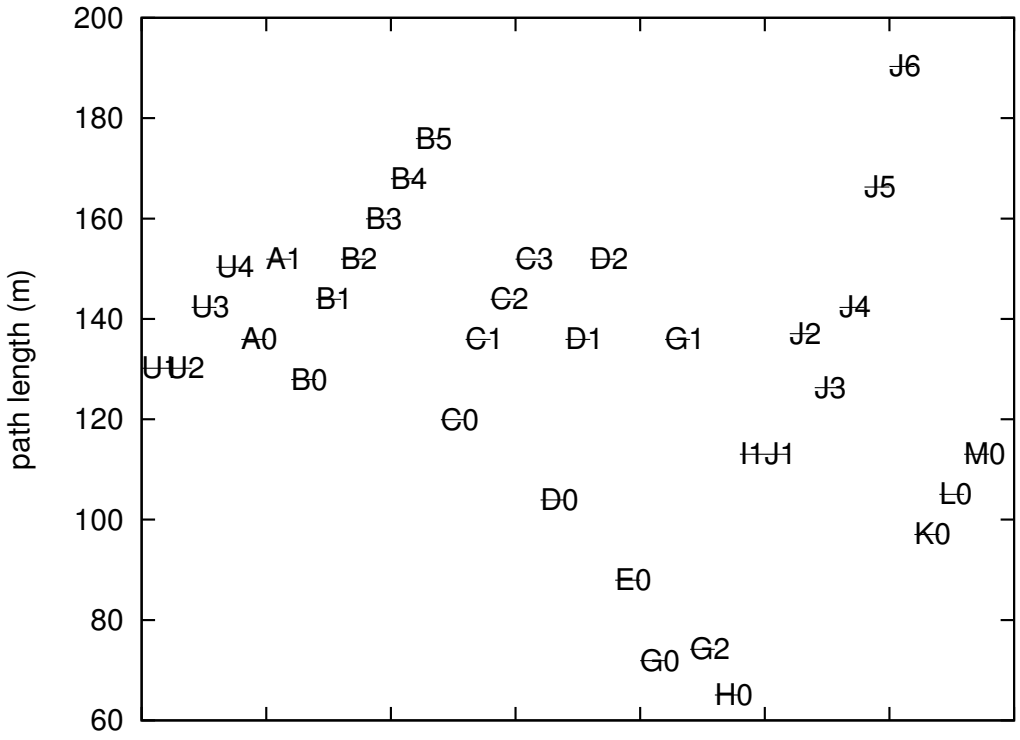

Figure 9: Estimated path lengths from the nominal station coordinate [177, Tab. 3-2][97] through the duct, to the reference position of the DL carriage [177, Tab. 3-3] passing by the BC, by the DDL, and ending at the nearest possible PRIMA feeding optics [111]. Depending on the application, one would add 19.8 m to these to incorporate the path from M1 up to the last mirror (M16) of the STS, as detailed in [162, App. A]. The maximum path length is 270 m for extreme positions of the DL carriage [127].

270 m to one telescope, the error in the correction (16) would amount to $1.8 \cdot 10^{-9} \cdot 270$ m $\approx 0.5\mu$m. This error in D is boosted by a factor $1/\sin z$ of (34), which stays below 11 assuming that baseline calibrations at $z < 5$ deg are avoided. Still, the error in b is well below the accuracy of $\approx 50\mu$m generally required for the baseline length.

3.3 Beam Curvatures in the Tunnel

3.3.1 Refractivity Gradient and One-Path Solution

A gradient of the refractive index tilted toward the line of sight bends beams ("mirage"). We consider the model of temperature gradients that induce linear deviations in the refractive index

$$n = n(x, y) = n_0 + xn_x + yn_y; \qquad \nabla n_{\mathbf{r}} = (n_x, n_y, 0) \tag{17}$$

relative to the point $(x, y) = (0, 0)$ where the light beam enters the delay line tunnel (Fig. 10). The Snell's law of refraction reads in this case

$$n(x, y) \sin \Psi = n_0 \frac{n_y}{\sqrt{n_x^2 + n_y^2}}, \tag{18}$$

where $\Psi = \arctan G - \arctan y'$ with $G \equiv n_y/n_x$ is the local tilt angle between the beam and the gradient of the refractive index, and $n_y/\sqrt{n_x^2 + n_y^2}$ the $\sin \Psi$ at the origin of coordinates. We solve the resulting first-order differential equation

$$n(G - y') = n_0 G \sqrt{1 + y'^2} \tag{19}$$

for the beam geometry $y' \equiv \partial y/\partial x$ with a power series ansatz with the boundary condition $y'(0) = y''(0) = 0$ to find

$$y \approx \frac{n_x G}{2n_0} x^2 - \frac{n_x^2 G}{3n_0^2} x^3 + \frac{n_x^3 G(G^2 + 6)}{24 n_0^3} x^4 - \frac{n_x^4 G(7G^2 + 12)}{60 n_0^4} x^5 + \cdots \tag{20}$$

(One can also deduce more formal implicit solutions by forming a product of two terms in y' as described in [64, §2 · 4] and introducing a coordinate $\eta = x + Gy$ as described in [64, §2 · 12] to obtain a separable first order differential equation in η and x.) If the gradients follows strictly the sides of the tunnel with no transverse component, $n_y = G = 0$, the beam stays straight: $y = 0$. Since $n_x x$ is not larger than $\approx 10^{-6}$ (see below), and G is of the order of 1, only the first term in Eq. (20) is relevant in practice. Then

$$y \approx \frac{n_y}{2n_0} x^2 \tag{21}$$

demonstrates that the path is approximately parabolic, and that the displacement is proportional to the temperature (density) gradient perpendicular to the path.

A temperature gradient $\partial T/\partial r \approx 2\text{K}/(100\text{ m})$ [79, Fig. 8] is equivalent to a density gradient of $[-p/(RT^2)](\partial T/\partial r)$ with the ideal gas law, where the absolute value of the prefactor is $\approx 0.11 \frac{\text{mole}}{\text{m}^4}/\frac{\text{K}}{\text{m}}$ at $p = 751$ hPa and $T = 285$ K. The product of the two numbers combines into some maximum air density gradient of $2.2 \cdot 10^{-3}$ mole/m^4, and at $1/\tilde{\nu} = 2.2$ μm, the gradient in the susceptibility is about $2.8 \cdot 10^{-8}$/m, the gradient in the refractive index $\nabla n \approx 1.4 \cdot 10^{-8}$/m at $n_0 \approx 1.0002044$. (Rule of thumb calculations can just assume that the relative change in the refractivity $n - 1$ equals the relative change in T at constant composition and pressure.) This is a rather optimistic value because the vertical temperature gradient can be about a factor of 5 larger [79, Fig. 10][51], and the design value [127, Tab. 3.7.2] in the VLTI laboratory is a factor of 2 larger. Various examples for propagation distances x and directional angles $\Psi_0 = \arctan n_y/n_x$ between the gradient and the main tunnel axis are shown in Fig. 11. The finite length of the delay line tunnel limits x to a theoretical maximum of about 140 m, the case of AT stations A0 or A1. The full truth is that the same effect is already present in any of the light ducts [48]. To quote [77]: "*Therefore, provision should be taken to allow the metrology system of PRIMA to participate to the control of the Differential Delay Lines. This drift can be explained by the fact that one of the beam was propagating very close to the wall of the light duct. Because the wall has a significant temperature inertia, this beam was less affected by the changes of the air temperature compared to the beam propagating at the center of the light duct. . . . It is anyway recommended for pure geometrical reasons; in the current dual feed configuration, the secondary beam is too close from the wall of the light duct.*"

From Eq. (20) one obtains the local angle of arrival at the VCM

$$R \equiv \arctan(y') \approx \frac{n_x G}{n_0} x - \frac{n_x^2 G}{n_0^2} x^2 - \frac{n_x^3 G(G^2 - 6)}{6 n_0^3} x^3 + \cdots, \tag{22}$$

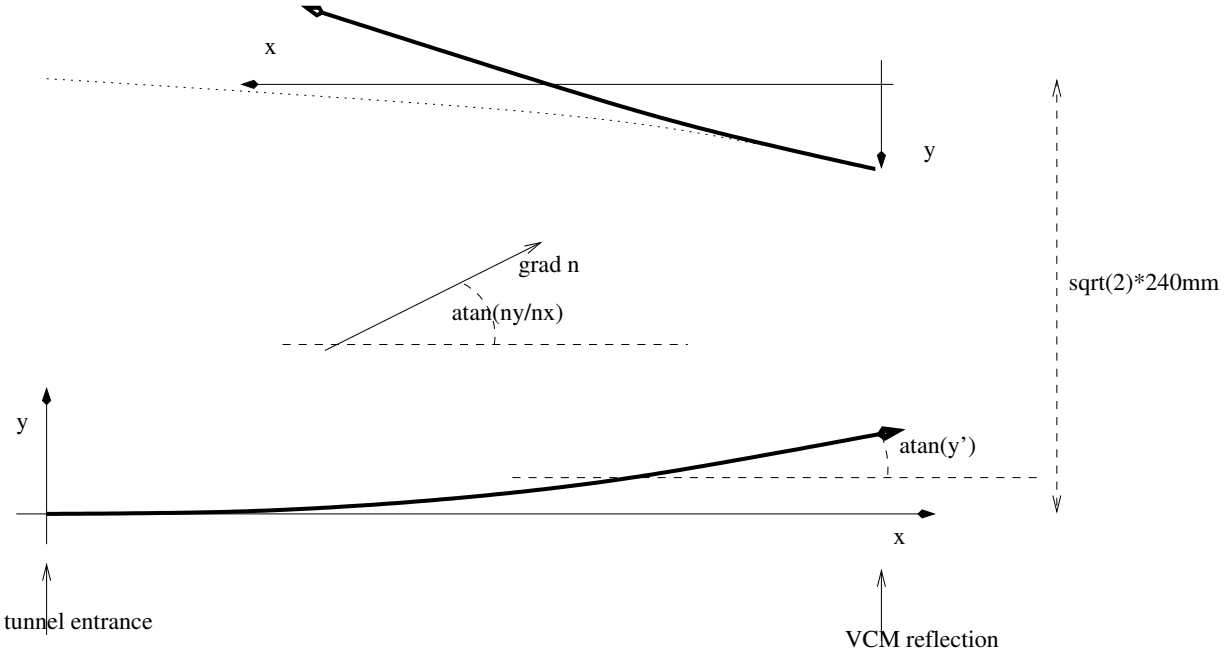

Figure 10: In this calculation of a curved beam, the beam enters the tunnel at $(x, y) = (0, 0)$ and is bent away from the geometric straight line by a horizontal gradient of the refractive index $\nabla n = (n_x, n_y, 0)$.

which is plotted in Fig. 12. Remarks:

1. To obtain the corresponding angles on the sky, these numbers must be multiplied by the ratio $80/1800 \approx 0.044$ of the beam over AT mirror diameters.

2. The angle $\arctan(y/x)$ that is calculated by measuring the beam spot location y on a distant detector [48] and dividing by the detector distance x is only half as large, and this factor has not been taken into account in [48, Table 3] as it seems. (A request on clarification on this factor has been sent to the author in the first week of Feb. 2004, awaiting an answer since then. A look into [77] adds even more confusion by not making a difference between the "tilt" and its standard deviation. It remains dubious if and by which means any of these measurements defined a straight horizontal line of sight. For comparison: the geometric tilt between looking straight along 82 meters through vacuum or looking along the equipotential surface is about 1.3 arcsec given the standard earth radius.)

3. Rewriting Eq. (21) as $y' \approx n_y x$ seems to be compatible with the formula given at the bottom of page 5 in [48], but it remains unclear whether the expression dz/dx there is equivalent to the differential y' or to the divided difference y/x. This "heuristic" approach in [48] seems to introduce the ambiguous factor of $1/2$ that I mention missing above.

The geometric path length would have been x for the straight line and is changed to the integral $\int \sqrt{1 + y'^2} dx$, which is $x[1 + n_y^2 x^2/(6n_0^2) - n_x n_y^2 x^3/(4n_0^3) + \cdots]$. The optical path length would have been $\int n dx = x(n_0 + n_x x/2)$ for the straight line and is the integral $\int n\sqrt{1 + y'^2} dx$ long the curved beam, which is $x[n_0 + n_x x/2 + n_y^2 x^2/(3n_0) - 5n_x n_y^2 x^3/(24n_0^2) + n_x^2 n_y^2 (4G^2 + 9)x^4/(60n_0^3) \cdots]$. The

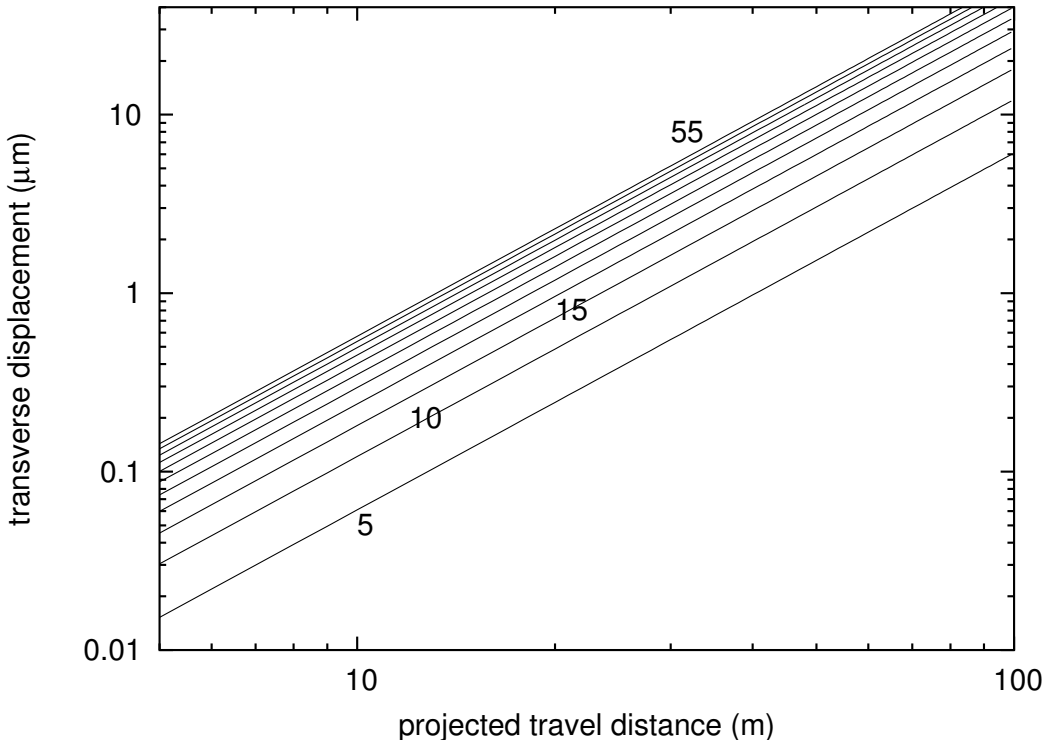

Figure 11: Transverse beam displacement $y(x)$ in μm by a gradient of the refractive index of $1.4\cdot10^{-8}$ m^{-1} for propagation of $x = 5 \ldots 100$ meters along the tunnel and angles $\Psi_0 = 5^\circ \ldots 55^\circ$ between the gradient and the tunnel tube axis, according to Eq. (20).

excess

$$\Delta L = \frac{n_y^2}{3n_0}x^3 - \frac{5n_x n_y^2}{24n_0^2}x^4 + \frac{n_x^2 n_y^2(4G^2+9)}{60n_0^3}x^5 \cdots \tag{23}$$

that one would attribute to the curvature, remains smaller than 0.05 nm for $x \le 100$m and $\Psi_0 \le 55^\circ$ for the examples shown in Figs. 11 and 12. The optical path difference of $\approx n_x x^2/2$ which is added by the longitudinal density gradient has been measured separately [77], but is actually absorbed in the calibration with the metrology as discussed in Sect. 3: if one looks at the OPL calculation just as a numerical integration along the path with varying density, knowledge of the gradient means one can switch from the Riemann type of summation to a trapezoidal rule.

3.3.2 Cascaded Solutions: Mirror Reflections

After the five reflections inside the VCM, the rotational symmetry by the VCM optics [39] is designed to invert this beam displacement on exit, and one would expect at first glance that this could undo some of the transverse effect as the beam would travel on the dotted curve in the upper part of Fig. 10 back to the left. Unfortunately, the consistent model must assume that the same, global density gradient is still effective in these regions (not mirrored), and the beam will therefore be bent asymmetrically, further increasing its angle relative to the geometric horizontal, and crossing the nominal beam axis (solid curve upper part of Fig. 10) depending on how far the delay line carriage is away from M16. After passage through the VCM, the beam is shifted by 240 mm horizontally and vertically relative to the entrance axis; so the further tracing would done in a new (x, y) coordinate

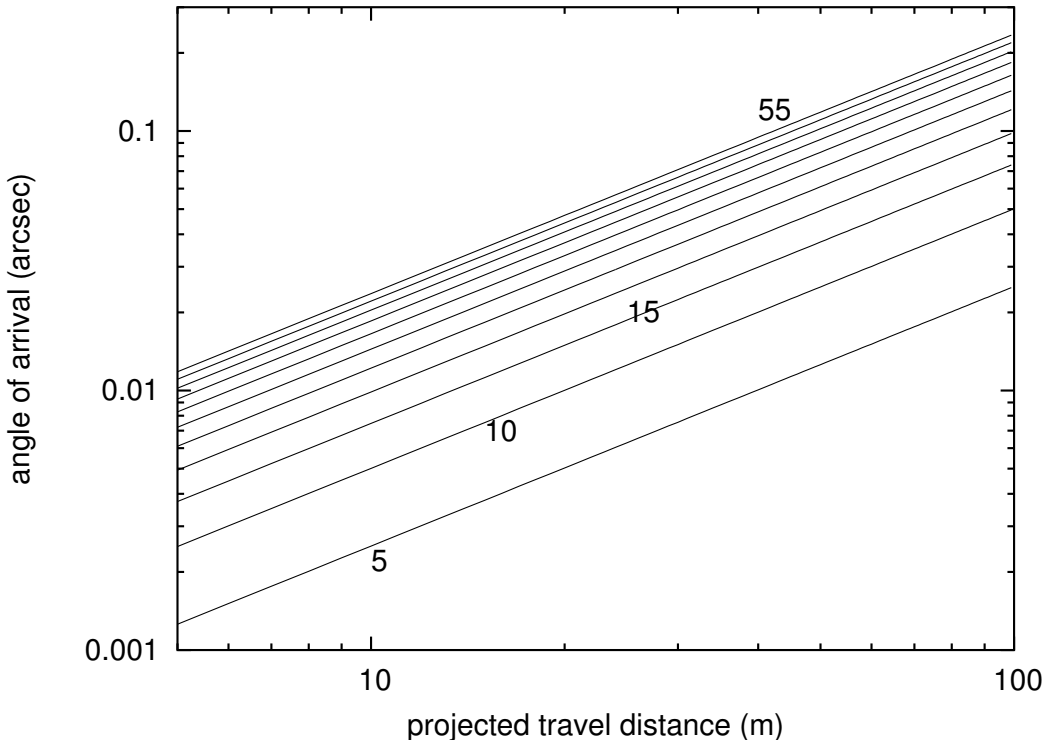

Figure 12: The disorientation R in units of arcsec equivalent to the beam displacement of Fig. 11, according to Eq. (22).

system which is rotated relative to the old one by 180°, in which the boundary conditions are nonzero $y_0 \equiv y(x=0)$, nonzero $y_0' \equiv y'(x=0)$, and the Snell's law

$$n(x,y)\sin\Psi = (n_0 + n_y y_0)\frac{n_y - n_x y_0'}{\sqrt{n_x^2+n_y^2}\sqrt{1+y_0'^2}}. \tag{24}$$

This equation turns into Eq. (18) for a beam with $y_0 = y_0' = 0$. The generalization of Eq. (19) becomes

$$n(G-y') = \frac{(n_0+n_y y_0)(G-y_0')}{\sqrt{1+y_0'^2}}\sqrt{1+y'^2}, \tag{25}$$

and this is solved with

$$y \approx y_0 + y_0' x + \frac{(1+y_0'^2)n_x(G-y_0')}{2(n_0+Gn_x y_0)}x^2 + \frac{(1+y_0'^2)n_x^2(G-y_0')(Gy_0'-3y_0'^2-2)}{6(n_0+Gn_x y_0)^2}x^3 + \cdots \tag{26}$$

$$R = \arctan(y') \approx \arctan(y_0') + \frac{n_x(G-y_0')}{n_0+Gn_x y_0}x - \frac{n_x^2(G-y_0')(Gy_0'+y_0'^2+2)}{2(n_0+Gn_x y_0)^2}x^2 + \cdots \tag{27}$$

This could be used to plot ray paths after return from the VCM as sketched in the upper part of Fig. 10, one explicit example given in Fig. 13. There is one "lucky" point about 40 m away from the VCM at which M16 could be placed and tilted to remove tilt and displacement at the same time (for this particular density gradient). The location of this spot with negligible transverse displacement can be modified with an IRIS tip-tilt [52, 126], but not the tilt of the wavefront at this spot. (This

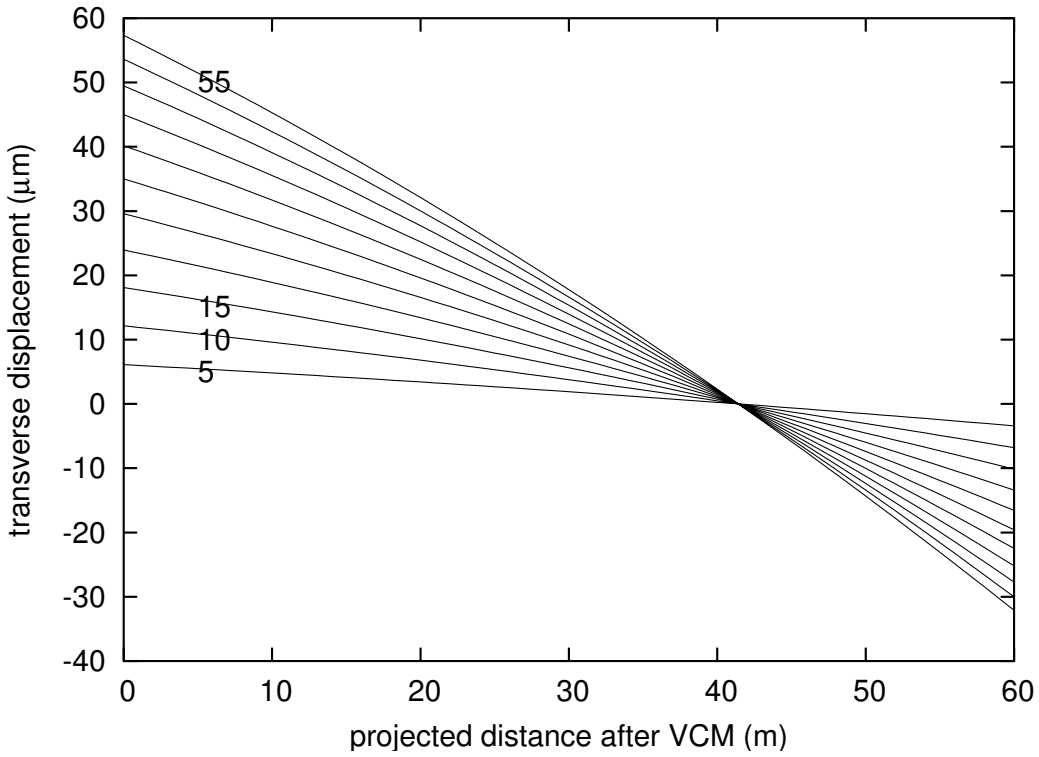

Figure 13: If we assume that the VCM is hit after 100 m in Figs 11 and 12, and follow the path as modeled by Eq. (26) in the same global field of the refractivity in reverse direction, the ray is bent back toward the nominal beam axis, which it meets again after about 40 additional meters—which would be 60 m away from the starting point. This is plotted as before for different angles $\Psi_0 = 5^\circ \ldots 55^\circ$ between the refractivity gradient and the main tunnel axis.

is similar to pointing with a ballistic cannon on a target, where the distance to the target can be adjusted by the barrel inclination, but not the impact angle.)

The effects described above are part of any interferometric instrument of the VLTI and have probably be already documented at places unknown to me: If one writes down the "white light fringe position" in terms of two VLTI metrology readings relative to opposite (fixed) walls of the VLTI tunnel, the difference between these is proportional to the OPD and therefore subject to the scaling by the mean (ie, path integrated) density fluctuations. (This is, of course, the reason why analyses like [109] can correlate temperatures/humidities and OPD's.) The particular aspect of a *gradient* along the beam path is that the standard VLTI operation of keeping one reference DL carriage fixed, and moving the other, faces some "broken symmetry:" moving the carriage at the "cooler" place changes the OPD at the optically thicker place and needs a smaller *mechanical* amplitude to achieve some given OPD. However, the VLTI metrology does not notice this to first order, because its laser beam is scaled by the same effect. This means to the engineer that he cannot measure temperature gradients that way, or to the mathematician that a system of equations with two inputs (optical path lengths) is under-determined to solve for three unknowns (temperature, temperature gradient, and optical path difference). This does not bother standard measurements of fringe amplitudes which acquire the ZOPD wherever it may reside, and if one would attempt to measure the baseline by building the optical path length *sum* at fixed OPD, the effect of the (longitudinal) temperature gradient would cancel as this involves moving one DL carriages up and the other down the gradient. (The optical

path length *sum* is not sensitive to this gradient, whereas the optical path length *difference* is.)

3.3.3 PRIMA Related Aspects

The metrology light is forced into the same analysis. With IRIS in operation, a gradient of the refractive index would be corrected by tilting a mirror of the STS, which leaves a small difference in angles and OPD between the science and the metrology wavelength. The principle of operation is shown in the sketches of Fig. 14. With Eq. (21) and Fig. 1, each °C/m of lateral gradient in the

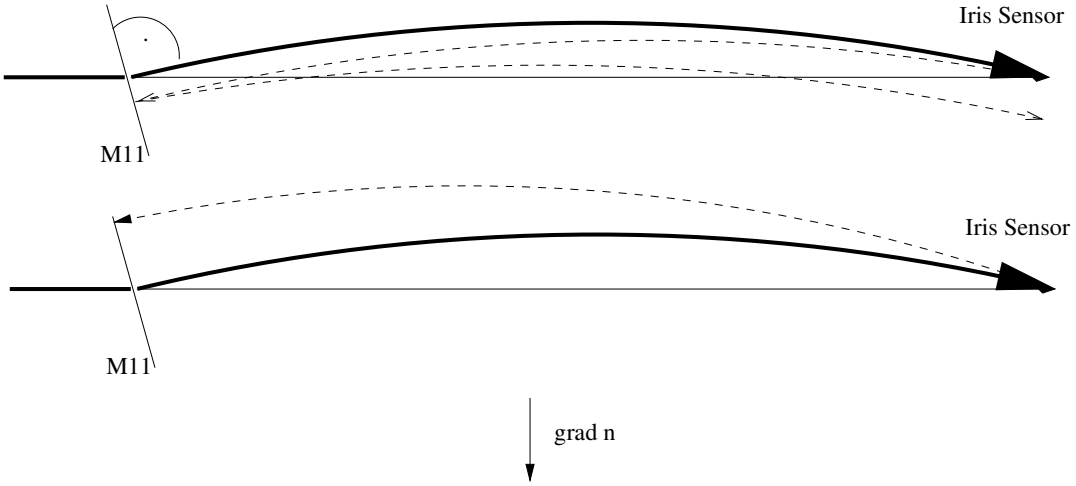

Figure 14: By tilting M11 in the STS, IRIS keeps the star beam (bold line) on the axis at arrival at its sensor reacting to a gradient of the index of refraction n. Beams would run straight horizontal (thin horizontal line) if there were no refractive index gradient. The metrology beam (dashed curves) experiences a slightly different gradient, caused by the chromaticity in the air dispersion (the term $\partial^2 n/(\partial\lambda\partial T)$). Top: If it is launched close to the IRIS sensor location at the same angle as the science beam, it hits M11 at a slightly different angle, and is not reflected back to its point of departure. Bottom: If one aligns the metrology beam also to return to its original point, it has to be "launched" under a different angle and hits at a different M11 segment than the science beam to compensate for the fact that the M11 tilt is not optimized to its wavelength.

temperature means a lateral spread of $5 \cdot 10^{-7}/\mathrm{m} \times 1/273 x^2/2 \approx 7.5 \cdot 10^{-10} x^2/\mathrm{m}$, and after $x = 100\mathrm{m}$ the science beam and metrology are separated by several μm. With Eq. (22) one could say that each °C/m of lateral gradient in the temperature creates a differential angle of $5 \cdot 10^{-7}/\mathrm{m} \times 1/273 x \approx 15 \cdot 10^{-10} x\mathrm{rad/m}$ between the two wavelengths, which is 31 mas in the lab (1.4 mas on the sky) after $x = 100\mathrm{m}$. As shown in Tab. 9, independent alignment of the metrology beam on its different trajectory gives a beam offset on the IRIS tilt mirror which is proportional to the square of the distance from the mirror to the lab. (The table has been created by selecting a mirror tilt that ensures that the science beam is back to the axis after the distance x, then searching for a self-consistent y_0' for the metrology beam that forces it to land perpendicular on this tilted mirror to have its return path matching the forward path.)

Further remarks:

1. The time-independent part of this misalignment will probably be canceled by rotation of the PRIMA feeding mirrors in the interferometric laboratory [52]. Due to the seasonal sign flip

x (m)	R sci (rad)	R met (rad)	displac (μm)
10	$3.7428 \cdot 10^{-6}$	$3.7611 \cdot 10^{-6}$	0.092
100	$3.7428 \cdot 10^{-5}$	$3.7611 \cdot 10^{-5}$	9.154
150	$5.6142 \cdot 10^{-5}$	$5.6417 \cdot 10^{-5}$	20.596

Table 9: The distance x between the mirror and the "launch" point, the two angles of the science and the metrology beam at the launch point, and the lateral displacement between the two beams at the mirror position for the lower picture in Fig. 14 for each °C/m of lateral gradient in the temperature.

of the vertical temperature gradient in the interferometric laboratory [79, p 13], this is only a semi-permanent adjustment. Obviously, the Coudé guider does not see these effects, and cannot be used for online-corrections, but calibration of the misalignment could be done with any other K band instrument (VINCI TCCD) long before PRIMA operations start to obtain a pointing offset table as a function of tunnel temperature gradients.

2. The beam curvature in the delay line tunnel is caused by transverse temperature gradients; the placement of the temperature sensors [80] is strongly biased toward measuring the longitudinal gradient, and doing this only in the delay line tunnel (not in the ducts) [2].

3. The beam of the associated interferometric second beam on another delay line experiences the same effect, but with the negative of this gradient in its coordinate system, because it runs into the opposite direction.

In summary, beam curvature following from air density gradients in the tunnel are first of all a problem of beam wandering on the detector, a problem of alignment in the static case, and a problem of loosing coherency depending on the frequency range. The impact of the additional optical path length following from the beam bending seems to be negligible.

3.3.4 Beam Tilt in the Tunnel

A further effect of the established vertical temperature gradient in the DL tunnel of the order of 0.1 K/m [79] is a tilt of the upper part of a beam relative to the lower part: at this part of their way, before the BCs, the beams have diameters of 80 mm, which means the upper and lower rim face temperature differences of $8 \cdot 10^{-3}$ K. At 2 μm, each degree difference in temperature (at constant relative humidity and pressure) leads to a change of air refractivity of $\approx 8 \cdot 10^{-7}$—that is $(n-1)/280$ at $T = 280$ K. Therefore the two opposite rims of the 80 mm beam see a difference in refractivity of $64 \cdot 10^{-10}$, which would accumulate over a typical path length of 100 m to 640 nm differential OPD within each beam (Fig. 15). This is a wavefront tilt, up or down depending on the season, of $8 \cdot 10^{-6}$ rad or 1.7 arcsec in the lab (equivalent to 37 arcsec on the sky). The effect is partially canceled by symmetry,

- since one of the interferometric beams moves westwards and the companion eastwards in the tunnel starting from their M12, which means the upper and lower pieces of these wavefronts will be paired interferometrically, non-crossing,

- since the reflection by the VLTI DL (M13–M15) inverts the beams: effectively only the paths from M12 to M16 ($U \approx 53$ m) add up. (The upper rim on entry to the DL becomes the lower rim on exit, but the temperature gradient does not flip its sign between these two levels in the

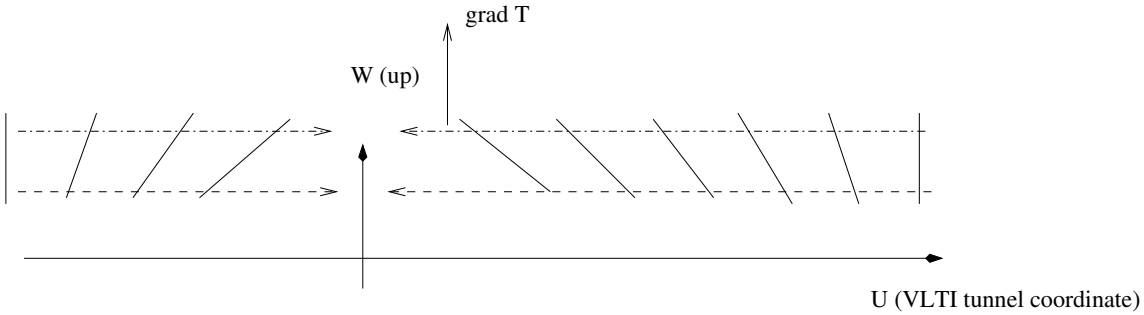

Figure 15: The effect of a vertical temperature gradient (associated with Paranal's W coordinate) is a reduced density of air in the warmer section of each 80 mm beam, effectively a smaller refractive index and accumulation of a wavefront tilt as the beam moves along the U coordinate. Tilts for beams moving in opposite directions cancel to the degree that these paths have the same length, as one collapses/superimposes the pieces across the planes to build an interferometric pattern in the BC.

laboratory. So the portion of the beam that experienced the colder air when approaching the carriage, experiences the warmer air when returning.)

Incomplete cancellation happens if the telescope stations have asymmetric distances to the $U \approx 53$ m coordinate; the worst case pairs a telescope on the A-rail ($U \approx -32$m) with a telescope on the H-rail ($U \approx 64$ m), which leaves a non-matching path length of $(|-32-53|-|64-53|)\text{m} \approx 74$ m. The effect is chromatic and mimics very much a transverse atmospheric dispersion, with the major difference that the direction is not determined by the beam orientation on the sky but by the orientation in the tunnel.

Numerical evaluation of the fiber coupling coefficients for black body star spectra multiplied by the detector quantum efficiency has been done as follows: the vertical temperature gradient is converted to a Z_2 Zernike polynomial across the pupil, interpreted as a phase over the pupil, and numerically integrated with the fiber's far field to define a chromatic amplitude coupling coefficient. The square of this (the energy coupling) is multiplied with the spectrum, which shifts the effective (mean) wavenumber as listed in Table 10. The effect is proportional to the square of the intra-pupil phase shift, which itself is proportional to the asymmetry in the path length ΔU and proportional to the temperature gradient.

$\Delta U = 75$ m			$\Delta U = 30$ m		
$\partial T/\partial r$ (K/m)	T (K)	$\Delta\bar{\tilde{\nu}}$ (cm^{-1})	$\partial T/\partial r$ (K/m)	T (K)	$\Delta\bar{\tilde{\nu}}$ (cm^{-1})
0.05	3000	0.26	0.05	3000	0.04
0.1	3000	1.04	0.1	3000	0.17
0.1	4000	1.04	0.1	4000	0.17
0.1	6000	1.04	0.1	6000	0.17
0.1	8000	1.04	0.1	8000	0.17
0.1	16000	1.04	0.1	16000	0.17

Table 10: Change of the effective wavenumber $\bar{\tilde{\nu}} = \int e(\tilde{\nu})\tilde{\nu}\, d\tilde{\nu} / \int e(\tilde{\nu})\, d\tilde{\nu}$ if a vertical temperature gradient $\partial T/\partial r$ is switched on, computed for the central of the three spectral channels at two different lengths of the East-West difference of the distances between M12 and M16.

Although the effect on the change of the effective wavenumber ought not be larger than 0.4 cm^{-1} [162] to define the star spectrum well enough for the dispersion correction, the prospective violation of this constraint in Tab. 10 cancels to very high degree: the shift for both beams is the same because there is virtually no star temperature dependence. To the approximation that the second derivative of the refractivity $\partial^2 n/\partial\tilde{\nu}^2$ can be neglected, the differential effect in the color correction disappears.

4 FSU K-PRISM DISPERSION

4.1 Differential OPD

The task of the PRIMA K-prism is to introduce a $\lambda/4$ shift of one beam relative to the other at a nominal wavelength of 2.25 μm [13]. The estimated dispersion of the Infrasil glass (by Heraeus) is plotted in Fig. 16. The path of the 1.3 μm metrology laser leads also through the beam combiner and this "achromatic" phase shifter, and therefore the graph shows the J, H, and K band.

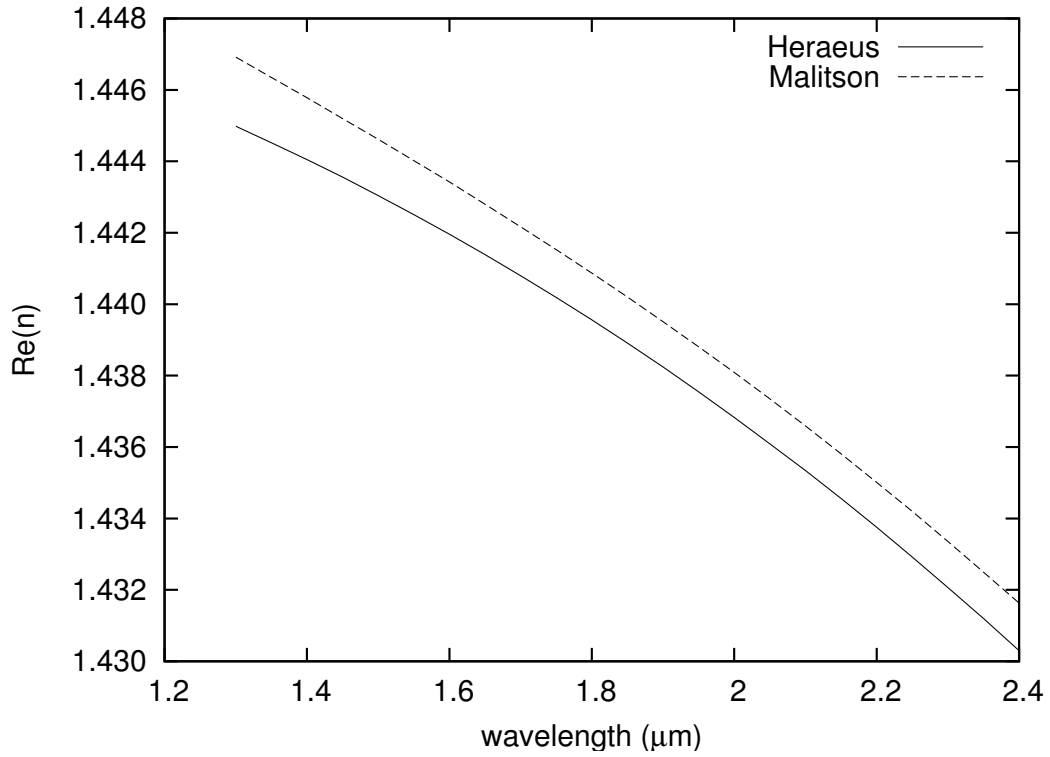

Figure 16: The refractive index of fused silica from the June 2003 data sheet (3-term Sellmeier formula) of the manufacturer in comparison to the Malitson formula [7, 92]. The dispersion between 2 and 2.4 μm is 0.00646.

At an internal path length of 152.12 mm within the glass, the dispersion of 0.006 between 2 and 2.4 μm amounts to a difference in OPD within the K band window of about 151.12 mm ·0.00646 ≈ 0.98 mm, which is equivalent to about 40 times the OPD difference introduced by the air dispersion after 200 m of air. The change of this index of refraction is estimated at $\partial n/\partial T \approx 10.9 \cdot 10^{-6} 1/K$ [158, 175]. A typical seasonal change of the temperature by 0.5° C close to the PRIMA table (where no temperature sensor is foreseen) would therefore change the OPL in both beams by about 0.8μm.

The additional dispersive path lengths and its temperature drift are supposed to cancel as these OPLs subtract to build the OPD (but see [61]). The problem of extrapolating the OPD as seen by the metrology light to the K band re-surfaces as already discussed for the air dispersion in Sec. 3. There is only an error contribution to the differential OPD if the 4 pieces (K-prisms and compensation blocks in both FSUs) have different lengths after finishing the manufacturing process. Example: If one of these is 1 μm shorter than the other three, the metrology laser measures an (additional) OPD of 1 μm ·1.44692 for this star, which is (in the K band) only an (additional) OPD of 1 μm ·1.4342. This

correction of $\approx 1\ \mu$m $\cdot 0.013 \approx 13$ nm would have to be calibrated once and for all—the additional temperature drift becoming negligible then.

4.2 Phase Shifts for Total Internal Reflections

The phase jump for TIR differs between the s and p component of the electric field vector; it is calculated via [6, 15]

$$\tan\frac{\delta_\perp}{2} = -\frac{\sqrt{\sin^2\theta - \hat{n}^2}}{\cos\theta} \tag{28}$$

$$\tan\frac{\delta_\parallel}{2} = -\frac{\sqrt{\sin^2\theta - \hat{n}^2}}{\hat{n}^2\cos\theta} \tag{29}$$

$$\tan\frac{\delta}{2} = \frac{\cos\theta\sqrt{\sin^2\theta - \hat{n}^2}}{\sin^2\theta}, \quad \delta \equiv \delta_\perp - \delta_\parallel \tag{30}$$

from the effective index of refraction $\hat{n} \equiv 1/n$ for various angles of incidence θ from the dispersion. Examples of δ as a function of θ are shown in Fig. 17.

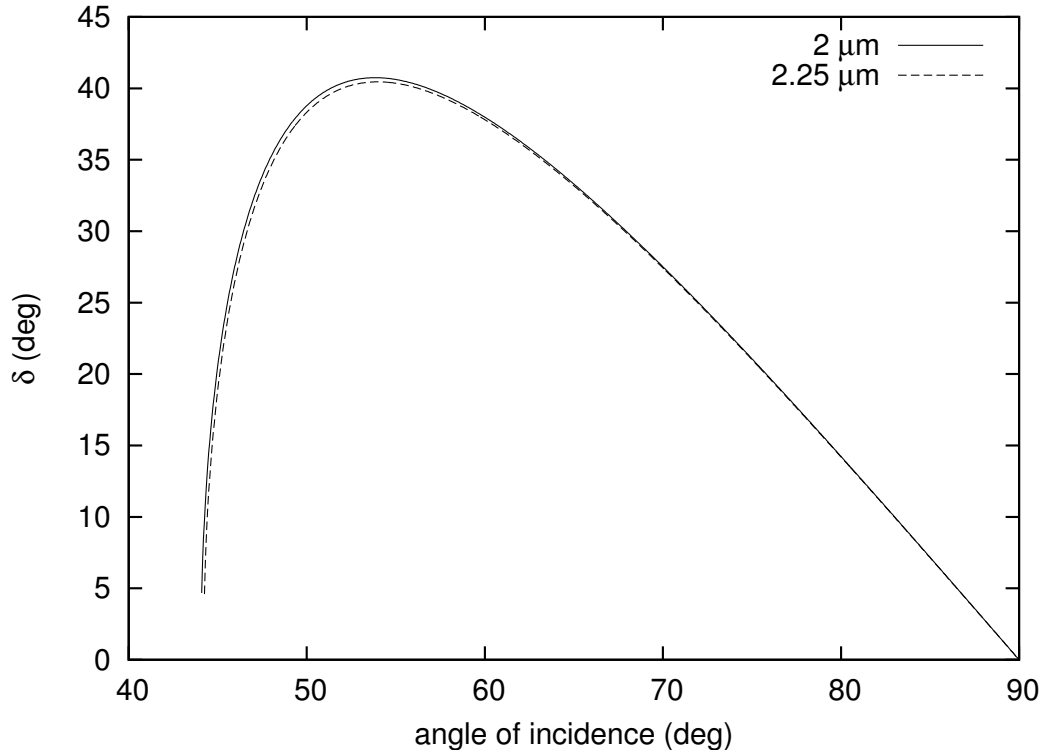

Figure 17: The difference δ between the phases for the s and p components of the electrical field vector after TIR within the material of Fig. 16 for two K band wavelengths λ and varying angle of incidence θ. See [13, Fig 4.3-3] for comparison.

The design [13, Tab. 4.3-1] foresees two internal reflections at $\theta_1 = 72.12°$ at the legs of the prism and one at $\theta_2 = 2\theta_1 - 90°$ off the base. This results in a total phase difference between the s and p component of $2\delta(\theta_1) + \delta(\theta_2)$ which is shown in Fig. 18. The K-prism angles have been chosen to achieve a sum of 90° at $\lambda = 2.25\ \mu$m. The mismatch $\Delta\delta \equiv \sum\delta - \pi/2$ from these 90° is below

$|\Delta\delta| \leq 0.4° \approx 0.007$ rad ≈ 0.001 cycles, equivalent to an OPD shift of less than 2.4 nm. This is to be compared with a value of 10 ° measured for a metrology laser round trip [83, p. 13] and characterizing the polarization by the VLTI optical train.

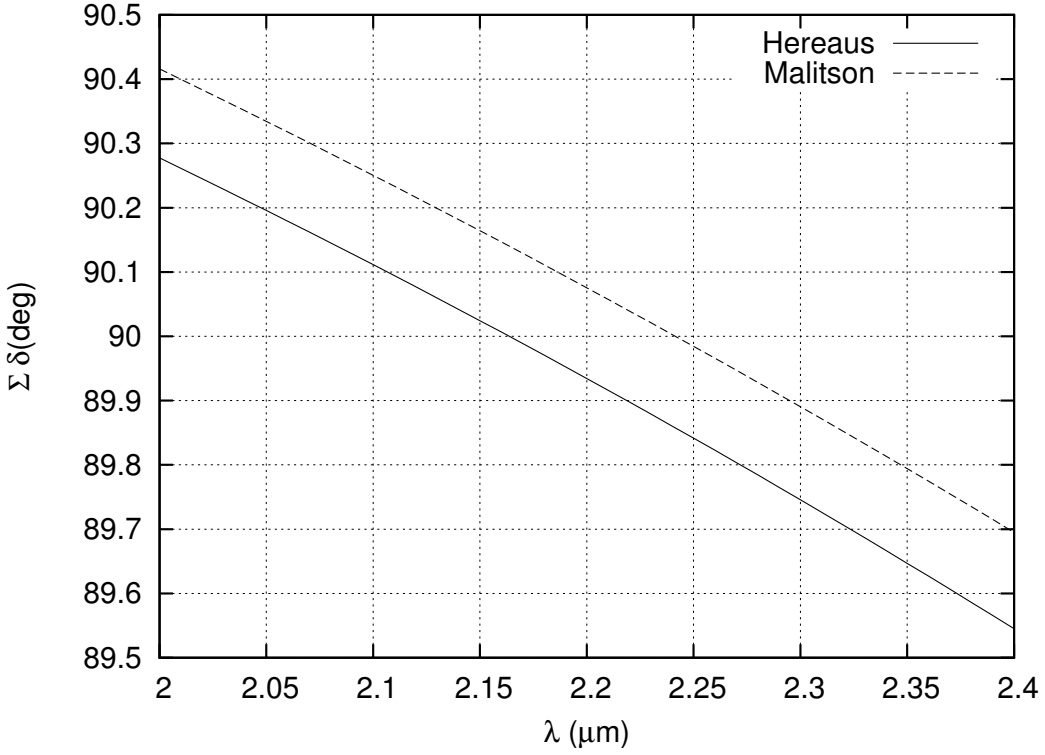

Figure 18: The accumulated phase difference between the components of the electrical field vector perpendicular and parallel to the K-prism base, modulo 360°, after three TIRs within the Infrasil material characterized in Fig. 16 as a function of wavelength λ at the nominal angles $\theta_1 = 72.12°$ and $\theta_2 = 54.24°$.

An obvious side effect is that the output state of a light ray that is linearly polarized on entrance to the K-prism stays linearly polarized on exit only if the electrical field vector is parallel (azimuth $\alpha = 0$) or perpendicular ($\alpha = 90°$) to the base. If it started rotated by $\alpha = 45°$ on entry it becomes circularly polarized on exit, in all other cases elliptically polarized: Fig. 19.

4.3 With the ABCD algorithm

Note that the accumulated phase kinks $\sum \delta_\perp$ and $\sum \delta_\parallel$ are not individually 0 or 90° after the total reflections, only the difference $\sum \delta$ is. These are actually visualized in Fig. 19 by the fact that the period of neither the horizontal nor the vertical, degenerate, ie linearly polarized, beam start at $E_X = +1$ or $E_Z = +1$, respectively. Two linearly polarized beams that enter the K-prism and the compensator at common E-vector angles $\alpha = 0$ or 90° towards the $+X$ axis maintain their plane of polarization (and remain "eligible" for coherent superposition from this point of view). The two components through the beam compensator (telescope 2) would read $S_2 \cos(0)$ and $P_2 \cos(0)$ on exit, the two components through the K-prism (telescope 1) $S_1 \cos(\sum \delta_\perp)$ and $P_1 \cos(\sum \delta_\parallel) = P_1 \cos(\sum \delta_\perp - \pi/2 + \Delta\delta) = P_1 \sin(\sum \delta_\perp + \Delta\delta)$. Supposed the beam combiner is ideal, it mixes these into sums and differences that are separated in s and p by the beam splitters, and with the same fluxes

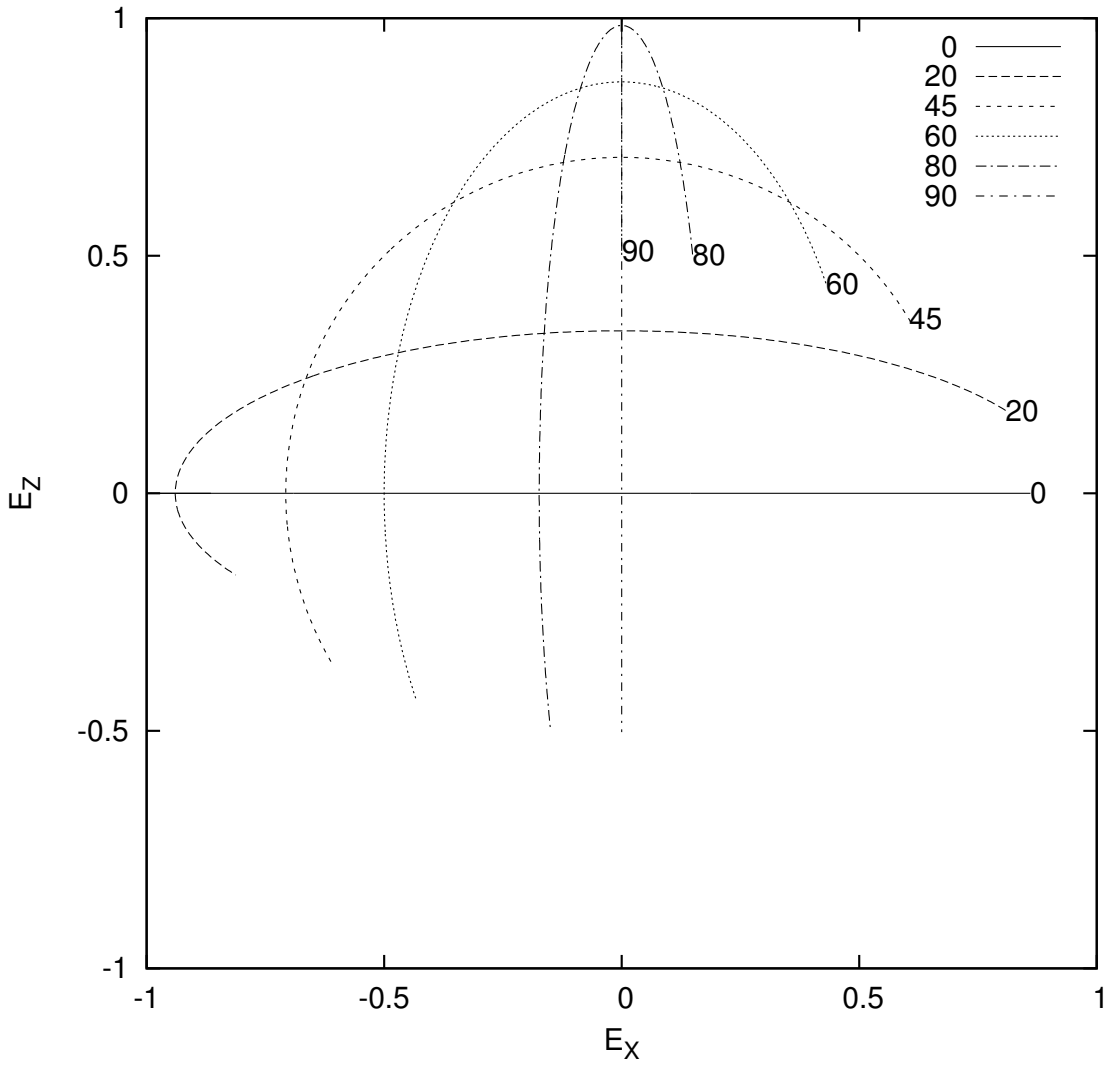

Figure 19: Half periods of the electrical field vector, as the ray leaves the K-prism into the $+Y$ direction, for different angles of rotation α between 0 and 90° it had towards the $+X$ direction when approaching the first internal reflection as a linearly polarized beam. The curves start at $E_X = \cos(\sum \delta_\perp)$, $E_Z = \cos(\sum \delta_\parallel)$, where the sums are taken over all three internal reflections. This assumes $\lambda = 2.25$ μm and the nominal incidence angles.

in the s and p-components ($S_1 = S_2 = P_1 = P_2$) we may drop the constant prefactor everywhere and define the four amplitudes just in the counter-clockwise order $1 + \cos(\sum \delta_\perp)$, $1 + \sin(\sum \delta_\perp + \Delta\delta)$, $1 - \cos(\sum \delta_\perp)$, $1 - \sin(\sum \delta_\perp + \Delta\delta)$. Building the individual squares A, B, C and D (detector readouts) of these and then the standard phase estimator yields the following series in terms of the $\Delta\delta$:

$$\arctan \frac{B-D}{A-C} \approx \sum \delta_\perp + \Delta\delta \cos^2(\sum \delta_\perp) - (\Delta\delta)^2 \sin(\sum \delta_\perp) \cos(\sum \delta_\perp)[\cos^2(\sum \delta_\perp) + \frac{1}{2}] + \cdots \quad (31)$$

The $\sum \delta_\perp$ as well as the $\Delta\delta$ are wavelength-dependent, and $|\Delta\delta| < 0.5°$ according to Fig. 18, and so it makes sense to plot the sum of the first two terms of this expansion to visualize the contribution of the K-prism to the output of the ABCD algorithm: Fig. 20.

This becomes more complicated if either the sky source itself is polarized or the VLTI optical train

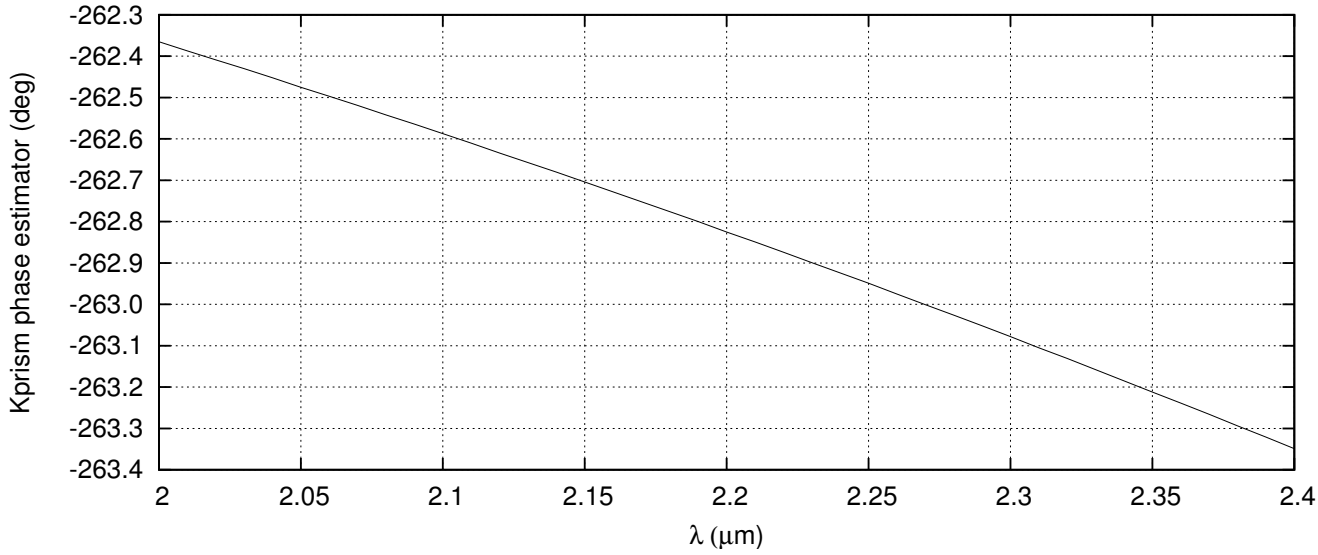

Figure 20: The ABCD phase estimator error due to the internal dispersion of the K-prism, expressed as the first two (constant + linear in $\Delta\delta$) terms of Eq. (31) for the Heraeus-dispersion of Fig. 16.

acts like a polarizer.

5 POINTING ON THE SKY

5.1 Basics: True and Apparent Zenith Angles

The pointing difference between the apparent and actual altitude of a star that is induced by the refraction of the earth atmosphere is in a simple model of a flat earth [57, (4.4)][42]

$$R \approx (n_0 - 1) \tan z_0, \tag{32}$$

where n_0 is the index of refraction on the ground, z_0 the zenith distance on the ground, and

$$R = z - z_0 \tag{33}$$

given in radian. We get Fig. 21 for a typical index of refraction.

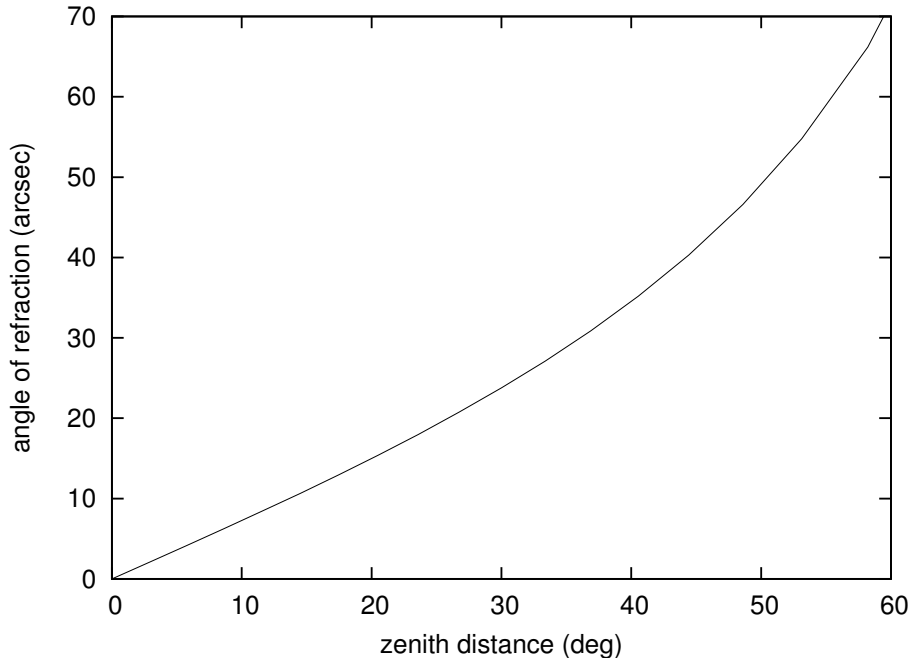

Figure 21: The angle of refraction R as a function of the zenith angle z_0, Eq. (32), for a horizontally flat model atmosphere and a refractive index on the ground of $n_0 - 1 = 2 \cdot 10^{-4}$. The AT operations are limited to zenith angles of 60 degrees.

We are interested in the chromatic effects [86, 93] and the dependence on the atmospheric model. This effect is also called transverse atmospheric dispersion in Astronomy.

From Eq. (32) we immediately deduce that the relative error in the altitude definition is very close to the relative error in the susceptibility at the telescope altitude above sea level. We can multiply (32) with $P = b \cos z_0$, where b is the baseline length, P the length of the projected baseline, and $D = b \sin z_0$ the delay line, and are back to numbers of the error estimate made in Sec. 3.1. This results means in essence that the Snell's law of refraction through the atmosphere states that $n \sin z$ remains constant along the path [57, (4.2)], and since we are measuring an optical path difference on the ground that is proportional to this product, we may (ambiguously) assign this difference either to a $\Delta(\sin z) = \cos z \Delta z$ at $n = 1$ above the atmosphere, or to $\sin z \Delta n_0$ at ground level, or to a weighed

sum of both. The benefit is that the pointing correction is a function of the local index of refraction, not a functional of the entire layered atmosphere.

The main conclusion (within this simple model of the atmosphere that can reduce the air density strictly to its density at the ground) from this argumentation is that there is no "double counting" of the error introduced by an unknown index of refraction; one may either look at as if induced "in the delay line tunnel" or as if introduced through an unknown curvature through the air, but there is no need to add/accumulate these errors.

Obviously, there is a rainbow effect in Eq. (32): as n_0 is a function of the wavelength λ, R becomes a function of λ, too: For wavelengths of $\lambda_1 = 2$ μm and $\lambda_2 = 2.4$ μm, we get a difference of $\Delta n_0 \approx 1.05 \cdot 10^{-7}$ from the solid line of Fig. 1, which translates into a spectral smear of $\Delta R \approx 22$ mas $\cdot \tan z_0$. Typical examples follow in Fig. 22. (22 mas are also the Airy disk radius at a 25 m baseline at 2.2 μm.)

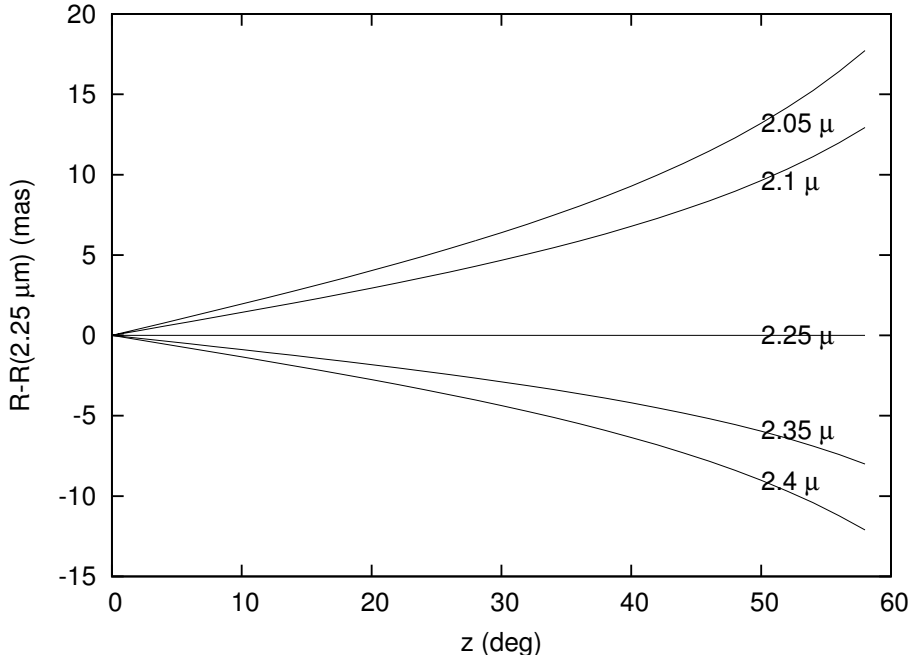

Figure 22: Transverse atmospheric dispersion at five wavelengths relative to some center wavelength 2.25 μm as a function of zenith angle, assuming $n - 1 = 2.03989087352 \cdot 10^{-4}$ at 2.05μm, $2.03974594703 \cdot 10^{-4}$ at 2.1μm, $2.0393540321 \cdot 10^{-4}$ at 2.25μm, $2.03911154344 \cdot 10^{-4}$ at 2.35μm, and $2.038987167 \cdot 10^{-4}$ at 2.4μm, in (32).

5.2 Spherical Earth: Geometry

Things are more complicated if we start to look at the more realistic model of a spherical earth [99, 102][17, 18, §2.3]. A telescope distance of $b = 100$ m on an earth of radius 6370 km leads to a purely geometrical pointing mismatch of about $b/\rho \approx 1.6 \cdot 10^{-5}$ rad $\approx 9 \cdot 10^{-4}$ deg ≈ 3.2 arcsec (Fig. 23). Note

- that this term b/ρ implies an approximation of the kind $\sin Z/2 \approx Z/2$, a limit of a baseline so short that it does not matter whether it is measured along a straight line (as drawn in Fig. 23)

or along the circular perimeter. The relative error (from the Taylor expansion $\sin Z \approx Z - Z^3/6$) in this formula is about $Z^2/26$, or about 10^{-11} for the example of $b = 100$ m.

- that this also seems to require some minimum precision on the knowledge of the telescope distances ρ from the earth center. This is only a virtual requirement, because the baseline b is coupled to it—the zenith angles and the angle Z do actually not change as we displace the telescopes vertically. On the other hand, we are supposing that n_0 (the air "thickness") is a function of the telescope altitude, which introduces higher order corrections.
- Pointing/guiding is a functionality of the individual ATs: the existence of a nonzero pointing difference is absorbed in the telescope operation, and any delay originating from there is to first order absorbed into the tracking of the PS from the PRIMA "differential" point of view, including TAD correction [13]. We hereby explicitly deny any first-order relevance to the "separation" term of Gubler and Tytler eminent from their consideration of single telescopes [58], because both our telescopes are "mispointing" at the same time with respect to the SS, and the delays of interest compare the PS zenith angles and the SS zenith angles separately. (The full truth is that guiding, at least for the UTs if we believe in the MIDI FITS header keywords, is done at $\lambda = 600$ nm, not anywhere in the IR. It remains to be investigated whether any residual effect accrues from there or from the fact that the VLT guiding software has its own algorithms of wavelength-dependent pointing correction [174, §14.9].)

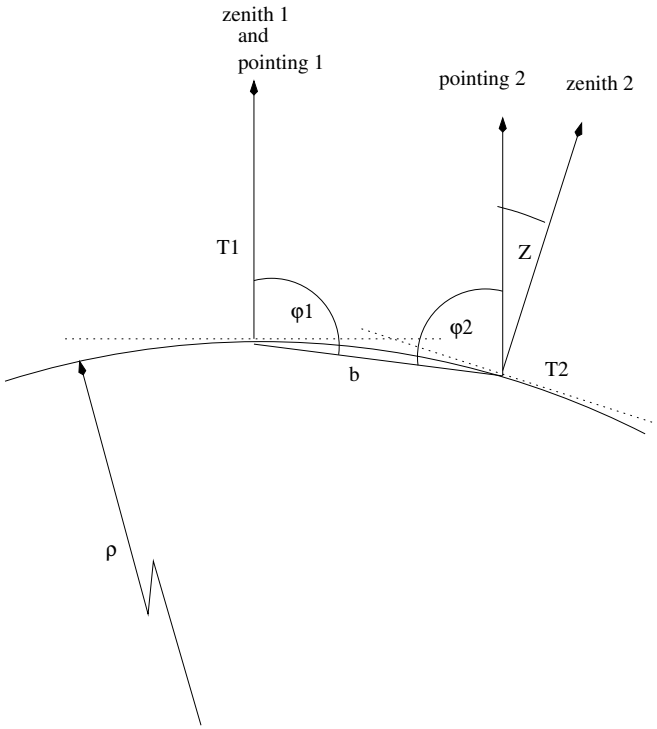

Figure 23: Two telescopes placed on the earth of radius ρ at a distance b looking at the same star experience local zenith angles that differ by $Z \approx b/\rho$, measured in rad, supposed $b \ll \rho$.

These data inserted back on the abscissa axis of Fig. 21 indirectly transform into a contribution to the delay that may be understood (and calculated to lowest order) on the basis of what is said in Sec. 5.1 but has no equivalent with single telescopes (as long as their diameters are much smaller than the earth radius). The example of $9 \cdot 10^{-4}$ deg from the previous paragraph translates into an additional

angle of refraction of $\Delta R \approx \Delta z_0(1+\tan^2 z_0)(n_0-1) > \Delta z_0(n_0-1) = Z(n_0-1) \approx 1.8\cdot 10^{-7}$ deg ≈ 650 μas and is certainly relevant from the PRIMA perspective. (The equation is the first derivative of (32) w.r.t. z_0. The neglect of the term $\tan^2 z_0$ means this is a lower estimate in the limit of stars at the zenith.)

The effect on the delay described here could also be interpreted in the "standard model of delay line correction," where the two rays of the star that will eventually hit the two telescopes "generate" a phase difference in the vacuum (undone later on in the delay line tunnel) because they hit the top layer of the earth atmosphere with a path difference of

$$D = b\sin z = P\tan z \tag{34}$$

(Fig. 7). The curvature correction means that this top layer "bends back" a bit for the telescope further away from the star. Note that dependable discussion of what the mathematical symbols mean seems to be missing in the "astrometric literature." The only obvious definition of the baseline length b is on earth. In a formal way, one may actually define an effective baseline length b^* above the atmosphere via

$$b^* \equiv \sqrt{P^2+D^2} \tag{35}$$

which turns out to be larger than b because the earth's atmosphere acts like a concave lens. This effective baseline is a function of the baseline b, and the star zenith angle, and a functional of the atmospheric refraction $\chi(r)$.

5.3 Spherical Earth: Atmospheric Layers

The delay line modification described in the previous paragraph is of purely geometrical nature and is closely related to the discussion of differences between two light rays, but there are more pointing "corrections" that already show up in the single ray case, as discussed next.

Eq. (32) is based on the assumption that the gradient of the refractive index n along the ray path is parallel to a global, constant zenith vector. As the gradient and the zenith vector change in direction along the path through a spherically symmetric atmosphere, because we assume that n becomes a function of the radial distance to the spherical surface of the earth, the equation becomes more accurately [57, (4.19)][5, 135, 160]

$$R = r_0 n_0 \sin z_0 \int_1^{n_0} \frac{dn}{n(r^2n^2 - r_0^2 n_0^2 \sin^2 z_0)^{1/2}}, \tag{36}$$

an integral over the refractive index, with limits to start above the atmosphere ($n=1$) and to end at the telescope position ($n=n_0$). The major new aspect is that the pointing direction becomes a functional of the height spectrum of the index n.

We first consider simple atmospheric models with a homogeneous composition of the molecule species such that the susceptibility

$$\chi = \epsilon - 1 = n^2 - 1 \tag{37}$$

falls off exponentially into the free space vacuum with a scale height K,

$$\chi(r) = \chi_0 e^{-(r-r_0)/K}, \tag{38}$$

where χ_0 is the value at the telescope (ground) level. A thorough examination shows that the curvature effect mentioned on page 52 actually may reduce R by up to 0.5% [99, Fig. 4], which

amounts to effects of 350 mas if combined with Fig. 21 close to $z = 60°$. The related Taylor expansion of (36) for small heights $h = r - r_0$ above ground starts as [99, (13)][57, (4.25)]

$$R = n_0 \sin z_0 \int_1^{n_0} \frac{dn}{n(n^2 - n_0^2 \sin^2 z_0)^{1/2}} - \frac{n_0 \sin z_0}{r_0} \int_1^{n_0} \frac{hn\, dn}{(n^2 - n_0^2 \sin^2 z_0)^{3/2}} + O\left((h/r_0)^2\right). \quad (39)$$

If the Earth model is detailed as a prolate ellipsoid with two axes that differ by a relative amount of 1/298 [161], the definition of ρ becomes fuzzy on this scale; in consequence, the inherent accuracy of R within the spherical model of the atmospheric hull around the earth is not better than ≈ 1 mas for $z \approx 60°$, and this is also the expected azimuth-dependence in the K band on Paranal. In summary, the effect of Earth ellipticity on R is less than 1/300 of 0.5% and therefore (i) covered by the daily variance in the surface pressure $\sim (n_0 - 1)$, which is $\approx 1/500$, see the plots in http://www.strw.leidenuniv.nl/~mathar/vlti/, and (ii) also much smaller than the resolution $1.2\lambda/d \approx 0.31''$ established by the single-telescope PSF.

The validity of this exponential model is related to the exponential scaling of the most important atmospheric gases as a function of altitude (Figs. 24 and 25). At our light frequencies of $1.3 \cdot 10^{14}$ Hz, the susceptibility of the Ionosphere is not expected to be larger than $1 \cdot 10^{-9}$ [62, (1.5)] and not to create a noticable bump.

The examples of Fig. 26 show that the misassignment in the star position could be a few mas for each kilometer of error in the scale height, increasing with the air mass. In the limit of $K \to 0$, we recover the values for the flat earth of Eq. (32); this is intuitively reasonable because it means that the air layer becomes thinner and thinner compared to the earth radius, and the "final" piece of the ray path, which observes the earth more and more as a flat disk, gets more and more statistical weight in the determination of the final, full angle of refraction. The corresponding mathematical argumentation is given by [157, (4)] and the limit $H^* \to 0$ in [86, (1)]. In practice, the scale height is coupled to the atmospheric gas density via Eq. (12), and in a self-consistent model of a single average molecule species like Eq. (38), K is uniquely coupled to the atmospheric pressure at ground level [108].

A variant of this problem is established if the scale heights of various gas components differ or the mixing ratios change [140, 152, 166]. In this case Eq. (38) is to be replaced by a sum over gas components with individual χ_0 and K. (It is certainly doubtful to scale the entire, single scale height with the ground humidity instead [86].) For illustration let us assume a fixed a "dry air" contribution to $\chi(r)$ with a scale height of 10 km at $\chi_0 = 4.0808 \cdot 10^{-4}$, superimposed by water vapor at $\chi_0 = 1.75 \cdot 10^{-6}$ that "freezes out" faster at varying scale heights of only a few kilometers [170]. (The sum of the two χ_0 corresponds to the point at 2.2 μm on the solid curve of Fig. 1.) Fig. 27 shows that this results in pointing variations of the order of tens of μas. Calibration of this water column by monitoring parts of the spectrum with high atmospheric water absorption was proposed before [1, 109, 122, 141, 144]; from the astrometric point of view, PRIMA would need a Fourier mode to do this on its own, but also seems not to depend on it as the differential pointing largely cancels (see below).

Another result from the ray tracing analysis is that the small difference in the refractive indexes at 2 and 2.4 μm, about $\Delta\chi_0 \approx 2.1 \cdot 10^{-7}$, displaces these two colored rays horizontally by about 0.80 mm if they hit the earth surface, calculated at apparent zenith angles of $z_0 \approx 30$ deg. For the virtual case of fastened telescope axes, one would have to move the telescope by about 38 cm along the curved earth surface to see the other end of the K band spectrum of the same star under the same apparent zenith angle $\sin z_0 = 0.5$. In the limit of geometric optics and the limit of zero FOV, an AT of 1.8 m diameter would partially act as a wavelength filter for objects far off the center. In our picture of the starlight as an unvignetted plane wave, there is no such effect. Instead, there is a rainbow

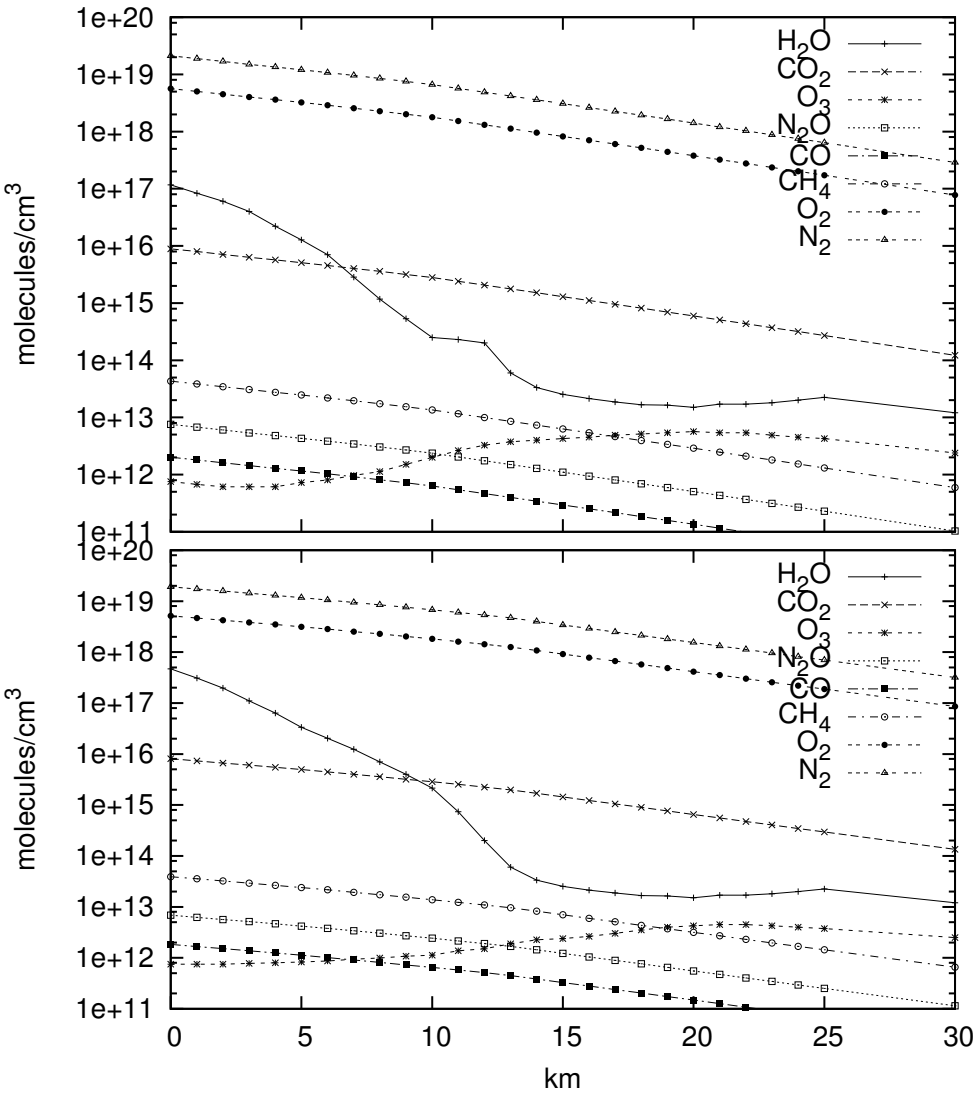

Figure 24: Molecular densities of the "mid-latitude winter" (top) and "mid-latitude summer" standard atmosphere [33]. The major differences are in the modeling of water and ozone.

effect caused by this lensing of the earth atmosphere, which spreads the apparent positions of the two colors on the sky by 12.5 mas, which can also be estimated from Eq. (32) as $\Delta R \approx \tan z_0 \Delta n$ using $\Delta n \approx \Delta\chi_0/2$ from Eq. (37), already mentioned on p. 50. The calculation within the ray optics, however, can be used to consider the distortion/decorrelation induced by turbulence on length scales of these displacements [24].

The effect of pointing errors (in the actual, ordinary sense, here referring to the fact that the telescope cannot point to the PS and SS at the same time) has been discussed elsewhere [88, 89] but is not important for PRIMA (which does *not* try to find a correlation between the fluxes of both star directions). This assumes that the additional tilt ("phasor") of the SS cancels between the two telescopes at the absence of beam rotations.

A bold attempt to verify the predicted offset of the measured OPD as a function of zenith angle

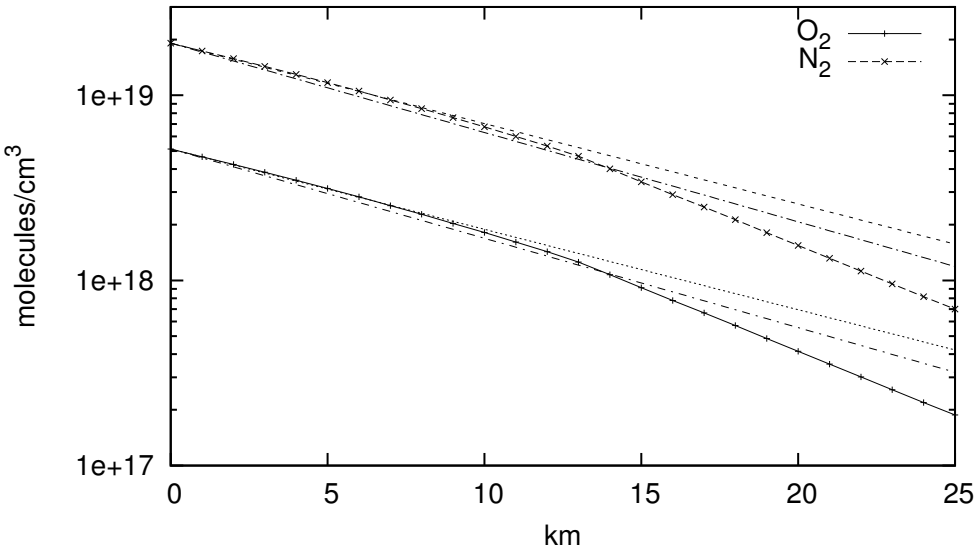

Figure 25: A zoomed version of the molecular densities of the "mid-latitude winter" shown in Fig. 24. The four straight lines in this logarithmic plot are exponential fits to the nitrogen and oxygen densities assuming scale heights of 10 km or 9 km.

[99, 102, 114] with MIDI data taken in 2003/2004 is made with Fig. 28. A very trivial (and obviously leaky) filter was used to eliminate FITS files that would have been created by fringe search scans or where MIDI was not a fringe tracker: only files were admitted where the OPD entry in the `IMAGING_DATA` table was nonzero at the end of the file, had been changed but not by more than 290 μm within the last 1000 exposures. Assuming that the geometric model used for the VLTI remained unaltered over this period and does not use zenith-dependent terms, the offset of the remaining files at the end of the exposure is plotted over the zenith angle derived from the `ISS ALT` keyword in the primary header. At the UT2–UT3 baseline an effect of up to 70 μm for larger airmasses is calculated, but tendencies of that order obviously remain hidden as the noise in the data is of the order of 1 mm. A thorough analysis would inevitably call for a full dis-entanglement of the assumptions made within the OPD model ([172], CMM module `vltipom`) from the air mass parameters, and need some months of work on its own to have some chance of being successful.

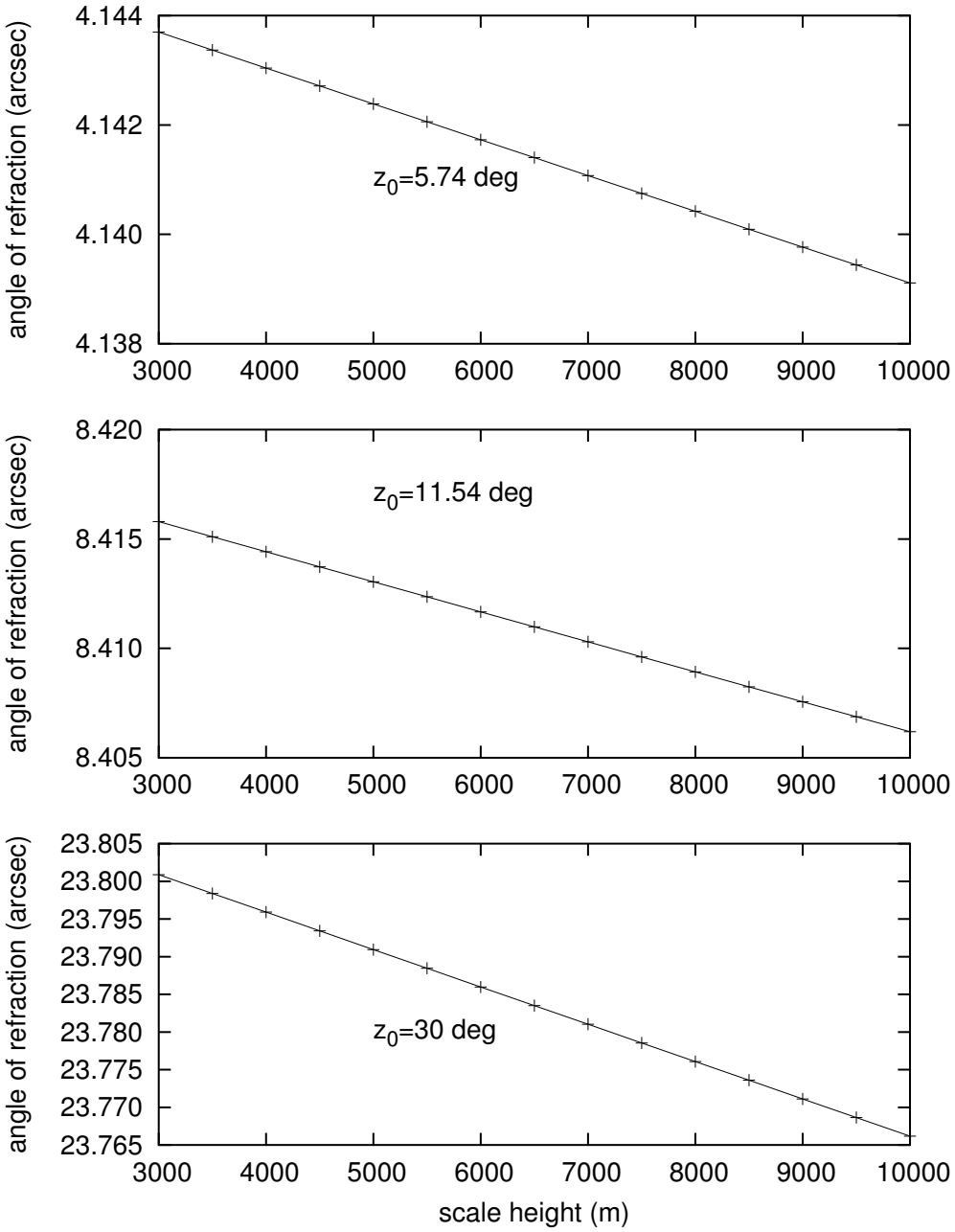

Figure 26: The angle of refraction acc. to Eq. (36) with a susceptibility $\chi_0 = 4 \cdot 10^{-4}$ on the ground (equivalent to $n_0 - 1 \approx 2 \cdot 10^{-4}$), varying scale height K, and three different zenith angles z_0.

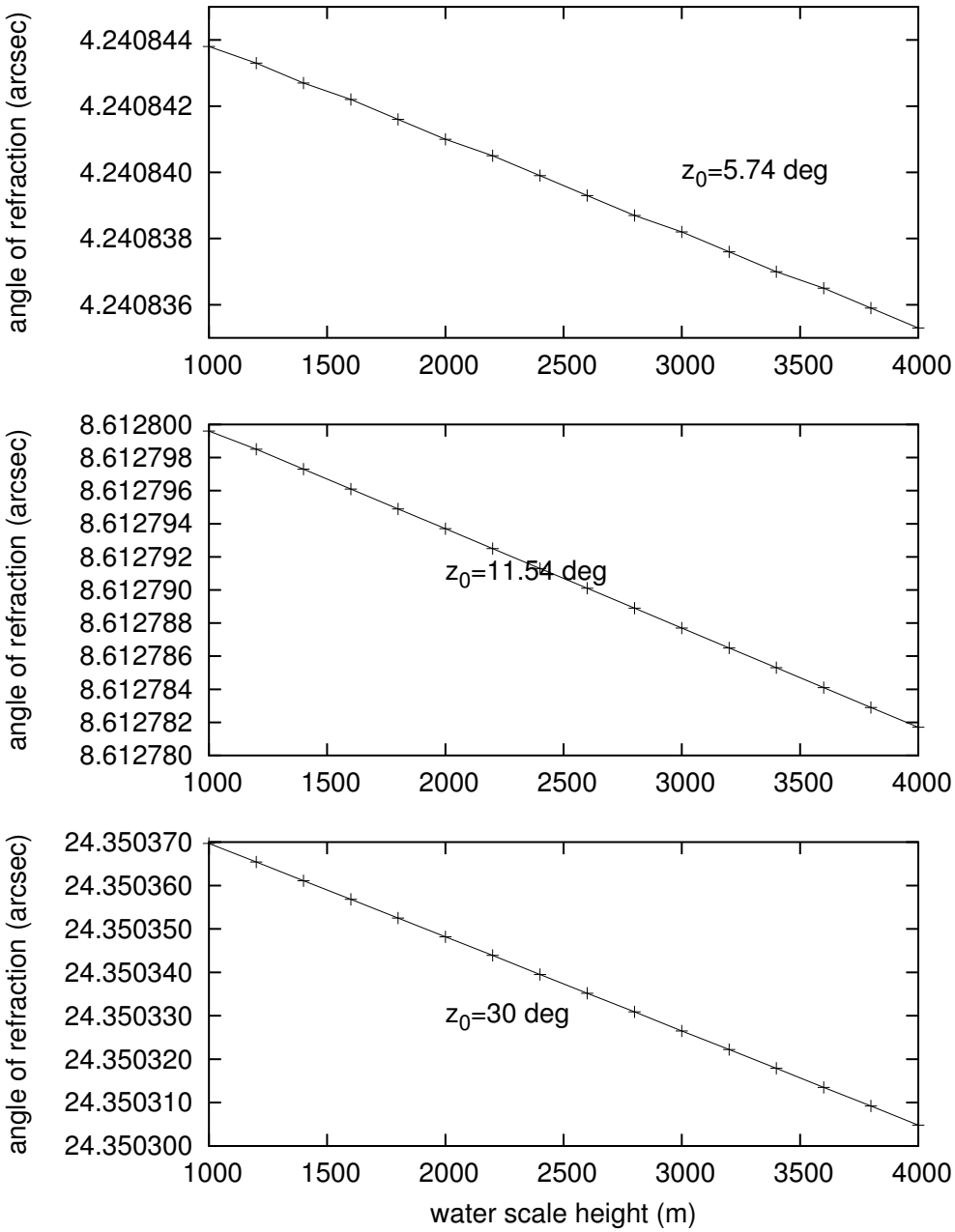

Figure 27: The angle of refraction acc. to Eq. (36) with two air components: one "dry" component with a susceptibility $\chi_0 = 4.0808 \cdot 10^{-4}$ and scale height 10 km, one "water vapor" component with a susceptibility $\chi_0 = 1.75 \cdot 10^{-6}$ and varying scale height, shown for three different zenith angles z_0, $\sin z_0 = 0.1$, 0.2 and 0.5. A typical water scale height is 2 km [98, 155, 176].

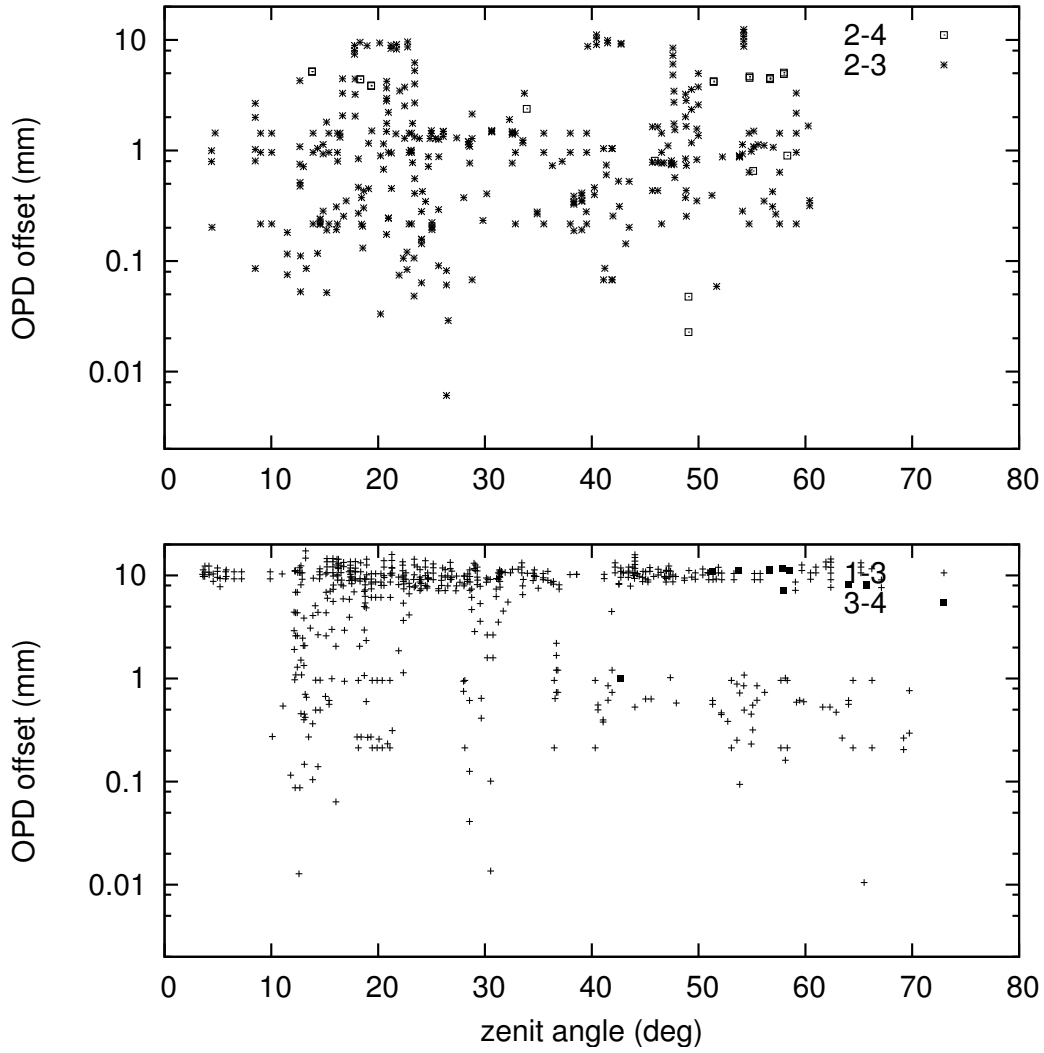

Figure 28: The OPD offset commanded by MIDI to the VLTI DL for a roughly pre-selected set of FITS files obtained in 2003 and 2004, for four different baselines between UTs. There is no obvious correlation between DL position offset and zenith angle.

5.4 Differential Delay with Lensing Effect

The combination of the spherical model (Fig. 23) with the reduction of the different apparent zenith angles to a single optical path difference after M1 in [99, 102] can be summarized in a few examples.

One would expect any effects of the spherical geometry be most pronounced if the baseline is large, the star elevations small (limited for the ATs to zenith angles ≤ 60 degrees [68]), and the differences in the star locations close to the PRIMA limit set by the STS [32, 115]. This coverage of the "cone" of the star separator seems to be set to 1 arcmin [115, fig 2][27], compatible with an expected maximum differential delay of 12 cm at a baseline of 200 m, and also half the FOV at the Coudé Focus, and therefore larger than the 2 arcsec FOV of the AT in the Interferometric Lab.

Table 11 is computed for a model of $\chi_0 = 4 \cdot 10^{-4}$ and a scale height of $K = 10$ km in Eq. (38) by full numerical integration over the three terms in [99, (24)]. The baseline b is the distance between the telescope locations on the earth in the straight line sense of Fig. 23,

$$b = \rho\sqrt{2(1-\cos(z^{(1)}-z^{(2)})} = \rho\left(\Delta z - \frac{(\Delta z)^3}{24} + \frac{(\Delta z)^5}{1920}\ldots\right), \qquad \Delta z \equiv z^{(1)} - z^{(2)}, \tag{40}$$

$$\Delta z = \frac{b}{\rho} + \frac{1}{24}\left(\frac{b}{\rho}\right)^3 + \frac{3}{640}\left(\frac{b}{\rho}\right)^5 \ldots, \tag{41}$$

not somewhere above the atmosphere. The definition of b shown in Fig. 7 becomes fuzzy because the beam separation changes as a function of altitude in the spherical model; the effective baseline b^* of Eq. (35) is also given to show the "lateral" distortion introduced by the atmosphere.

	apparent z_0 (deg)		angle of refr (arcsec)		D (m)	b (m)	b^* (m)	P (m)
	T1	T2	R_1	R_2				
PS	30.	29.9991	23.766175	23.765314	50.009 324 5	100.	100.000 073 168	173.1952
SS	30.000555	29.999656	23.766707	23.765846	50.0101641	100.	100.000 073 170	173.1942
PS	30.	29.998201	23.766175	23.764454	100.017278	200.	200.000 123 821	173.1952
SS	30.005554	30.003755	23.771491	23.769769	100.034071	200.	200.000 123 849	173.1855
PS	53.130102	53.128304	54.770809	54.767246	160.030112	200.	200.000 389 641	119.9605
SS	53.130658	53.128859	54.771909	54.768345	160.031275	200.	200.000 389 659	199.9589

Table 11: Optical path differences D according to [99, 102], the monochromatic case.

In the first line pair in the table, the star separation is 2 arcsec. Equipped with Eq. (34), a blind fringe tracker could predict differential optical path differences of $b\Delta\sin z = b(\sin z^{(1)}_{\mathrm{SS}} - \sin z^{(1)}_{\mathrm{PS}}) = 839.664$ μm, $b(\sin z^{(2)}_{\mathrm{SS}} - \sin z^{(2)}_{\mathrm{PS}}) = 839.671$ μm, or even use the ground-based $bn_0\Delta\sin z_0 = bn_0(\sin z^{(1)}_{0\mathrm{SS}} - \sin z^{(1)}_{0\mathrm{PS}}) = 839.664$ μm, or $bn_0(\sin z^{(2)}_{0\mathrm{SS}} - \sin z^{(2)}_{0\mathrm{PS}}) = 839.672$ μm, close to the value of 839.673 μm obtained by subtraction of the ray tracing results in the first but last column. In the second line pair in the table, the star separation is 20 arcsec, and the predicted differential OPD becomes 16.7929 to 16.7932 mm, which is close to the result 16.7930 mm of the ray tracing. In the third pair of lines, the star separation is 2 arcsec at a lower elevation closer to the AT limit. The results under the heading D of Table 11 can be summarized with Fig. 29. This deals only with the geometry where the two stars and the baseline vector share the same meridian, and probably becomes the worst case in the sense that the lensing effects are larger than placing both stars sideways off the baseline direction.

The examples in the table show that the atmosphere enhances the geometric baseline b by the order 10^{-6} to become b^*, summarized in Fig. 30. The relative size of this effect is about two orders of

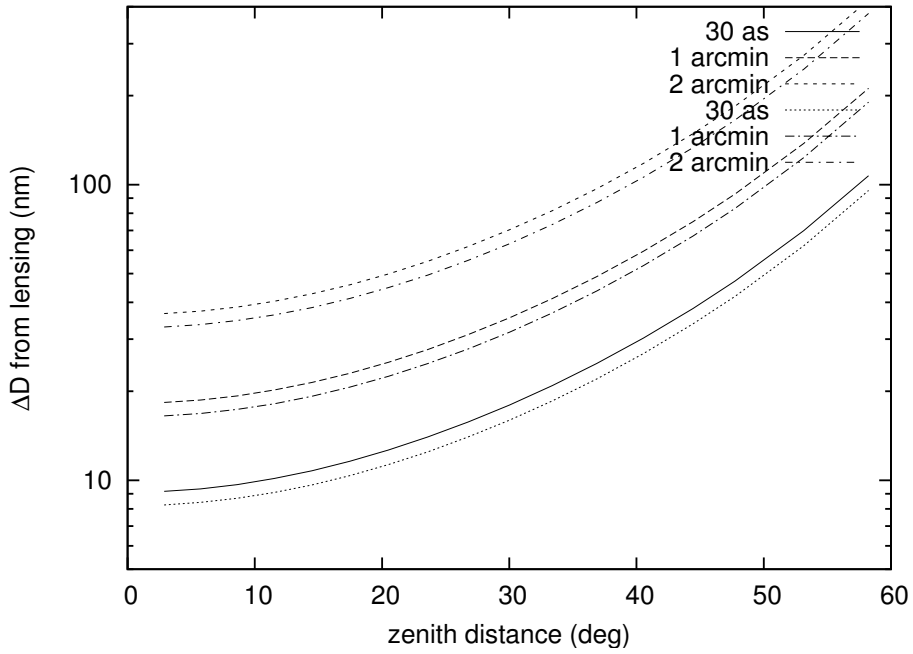

Figure 29: The difference between the differential delay ΔD that is expected from the "plain vanilla vacuum" formula (34) on one hand and calculated from the full numerical treatment of the atmospheric layer model (38) on the other. This is shown for a baseline $b = 200$ m at three star separations between 30 arcsec and 2 arcmin, using a susceptibility of $4{\cdot}10^{-4}$. This is the "differential" view on [99, Fig. 7]. Each line pair represents two calculations at scale heights of 10 and 9 km to give an idea of which error is introduced switching between the two models shown in Fig. 25.

magnitude smaller than the typical $n_0 - 1$ factor for the OPD's on the ground, but yet it may mean that b^* is about 400 μm larger for low star altitudes than the geometric baseline b on the ground. The baseline calibration for PRIMA is aiming at an accuracy of 50 μm, and therefore cannot neglect this airmass dependence. [It should be noted that the effect may be a factor of 10 stronger if the top atmospheric height H is reduced to only some 40 km instead of integrating the long tail of the exponential model (38). This can be understood on the basis of the sudden kink in the ray paths introduced at low altitudes and therefore higher atmospheric curvature.]

The lensing effect on ΔD and b enlarges both values, which means that the reduction to $\tau = \Delta D/(b\cos z)$ (see [162, Sec. 29] for the general formula for arbitrary azimuths and double star orientation) benefits from some cancellation effects in the errors that one would make by ignoring the atmospheric lensing at all.

The chromaticity within this results is characterized in Tab. 12.

The analysis in [99, 102] is made to remove the numerical noise that arises from massive cancellation of significant digits in the full numerical treatment of the integrals; it confirms that no major residual errors remain from the spherical shape of the earth atmosphere, as one extrapolates the laboratory data (measured actual differential OPD and known baseline) to astrometric distances on the sky. Simple formulas like Eq. (34) suffer from an inherent imprecision in the selection of which of the "available" zenith angles of the two stars in the two telescopes is to be used, which may accumulate to about a micrometer as shown in the examples above.

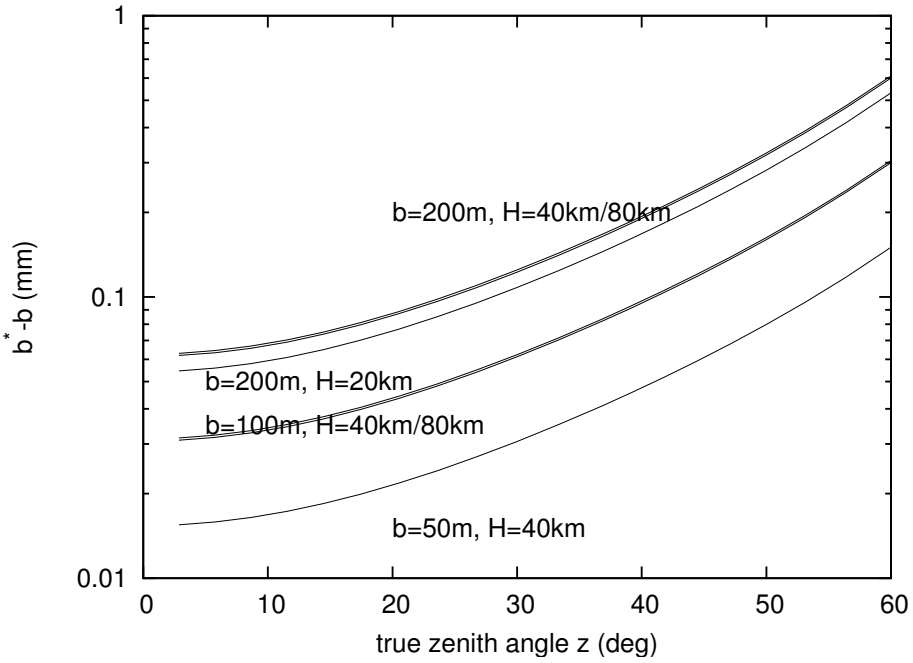

Figure 30: The difference $b^* - b$ between the length of the effective baseline above the atmosphere and the geometric baseline on the ground according to [99, 102], parametrized through the exponential model (38) at $\chi_0 = 4 \cdot 10^{-4}$ and scale height $K = 10$ km, which is cut off at $H = 20$, 40 or 80 km.

λ (μm)	χ_0	z_1 (deg)	b (m)	D (m)
2.05	$4.07898 \cdot 10^{-4}$	30.0067	100	50.009 516 7
2.25	$4.07791 \cdot 10^{-4}$	30.0067	100	50.009 514 0
2.45	$4.07690 \cdot 10^{-4}$	30.0067	100	50.009 511 5
2.05	$4.07898 \cdot 10^{-4}$	30.0067	200	100.017 673 9
2.25	$4.07791 \cdot 10^{-4}$	30.0067	200	100.017 668 6
2.45	$4.07690 \cdot 10^{-4}$	30.0067	200	100.017 663 5
2.05	$4.07898 \cdot 10^{-4}$	53.1456	200	160.030 745 4
2.25	$4.07791 \cdot 10^{-4}$	53.1456	200	160.030 736 8
2.45	$4.07690 \cdot 10^{-4}$	53.1456	200	160.030 728 7

Table 12: The spherical geometry introduces a delay D which differs between the two ends of the K band by a few μm at zenith angles of 30 deg, and by up to 17 μm at large zenith angles z and baselines b. D is positively correlated with the susceptibility χ_0, which partially cancels the refractive index dispersion experienced in the tunnel in Eq. (5).

In summary, the assessment we find in the Glossary of [4] "*External optical path difference.... It is computed by using the formula:* $\mathrm{OPD}_{ext} = SB$ *(where* S *is the unit vector pointing to the object, and* B *the baseline vector.*" turns out to be missing a vital additional contribution to the differential external OPD.

6 APPENDIX

6.1 GENIE sensors: de-facto VLTI Tunnel Humidity

A history of the humidity measured in the VLTI tunnel is available from the URL http://www.strw.leidenuniv.nl/~mathar/vlti/ [2, 3]. A summary over these summertime indoor humidities and temperatures in the first months at the four sensor locations is given in Fig. 31. One gets some impression from the outside at which times people have been busy in the tunnel, but we do not have log-books that would allow to associate times of VLTI observations with "calm" periods, for example, which one would optimistically select as reference data of PRIMA observations in the future. (VLTSW20050031 indicates that the duct cover status is presumably logged for times later than March 2005.)

Fig. 38 plots the differences between pairs of lines already contained in Fig. 31 to look for a global horizontal gradient of temperature or humidity. The distance between the sensor locations referred to in Fig. 38 is 128 m (subtracting the u coordinates of UT1 and UT4 in [177, Tab 3-1]), which means a typical difference of 0.02 mole/m^3 in the upper plot of Fig. 38 is equivalent to a gradient of $1.56 \cdot 10^{-4}$ mole/m^4; neglect of such a gradient would add an error of 2.1 μm to a (non-differential) OPL of 50 m, or an error of 8.2 μm to an OPL of 100 m, which is the product of the gradient in the index of refraction by the square of the path length. Dividing the typical magnitude of the values in the upper part of Fig. 38 by those in the upper part of Fig. 31 one might also conclude that the spatial *gradient* in the humidity comprises 10 to 20 % of the total contribution of humidity to the OPL. This implicitly translates any requirement on the knowledge of the OPL into a request on the maximum spacing of the humidity sensor stations. However, the PRIMA requirement on a doubly-differential OPL, i.e., a differential OPD, is not of that simple kind, and even for a non-differential determination of an OPD (MIDI, VINCI), details depend on which of the two beams runs how much of its path "uphill" or "downhill" this gradient, to cancel none or all of this effect as a function of the u-coordinate of the telescope station [101].

For comparison: a human would evaporate at least 35 g water per hour at 18°C [16, M14 Tab 5]; each hour of presence in the DL tunnel of ≈ 2400 m^3 increases the humidity on the average by 0.001 mole/m^3.

A much denser temperature-only sensor network exists aside the one summarized here, to which we have no remote access [80]. (By accident, one of these data points is reported in instrument data files, which leads to Fig. 36.) In the light of this fact we to not try to comment on the temperature distribution based on our sparse, 4-sensor network readings. We only conclude for know that the water density has no similarly predictable spatial gradient as is reported for the temperature [79, 148].

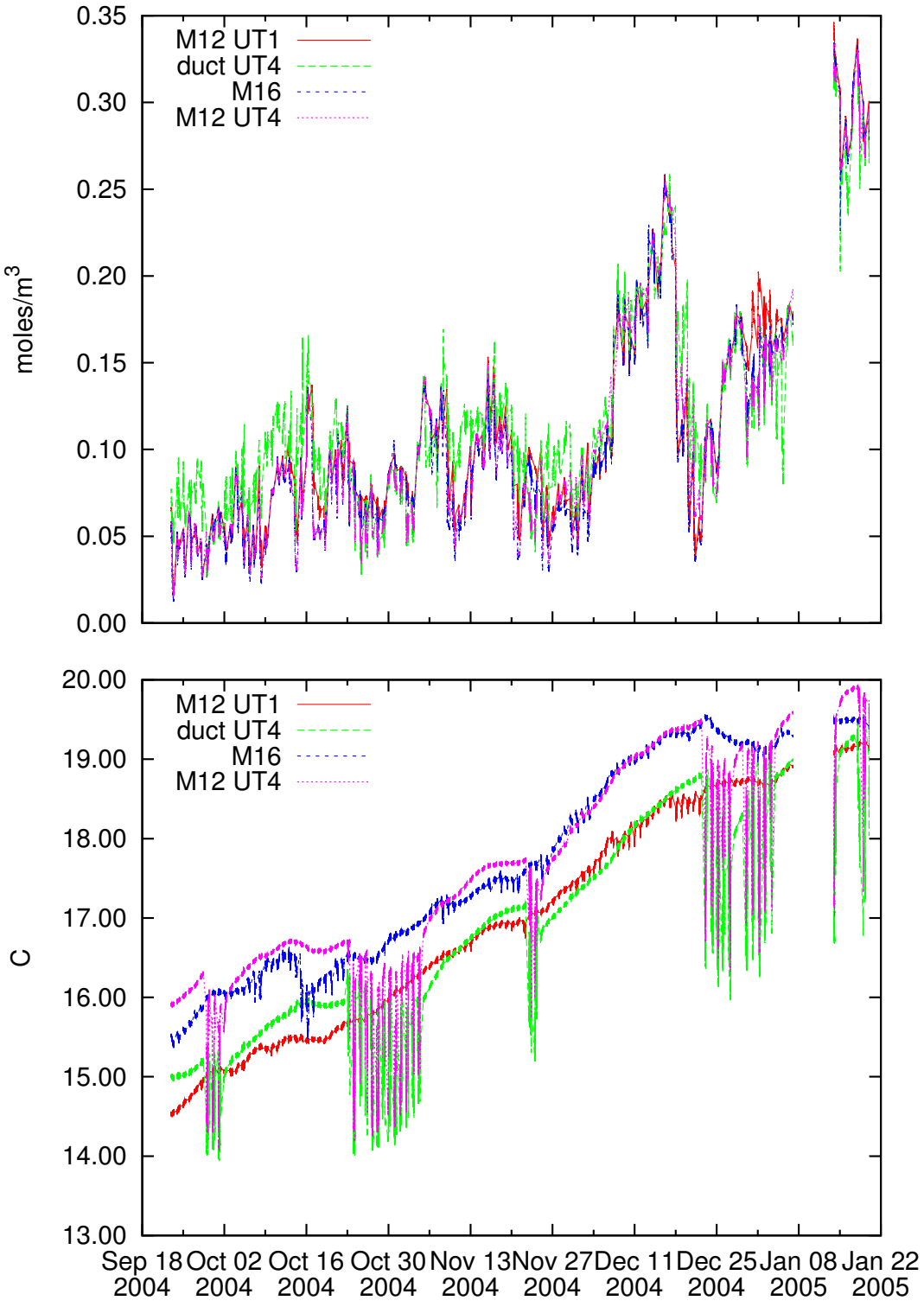

Figure 31: The time series of humidities and temperatures during the first 4 months after installation of the T/H sensors in the VLTI DL tunnel. Only night time data are shown, and converted from the percentages actually provided to a molecular density at the local temperature. Note that the temperatures represent early and mid summer time on the southern hemisphere.

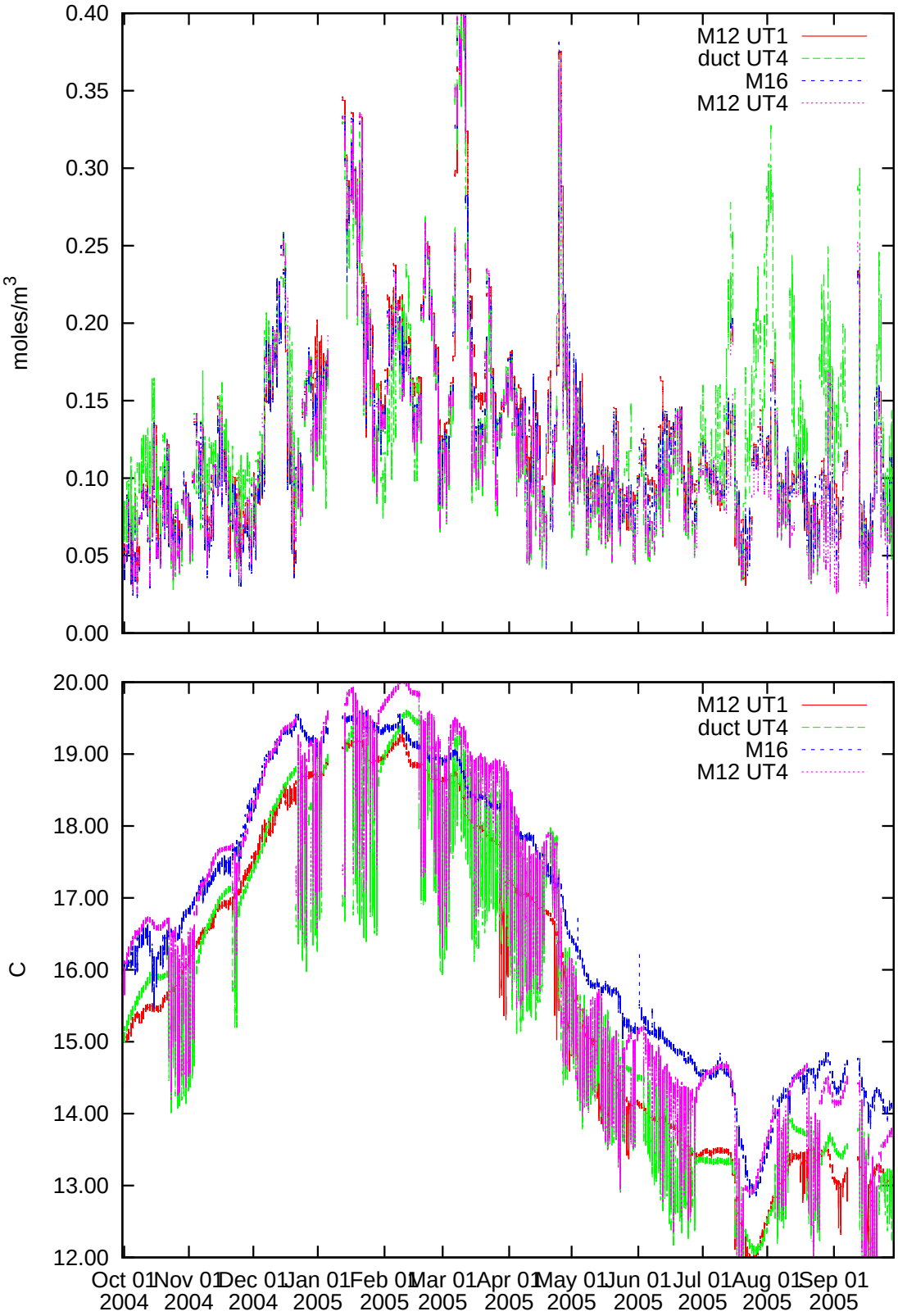

Figure 32: The data of Fig. 31 over a longer period of 1 year.

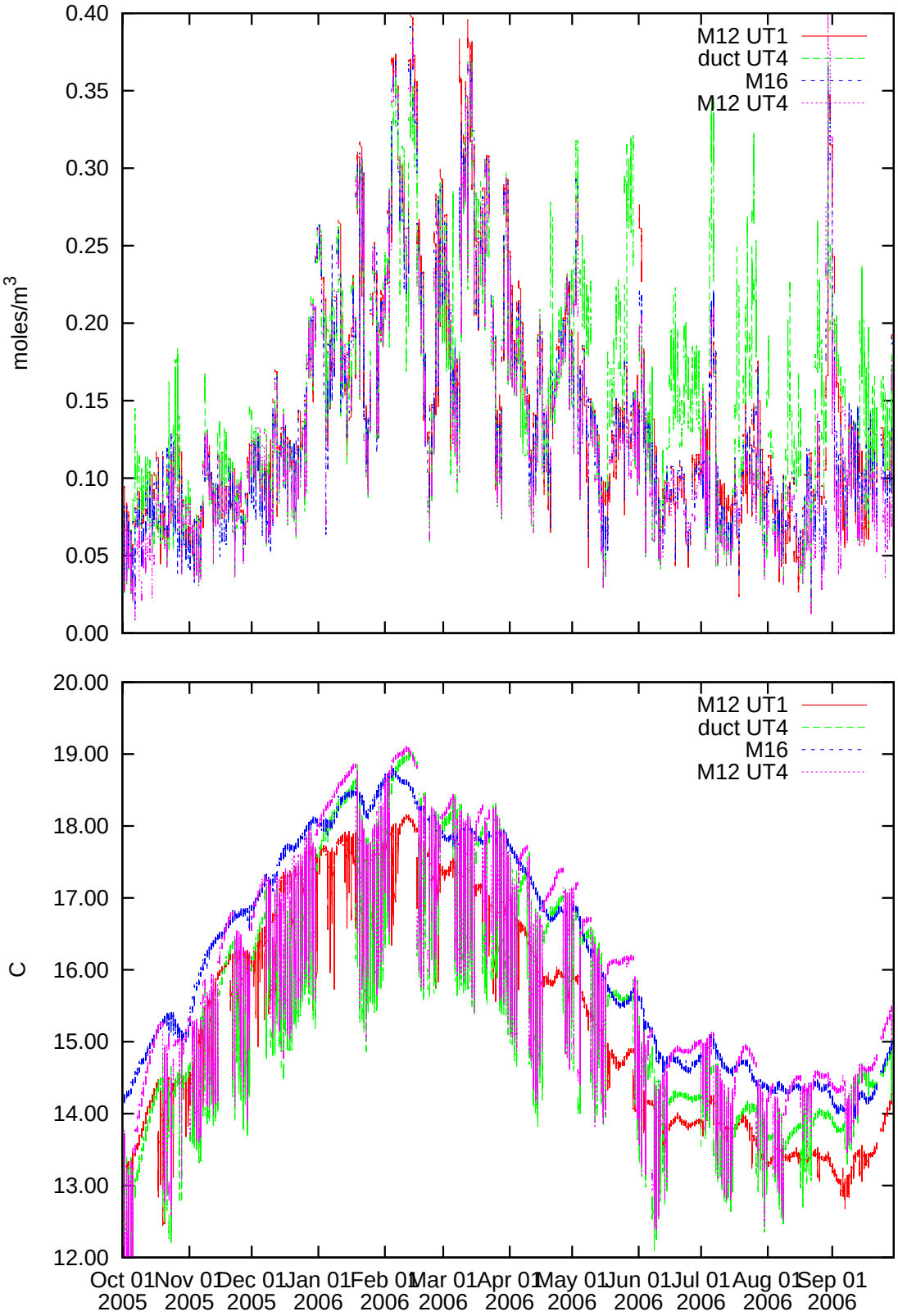

Figure 33: The data of Fig. 32 continued into 2006.

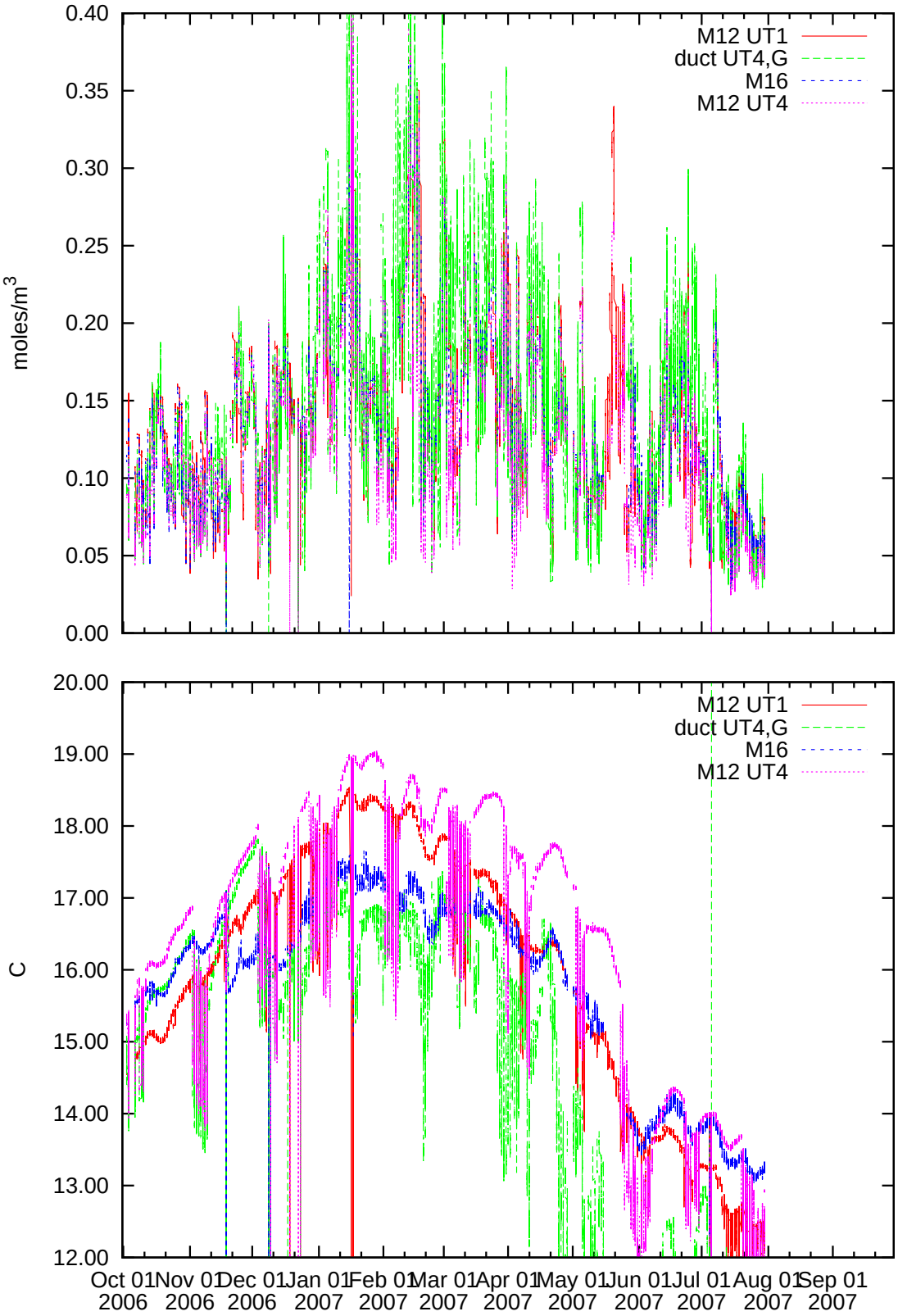

Figure 34: The data of Fig. 32 continued into 2007.

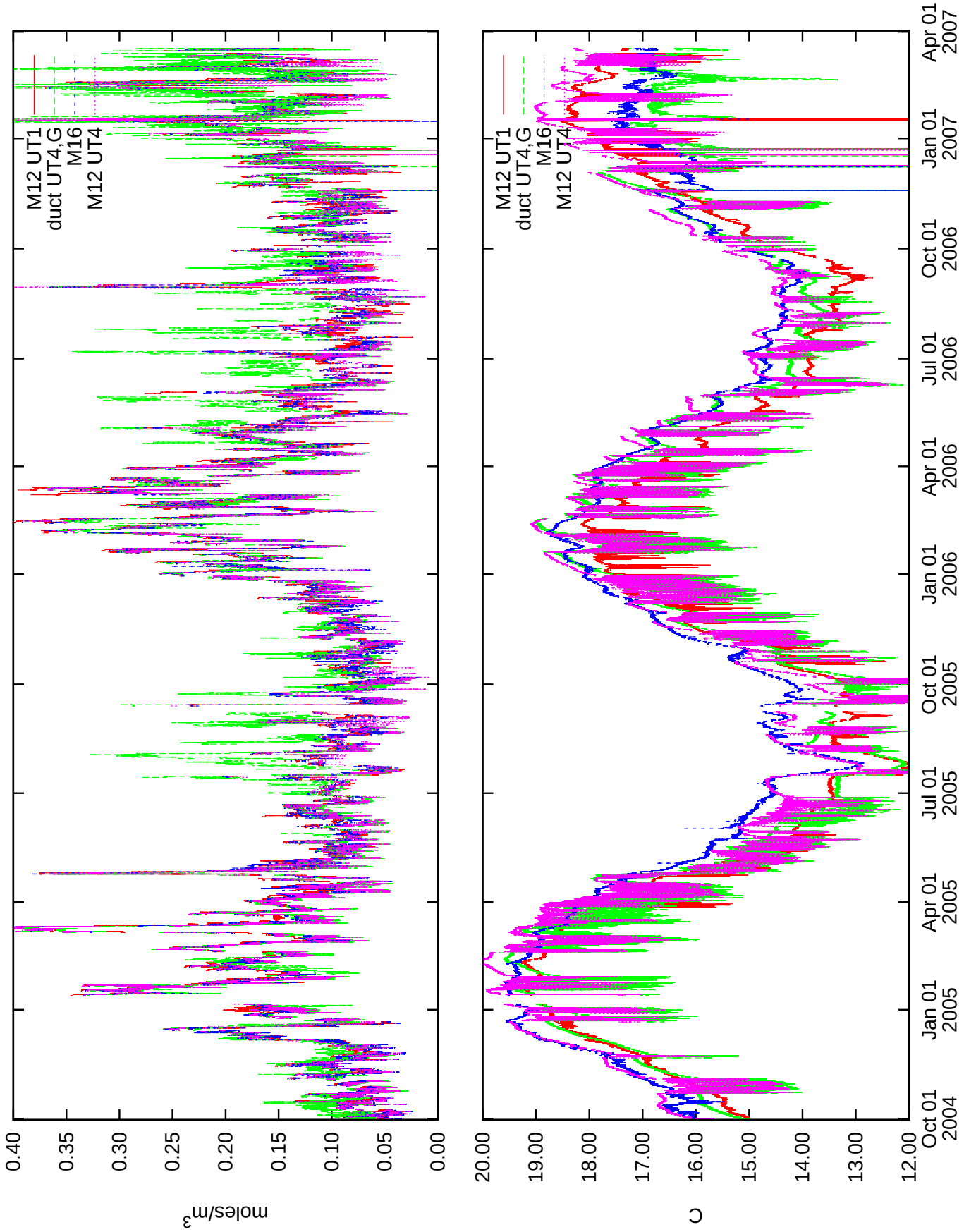

Figure 35: The data of Fig. 32–34 combined.

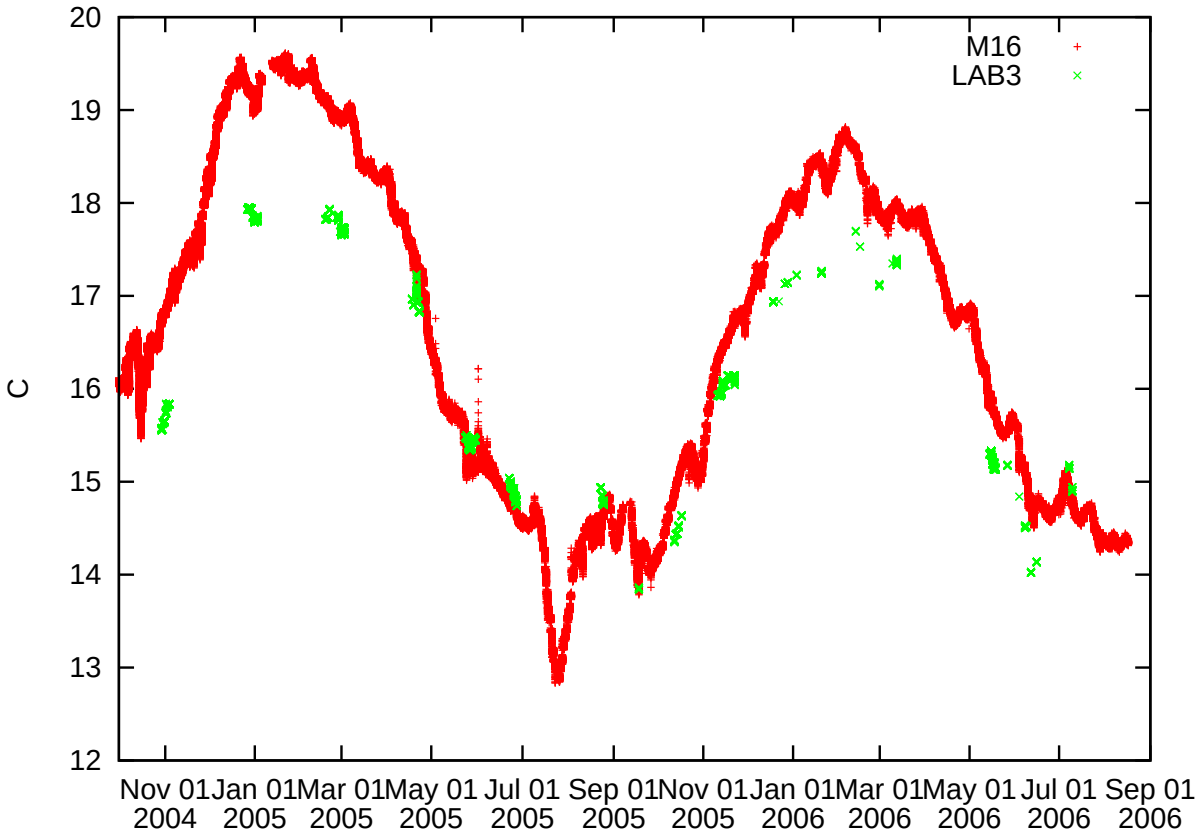

Figure 36: The temperatures of the GENIE humidity sensor near M16 (red, same as in Fig. 35) are compared to temperatures reported in MIDI primary header keywords `ISS TEMP LAB3` (green). According to the ISS dictionary, the green crosses are from a sensor at the VLTI laboratory East wall, according to [80, Fig 2] from a sensor at the West wall. (These are obviously only extracted from FITS files of MIDI runs to which the author has had access to.)

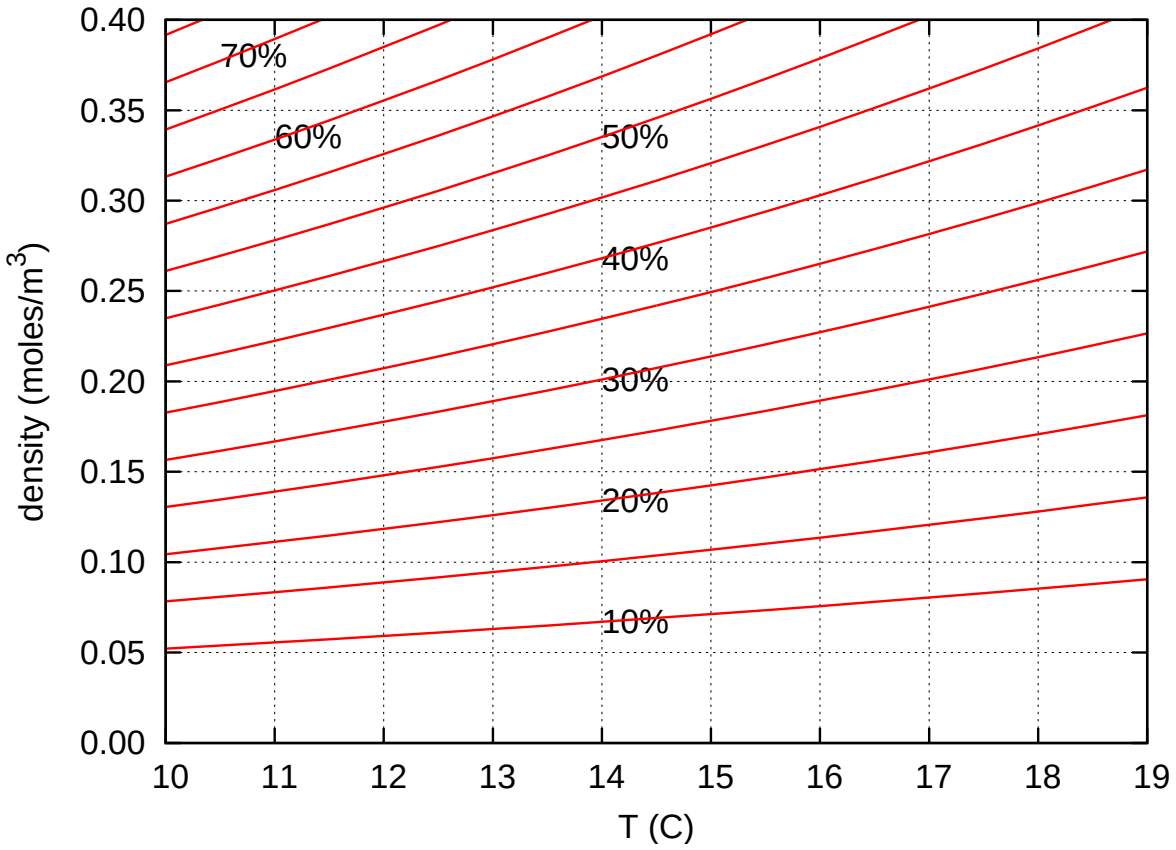

Figure 37: This figure facilitates the conversion of relative humidity to absolute humidity up to 0.4 moles/m^3 for air temperatures between 10 and 20°. The virials of [171] are applied to get the equation-of-state.

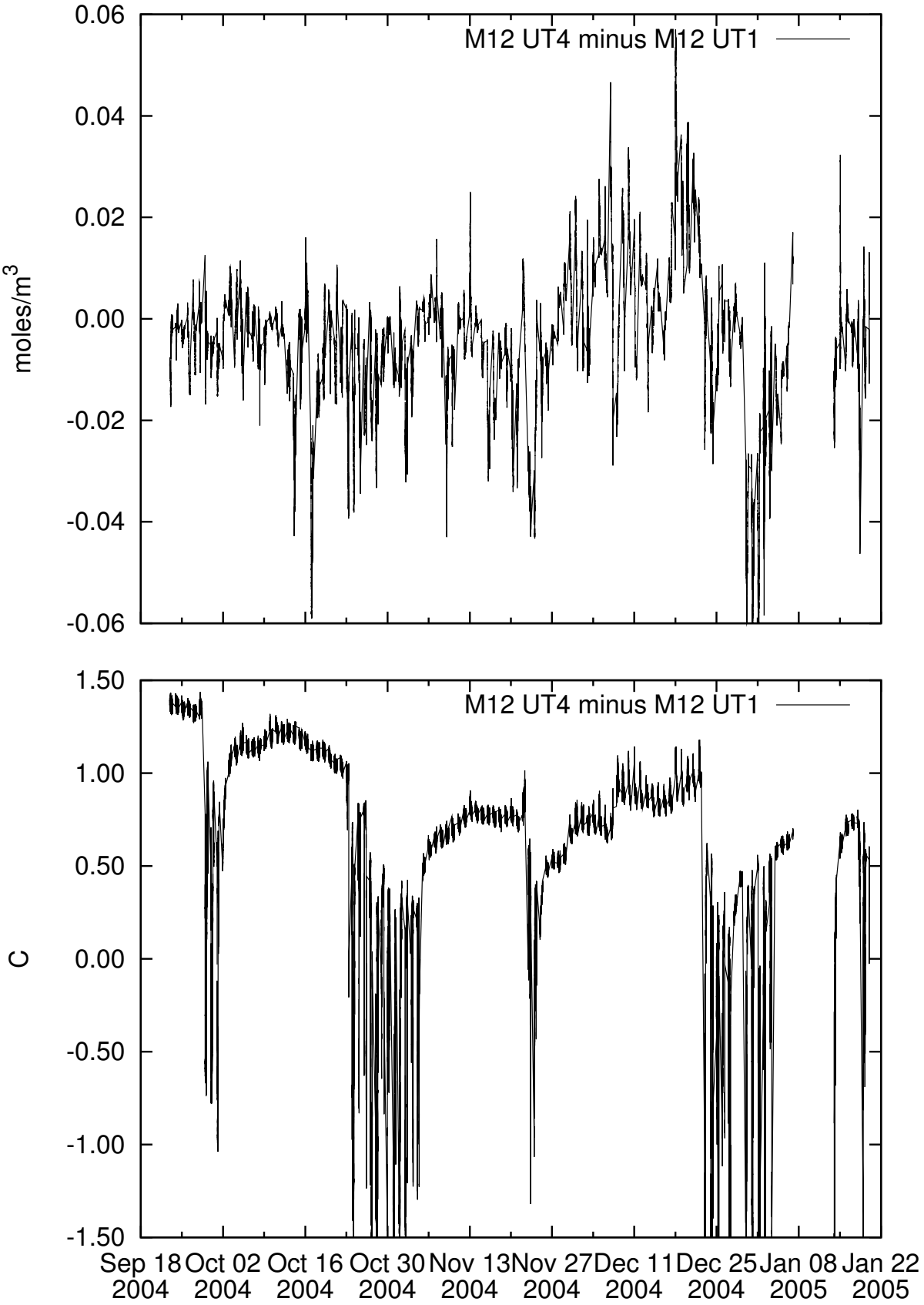

Figure 38: This time series covers the months as in Fig. 31 but looks at the horizontal gradients of temperature and humidity. The values at the sensor location close to M12 of UT4 have been subtracted from the values close to M12 of UT1 at each point in time. Lower graph: M12 for UT4 has typically been warmer than M12 for UT1 by 1/2 to 1 degree. Upper graph: There is no obvious equivalent bias in the horizontal water vapor density gradient.

Since the PRIMA observations are covering time intervals of about half an hour [28, 31], a statistics of temporal variations within these four time series is also of interest: The difference between the minimum and maximum humidity at each of the sensor locations is computed by slicing the night time data into consecutive, non-overlapping slots of 5 (Fig. 39), 10 (Fig. 40) or 30 minutes (Fig. 41) duration. Obviously, the most probable variation shifts to the right (larger amplitude of the humidity variation) as the time slot interval increases. We see that the humidity variations at the M12 of UT1 and at M16 are smaller than the variation measured within the light duct of UT4. Insertion of a typical variation of $\chi_w = 0.001$ mole/m^3 changes the susceptibility χ_w by about $1.05 \cdot 10^{-8}$, which is equivalent to an OPL change of 0.5 μm per 100 m path length. To an (open loop) fringe tracker this would set some minimum frequency of updating the tracker's parameters that depend on the actual humidity in the tunnel. Unfortunately we also see—in comparing Fig. 38 with Figs. 40-41—that the spatial inhomogeneity of the water density seems to be much more an issue than the temporal stability.

The correlation between the indoor humidity and the humidity measured at the Paranal weather station in Fig. 43 and 44 shows that at low and medium humidity (up to 0.2 mole/m^3) the volume concentration in the tunnel is higher than on the platform, which a posteriori confirms earlier suspicions [110]. One might suspect that this is a simple artefact of the different temperatures at the weather pole and inside the tunnel. Fig. 45 demonstrates that this is not the reason, as the reduction of the units to the local mixing ratios still displays a higher amount of water in the tunnel than outside.

At some time in the past, covers at the crossing of VLTI ducts into the DL tunnel have been installed, which may have taken influence on the humidity patterns. (This is a blind statement as I have no further information on when this happened and at which points in time these are open or closed.) It therefore makes sense to re-plot these correlations for other times of the year and later on, which is done in Figure 46.

The spatial correlation within the tunnel system (Fig. 48) is larger than to the outside.

Finally, the power spectrum of the humidity time series is shown in Fig. 49.

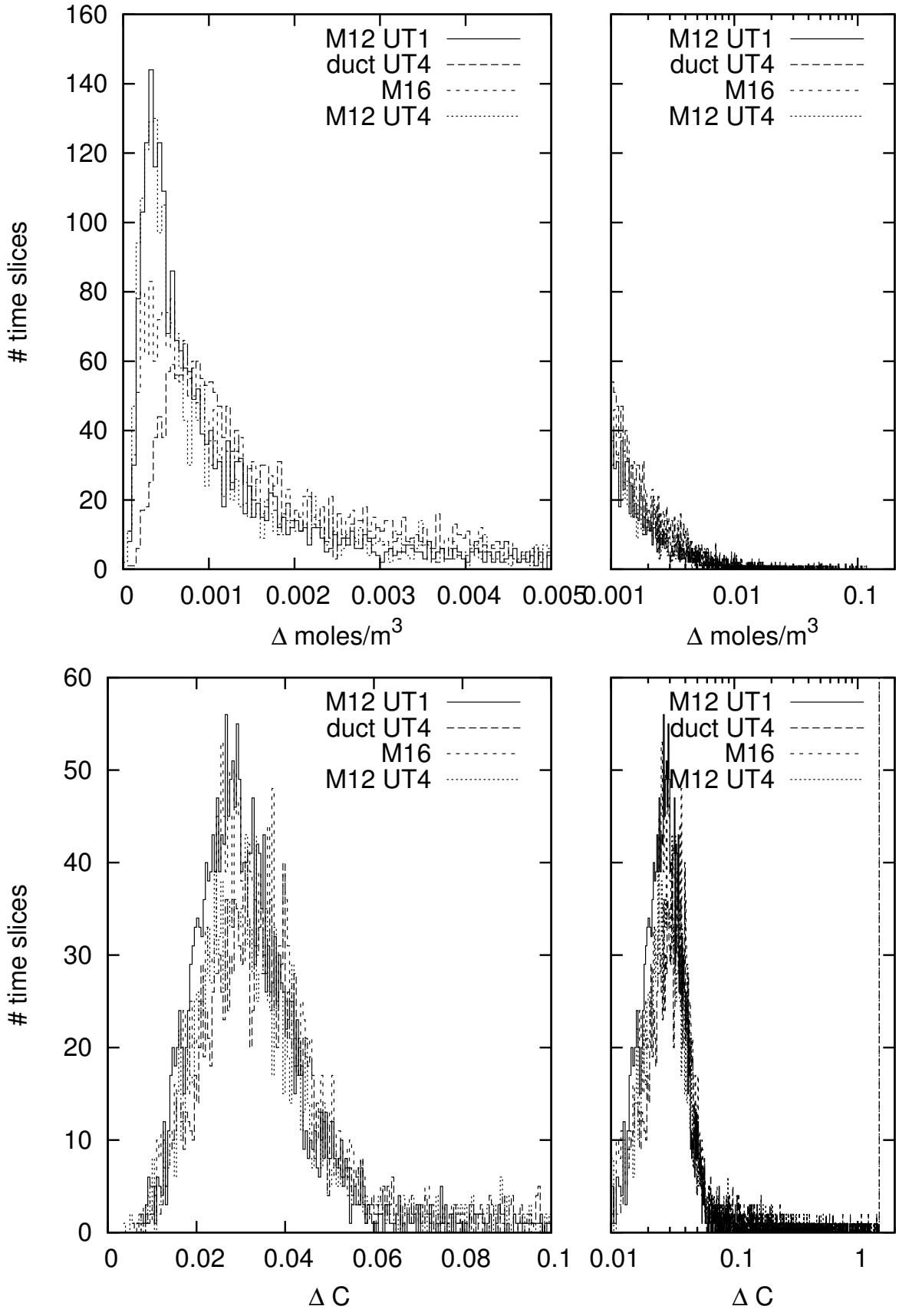

Figure 39: The time series of Fig. 31 interpreted as the variability in non-overlapping consecutive time intervals of 5 minutes duration. The smaller graphs on logarithmic scales have been added to give an idea on the probability of "sudden" changes, represented by the tails to the far right. 100 % of the data is equivalent to a total of 2399 slices.

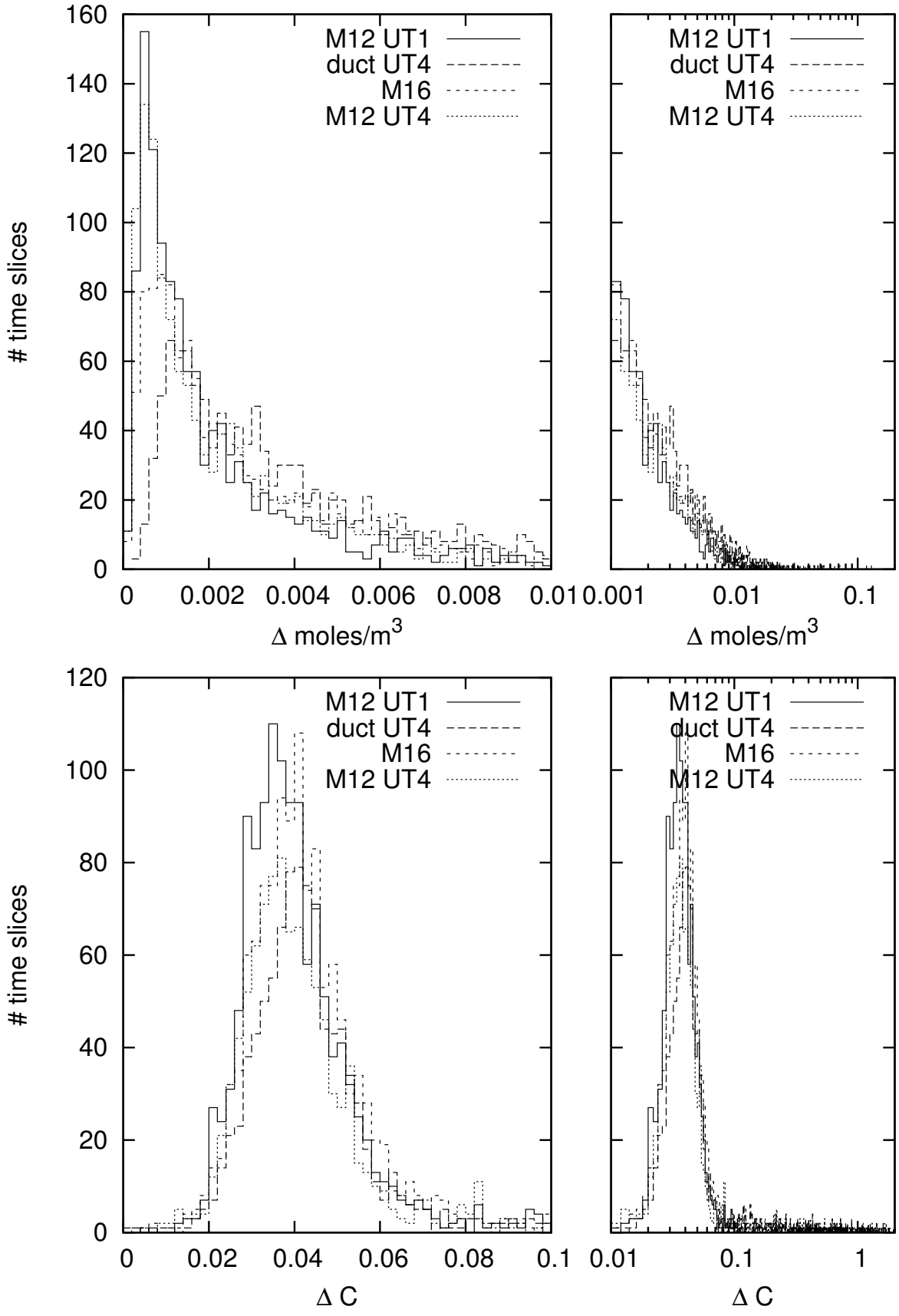

Figure 40: The time series of Fig. 31 interpreted as the variability in non-overlapping consecutive time intervals of 10 minutes duration. 100 % of the data is equivalent to a total of 1250 slices.

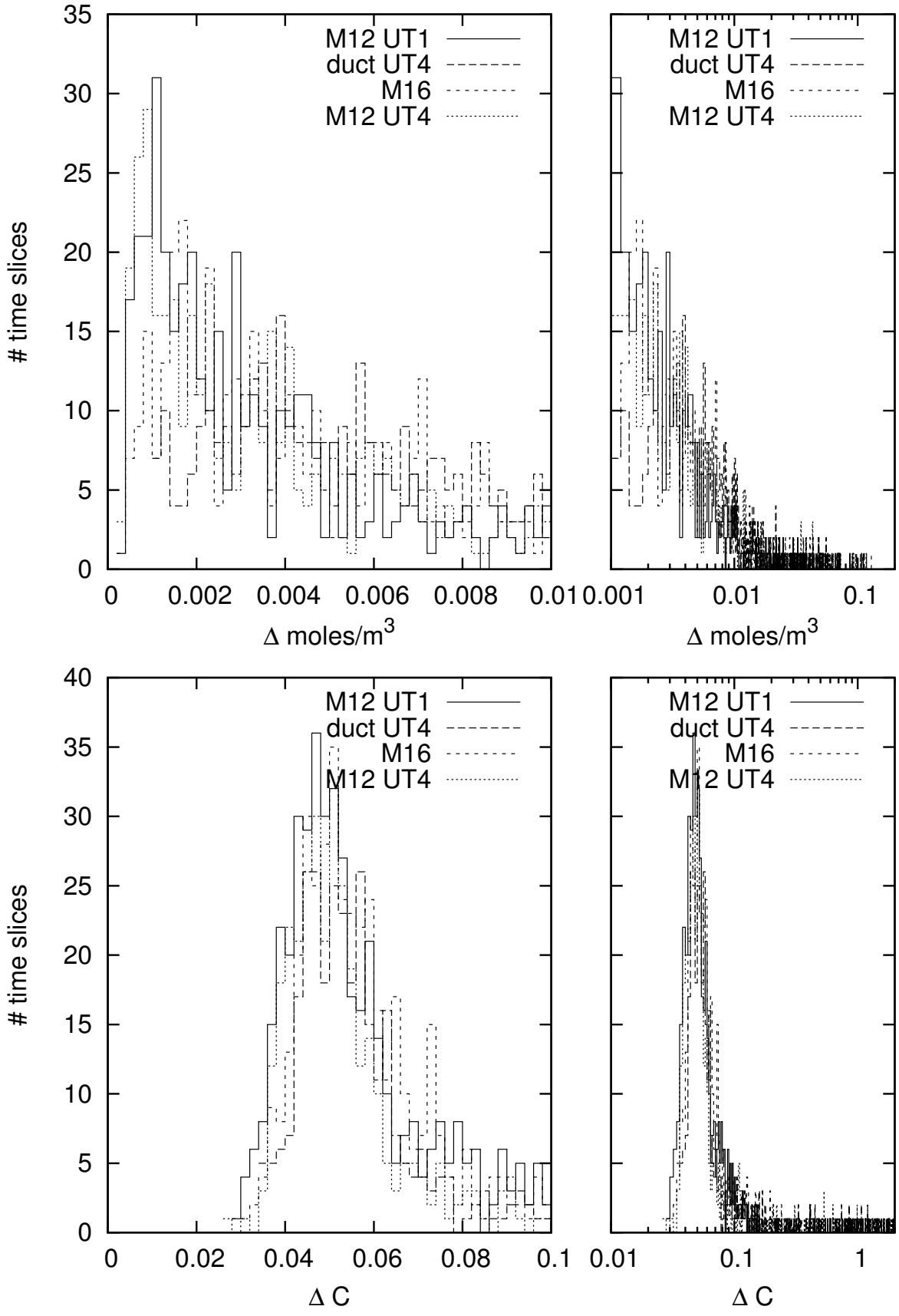

Figure 41: The statistics of Fig. 40 after increasing the time intervals to 30 minutes. 100 % of the data is equivalent to a total of 474 slices (which obviously is only about 1/3 of the slices of 10 minutes duration).

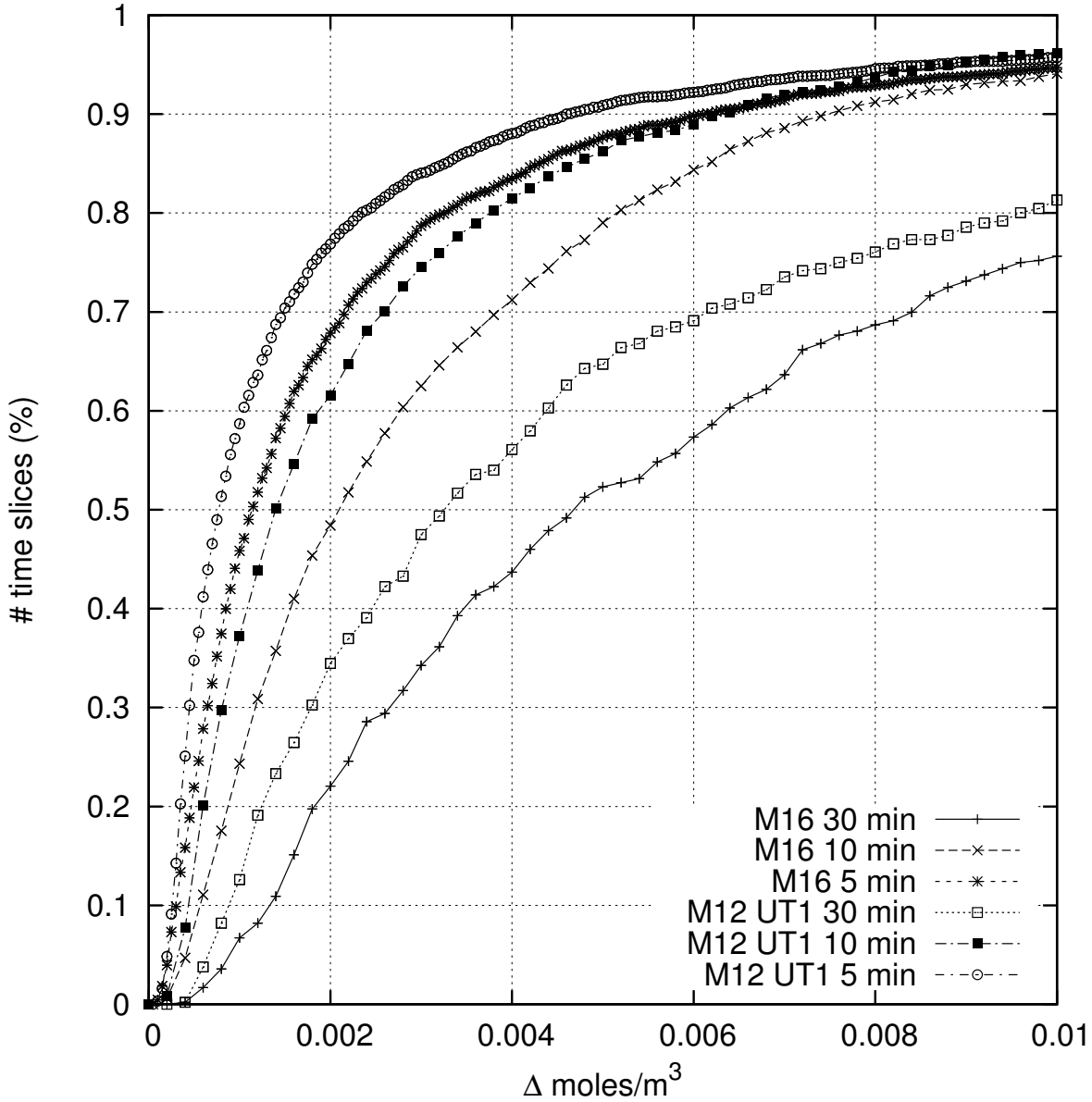

Figure 42: Some of the probability density functions of Figs. 39–41 are here converted into accumulated density functions. We see that there is a probability of 50 % of having fluctutations of 0.0046 mole/m^3 or less monitoring the humidity near M16 over 30 minutes, for example, or that there is a probability of 50 % of having fluctutations of 0.0008 mole/m^3 or less monitoring the humidity near M12 of UT1 over 5 minutes.

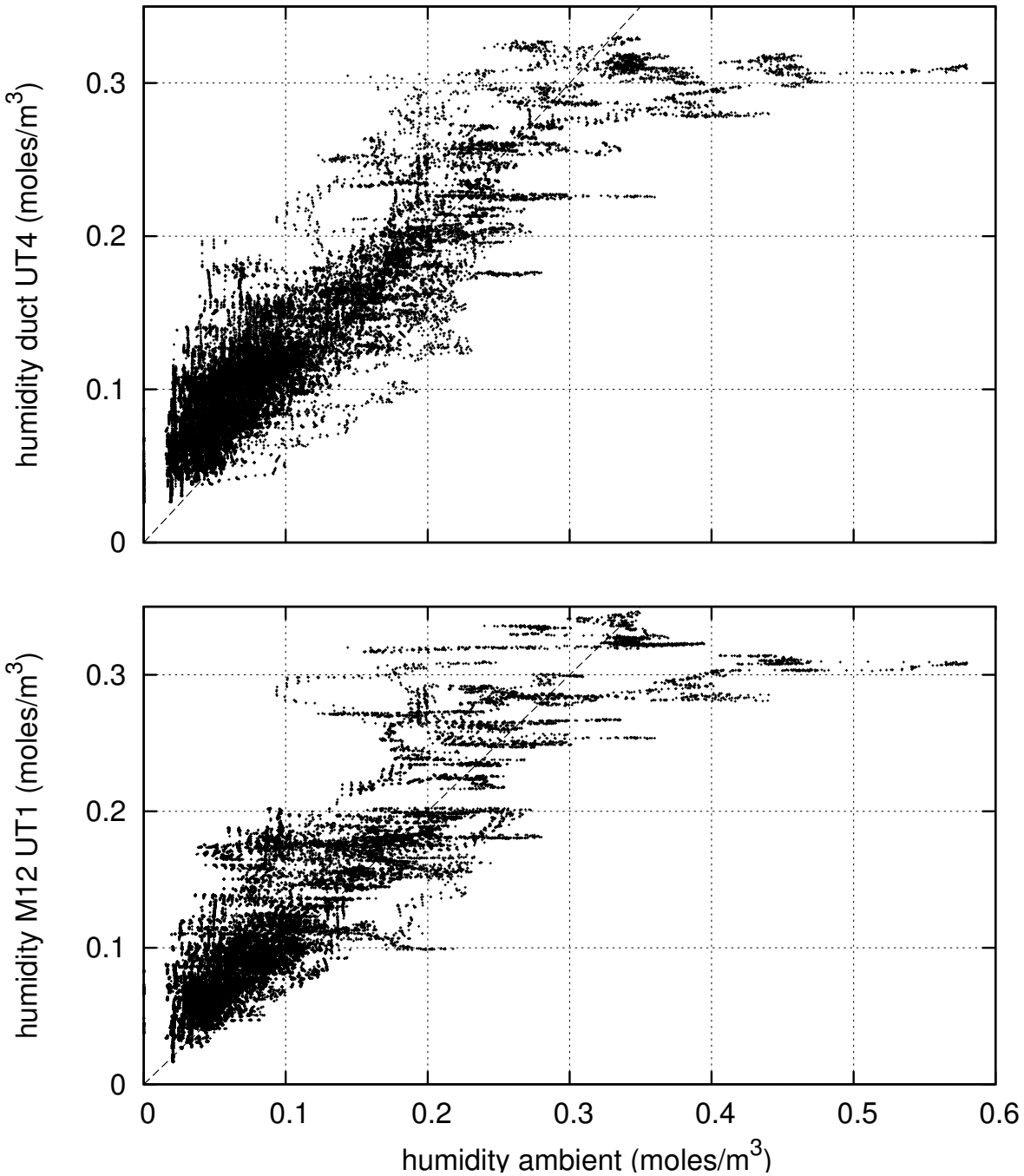

Figure 43: For the available nighttime data between Sep 22, 2004 and Jan 20, 2005, two of the indoor humidities and the ambient humidity are converted to water gas densities at their local temperatures, and correlated with each other. The dashed line on the diagonal is a guide to the eye.

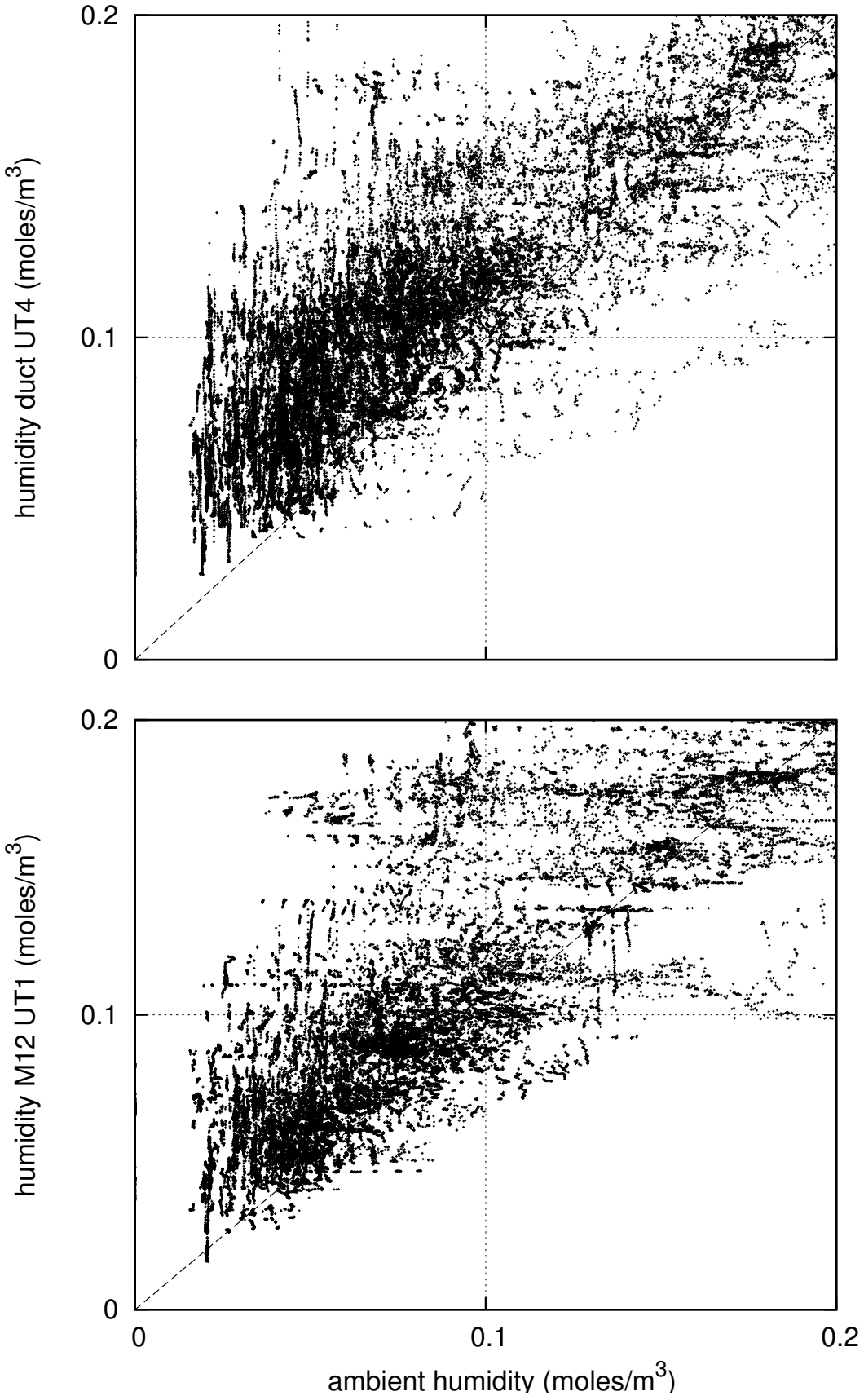

Figure 44: A magnified view onto the lower left part of Fig. 43.

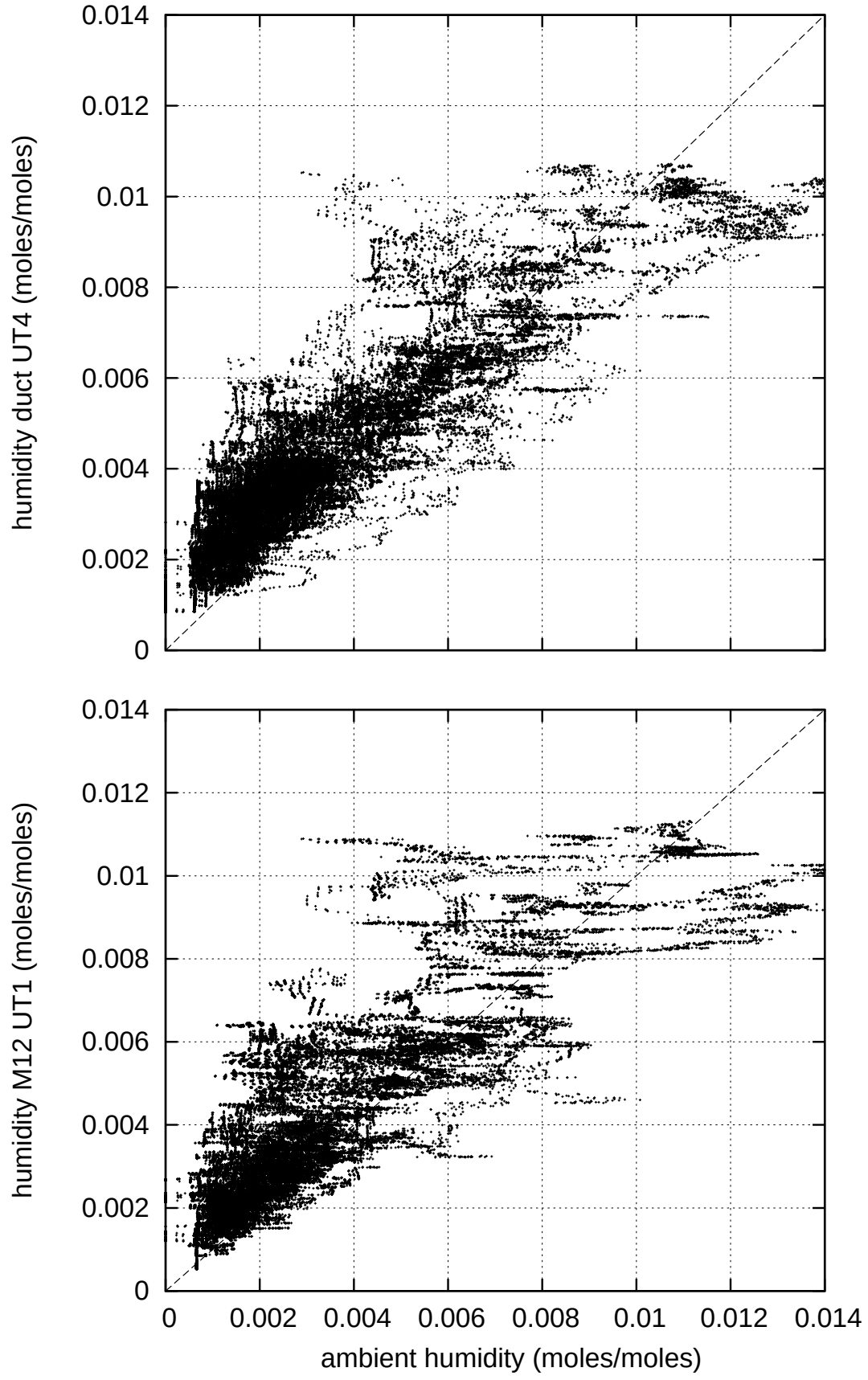

Figure 45: The molar mixing ratios for water vapor in units of the total molecular number density for nighttime data between Sep 22, 2004 and Jan 31, 2005.

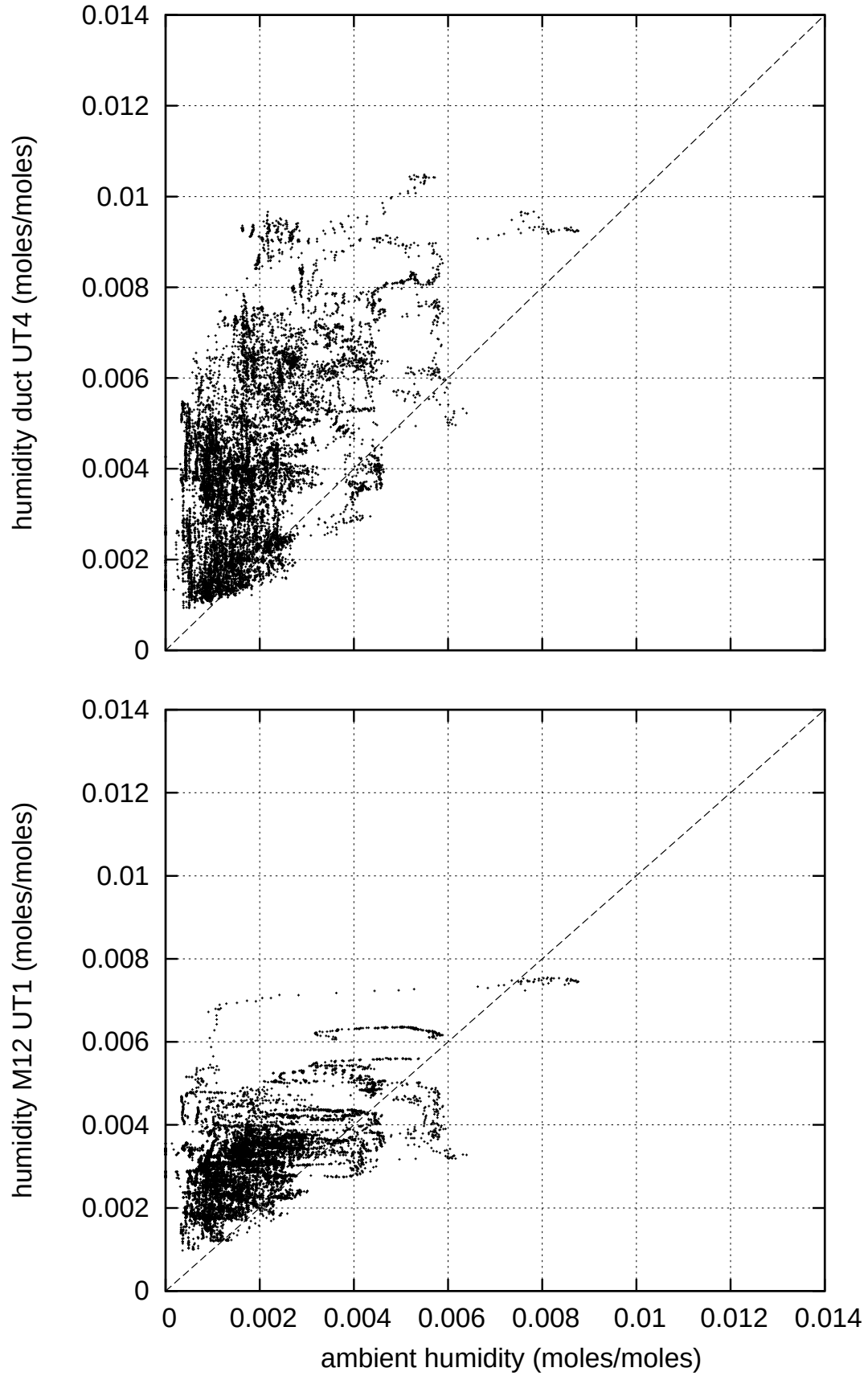

Figure 46: The molar mixing ratios for water vapor in units of the total molecular number density for nighttime data between July 1, 2005 and Sep 30, 2005.

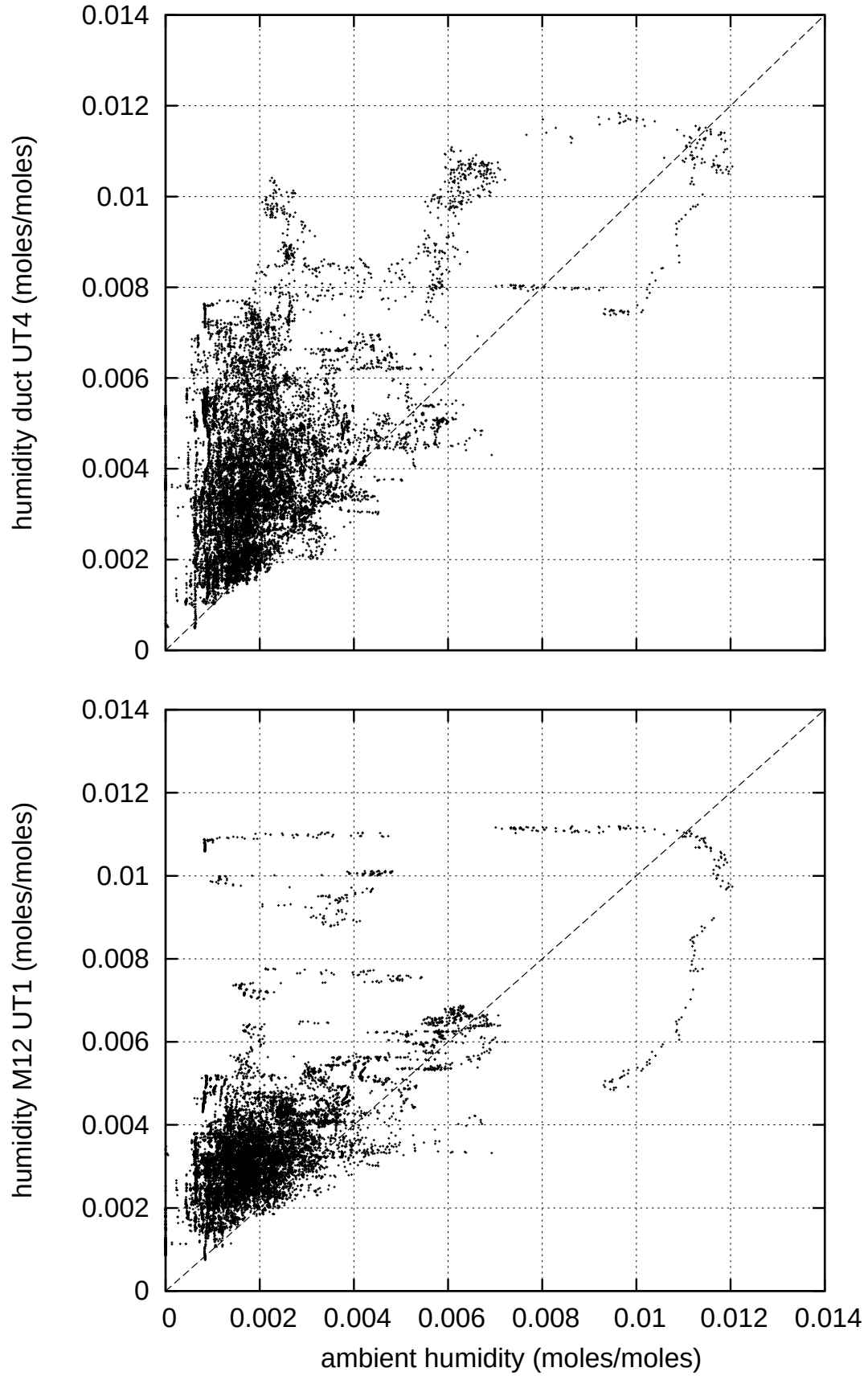

Figure 47: The molar mixing ratios for water vapor in units of the total molecular number density for nighttime data between July 1, 2006 and Sep 30, 2006.

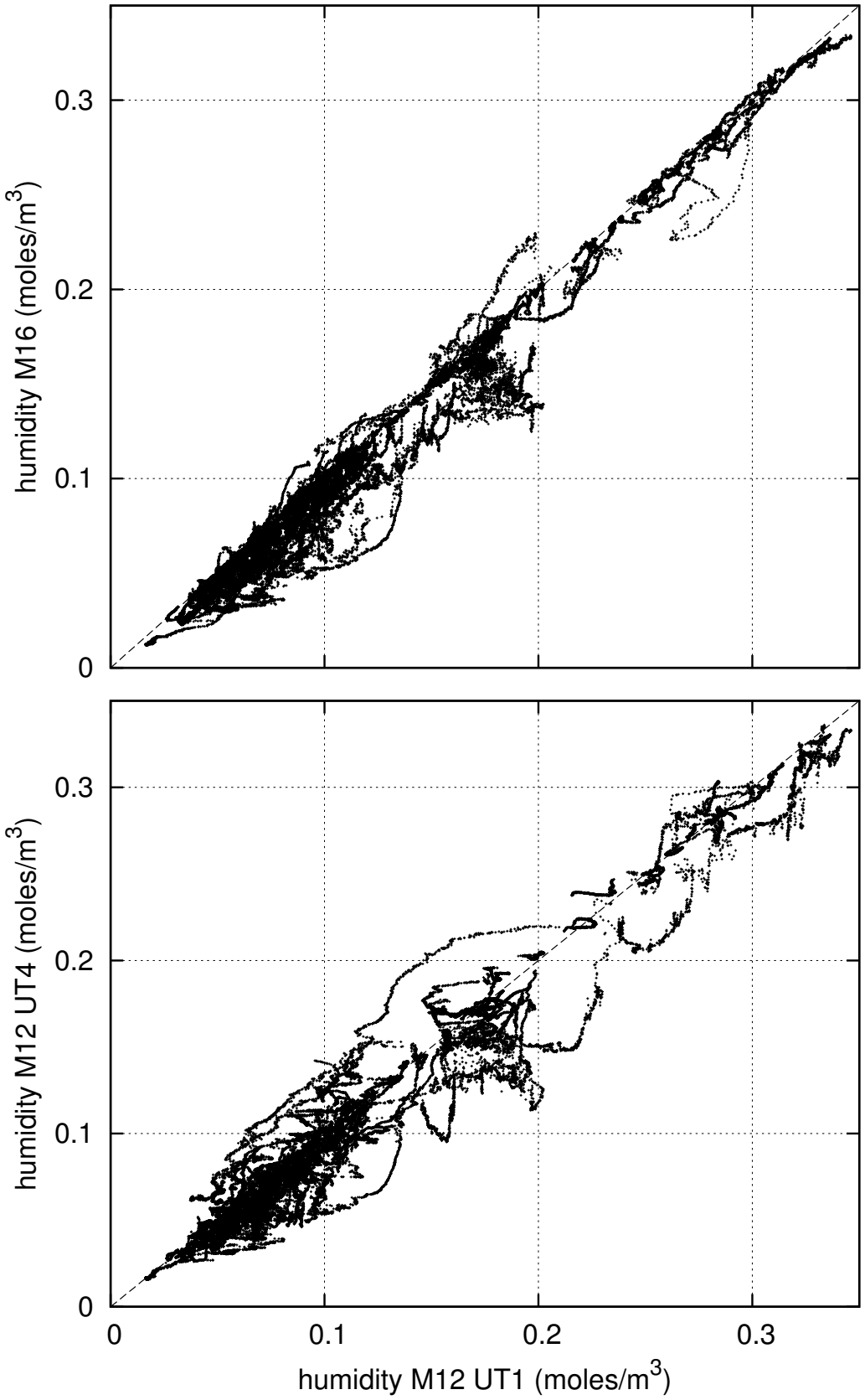

Figure 48: Correlation between the humidity measured at two points inside the DL tunnel and one point in the Interferometric Laboratory, nighttime data between Sep 22, 2004 and Jan 20, 2005.

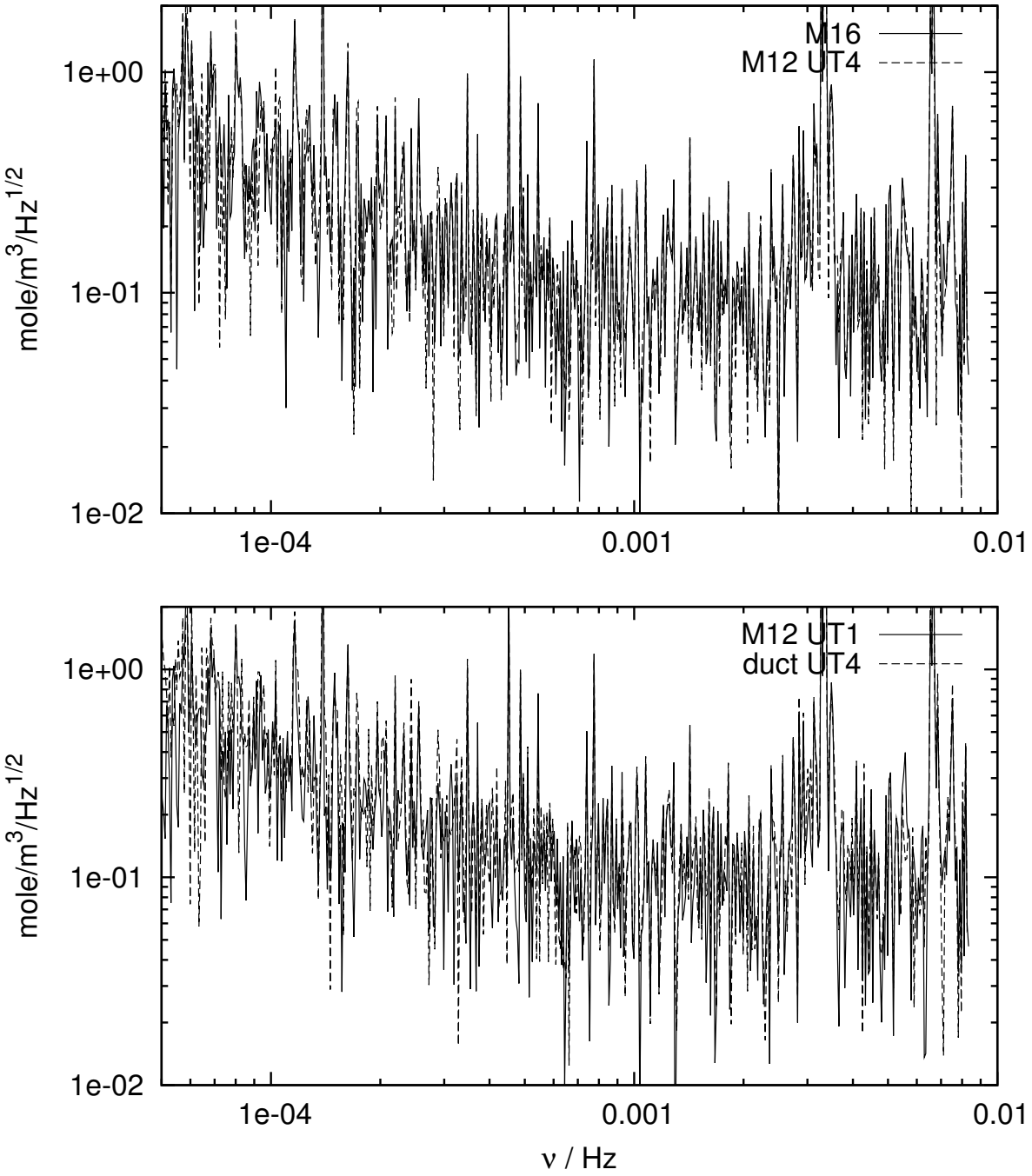

Figure 49: The power spectrum over all nighttime data until July 11, 2006. The sampling period has never been shorter than one minute, which reduces the information in the spectrum to frequencies below the Nyquist frequency of $1/(2*60)$ Hz. Since we are only looking at nighttime data, frequencies below 1/(9 hrs) are not shown either.

6.2 Thermal Loading in the VLTI

The small amplitude of temperature fluctuations in the middle of tunnel and the somewhat larger fluctuations near the M12 of UT1 are plotted in Fig. 50 in comparison to those of the weather pole data. Since the ambient temperatures are not recorded through most of the daytime, it is difficult to assess whether the drift in the tunnel temperature is consistent with a 24hr average of the outdoor temperature. The absolute humidity follows the outdoor pattern more quickly: Fig. 51. In summary (i) the air is exchanged between inside and outside (through the ducts), (ii) the heat capacity of the underground is an efficient absorber of large inertia, (iii) the daytime air-conditioning in the UTs and ATs controls temperatures, but not humidities.

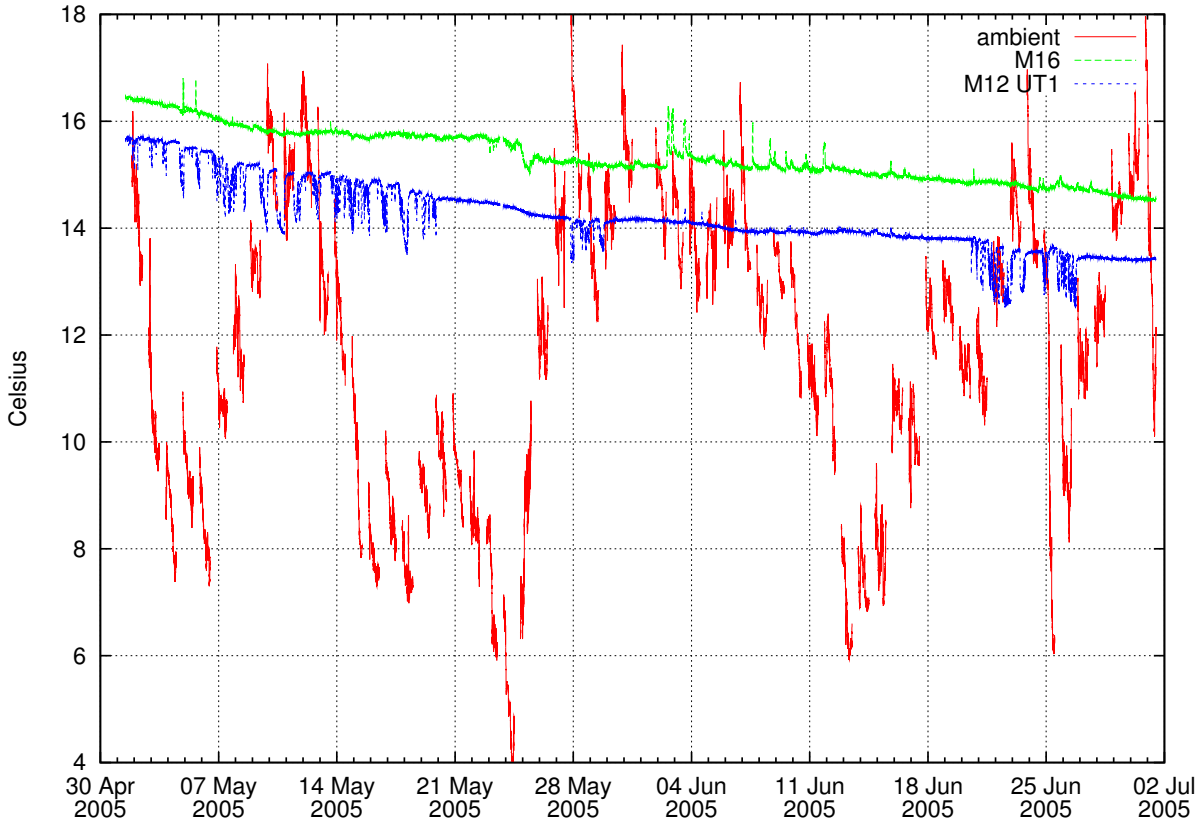

Figure 50: The temperature fluctuations within the VLTI tunnel measured with the GENIE sensors are small compared to those of the ambient temperatures reported from the weather station. The latter are interrupted each day at 12 hrs UT and resume at the beginning of the night, which produces the streaks in the figure.

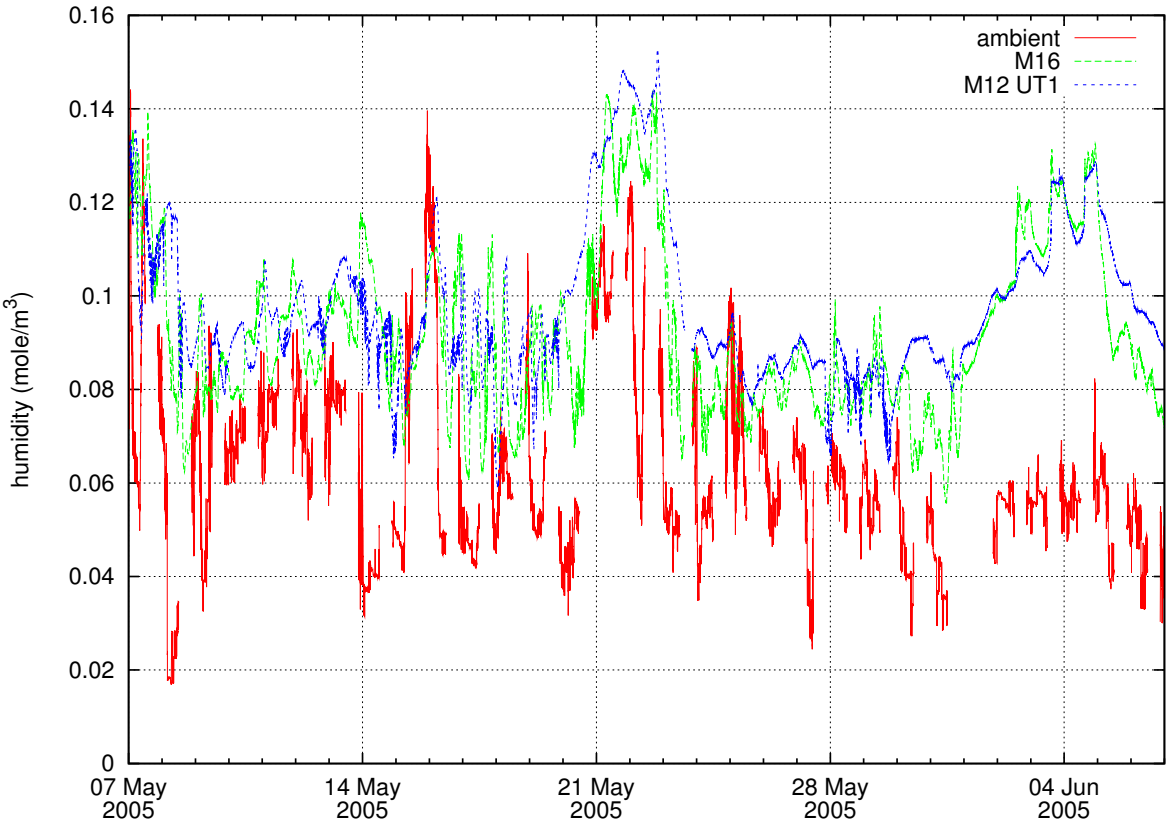

Figure 51: The humidity fluctuations within the VLTI tunnel measured with the GENIE sensors are closer correlated with the data of the weather pole than the temperatures in Fig. 50.

6.3 Tunnel Weather

6.3.1 Encapsulated Volume

From Fig. 3.3.1-3 of [127] the estimated cross section of the tunnel is 7.15×1.84 m^2 = 13.2 m^2, which we multiply by an estimated tunnel length of 158 m (grey area in Fig. 3-2 of [177] between U coordinates of ≈ -32 and $\approx +128$) for a tunnel volume of 2076 m^3. The floor area in the interferometric lab is (Fig. 3.3.1-2 [127]) 20.4×6.7 m^2 at a ceiling height of ≈ 4.9 m (Fig. 3.3.1-3 [127]). This gives 670 m^3 in the interferometric lab. The time needed to replace the total volume once through ducts connecting telescopes and tunnel is shown in Figure 52 [40, 41]. This is obtained by simple division of the volume through the product of duct cross section and wind speed (so neglecting any mixing effects).

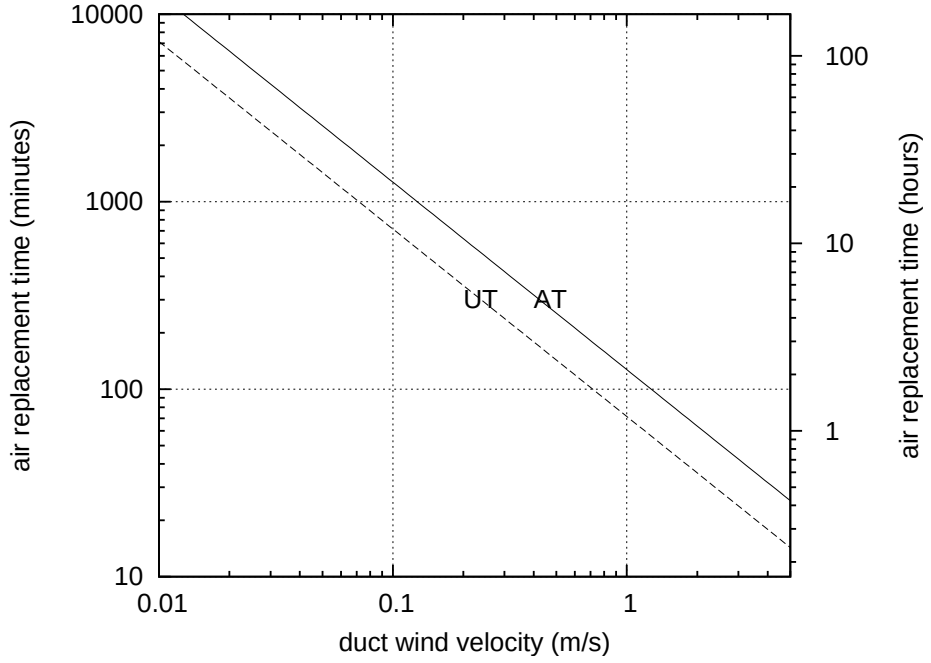

Figure 52: The plot shows the time needed to replace the estimated 2746 m^3 of air volume of the VLTI tunnel and interferometric lab at different speeds of the wind blowing through the 0.6×0.6 m^2 cross section of an AT duct or the 0.8×0.8 m^2 of an UT duct.

The actual time of a change in humidity to arrive in the middle of the DL tunnel was approximately 7 hours during the observation period. This estimate is from Fig. 53,[1] and also follows by building the two FTs of both functions independently, dividing one through the other, and fitting the phase of this product at small frequencies ν to $2\pi\nu\Delta t$ (in short: building the cross-correlation and using the shift-theorem of FTs).

[1] This is not a typical delay; at other occasions this time has been much shorter.

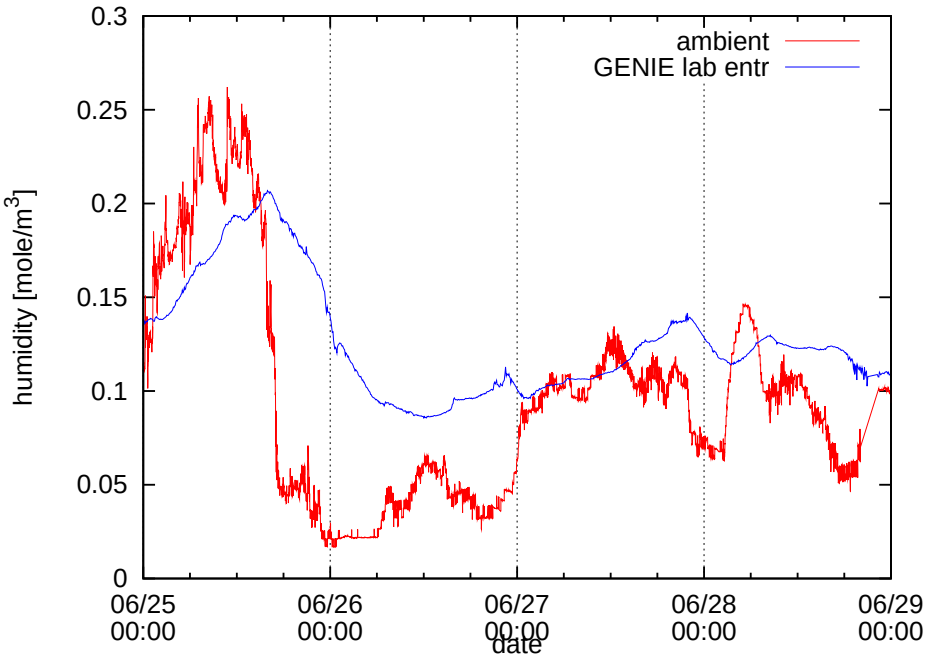

Figure 53: The time delay between a change in the ambient humidity measured at the weather pole (red) and the subsequent change in the humidity measured by a GENIE sensor near the interface of the VLTI tunnel and laboratory (blue) was $\approx$ 7 hours for the four days of the LI-COR campaign [105].

The *temperature* response does not allow a conclusion on the delay. From the data on June 25, the upper two plots of Figure 55, one would conclude that the temperature drop by ≈ 0.2 °C near the interferometric lab occurred 1.5 hrs *before* the drop by ≈ 5 °C at the weather pole. On the contrary, the two lower plots suggest that on June 27 the change of the temperature near the interferometric lab was 3 hrs *after* the change registered at the weather pole. Four daytime hours, one would actually expect that the air through the ducts (unless covered) follows the temperature/humidity profile of the air conditioning within the dome of the corresponding telescope, *not* the profile of the weather tower.

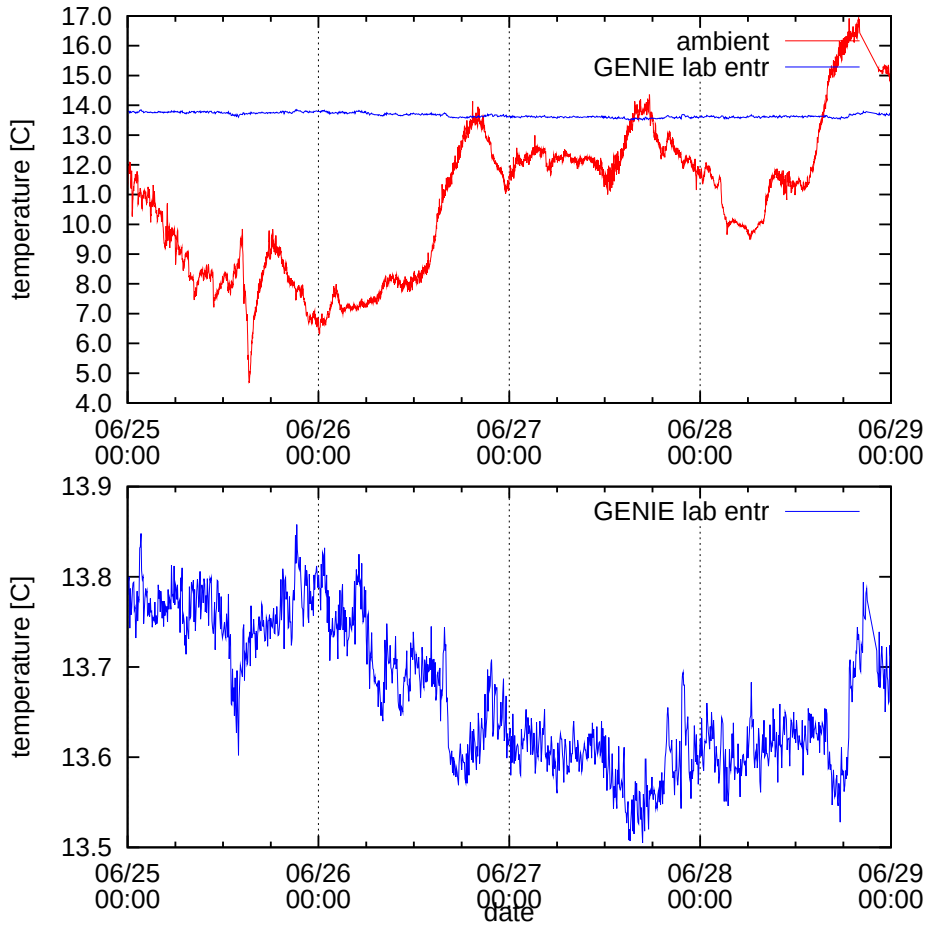

Figure 54: The time delay between a change in the ambient temperature measured at the weather pole (red) and the change in the temperature measured by a GENIE sensor near the interface of the VLTI tunnel and laboratory (blue) during the four days of the campaign. The temperature in the lab is plotted twice, because on a common ordinate scale with the weather pole data (upper plot), changes are miniscule (see also Fig. 50).

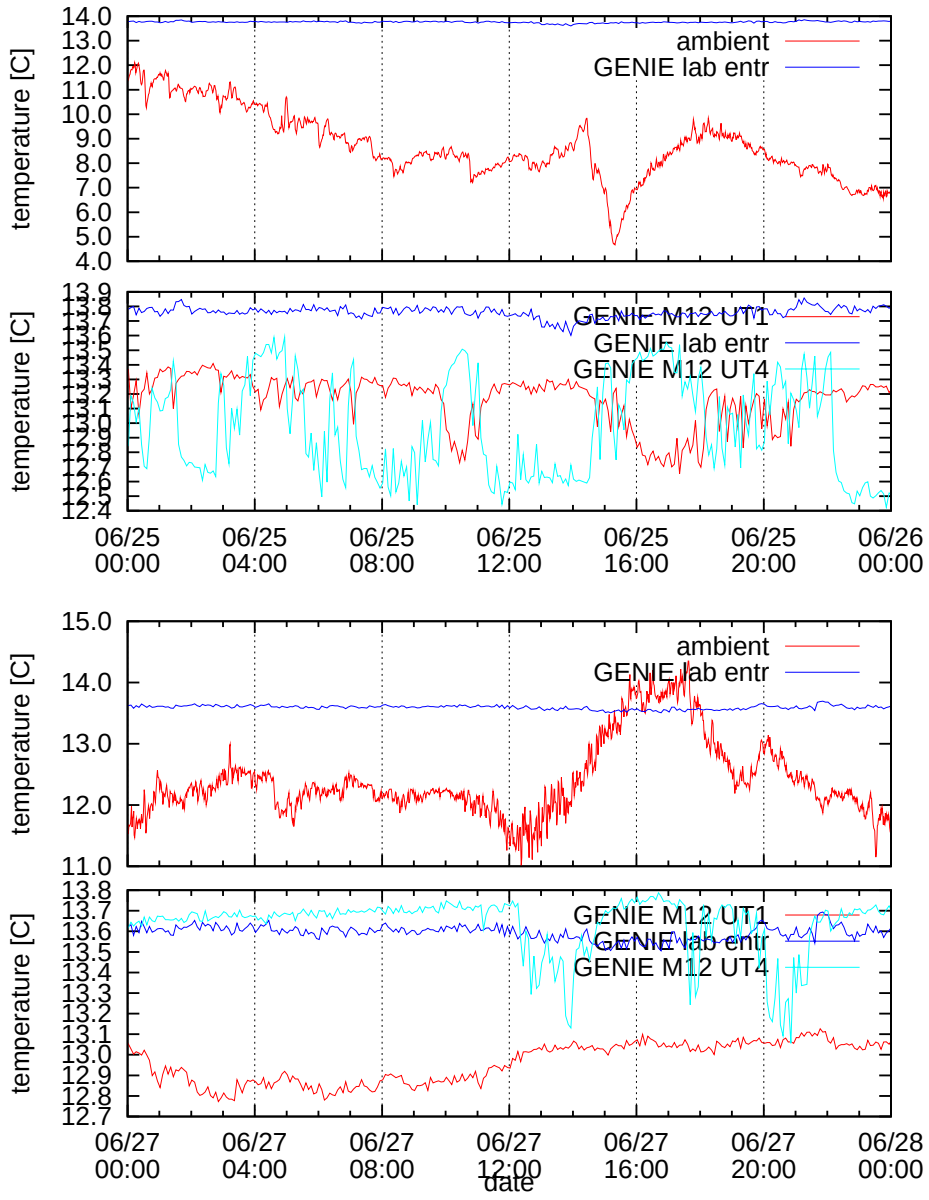

Figure 55: Zoomed into details of Figure 54 for the 25th and 27th of June.

6.3.2 Human Sweat

A human would evaporate at least 35 g water per hour at 18°C [16, M14 Tab 5]; each hour of presence in the DL tunnel of ≈ 2400 m^3 increases the humidity on the average by 0.001 mole/m^3 per human per hour.

6.3.3 Human Carbon Dioxide

At an estimated production of 0.26 liters of carbon dioxide per minute at rest at standard temperature and pressure [23, 45], scaled with 22.4 l/mole, we have 0.012 mol/min per human or 0.70 mole per hour. Distributed over the 2400 m^3, the production is 2.9×10^{-4} mole/m^3 per hour. This is to be rescaled with an air density of 16.2 mole/m^3 at Paranal pressures, and yields 18 ppm, which would be well visible in our curves, Figs. 5 and 22 of [105].

6.3.4 Instrument's Nitrogen Spill

Rumours say some VLTI instruments do not recyle their coolant (liquid Nitrogen) but release it into the laboratory. If this amounts to 50 liters in some time interval (on which we have no further information), we get 40.4 kg at 0.808 kg/l of the liquid, which is 1440 moles from the molecular weight of 28.01 g/mol.

At an average temperature of 16 °C (Fig. 35) and pressure of 743 hPa (Fig. 56), the ideal gas equation yields an air density of 30.5 mol/m^3. At an estimated volume of 670 m^3 in the lab (Section 6.3.1) and 78.1 volume-percent of nitrogen, this sums up to $670 \times 30.5 \times 0.781$ mole $= 15900$ mole of nitrogen in the lab. Supposed one adds the 1440 mole assumed above at constant total air pressure, keeping it within the interferometric laboratory, the partial pressures of the other gases, including Carbon Dioxide, will be reduced. In detail, increasing the nitrogen level from 15900 mole to $15900 + 1440$ mole $= 17340$ mole moves the nitrogen mixing ratio from 0.781 to $0.781 \times 17340/15900 \approx 0.8517$, which means the mixing ratio of the other gases (Oxygen, water, Carbon Dioxide) is reduced from $1 - 0.781 \approx 0.219$ to $1 - 0.8517 \approx 0.1483$, which is a reduction by a factor of $0.1483/0.219 \approx 0.68$. This seems to point at the likely cause for the CO_2 fluctuations in the tunnel shown in Fig. 5 and 22 of [105].

6.4 VLTI Tunnel Pressure

Compared to the fluctuations in temperature and humidity, the density fluctuations (and induced refractivity fluctuations) caused by changes in pressure are small. A statistics is plotted in Fig. 56.

6.5 Water Vapor Scale Height

At a scale height of 2 km$= 2 \times 10^6$ mm, x mm of PWV correspond to a density of $5 \times 10^{-7} x$ relative to the liquid water density on the ground; with a molar mass of $10^3/18.01015$ mol/kg and a specific density of the liquid of 10^3 kg/m^3, this corresponds to $0.0278x$ mol/m^3, which may be compared with the values in Section 6.1.

Typical values for Paranal are from 2 mm in July to 5 mm in February [142]. Weather satellite data are shown in Fig. 57. These are generally not well correlated to the humidity measured on the

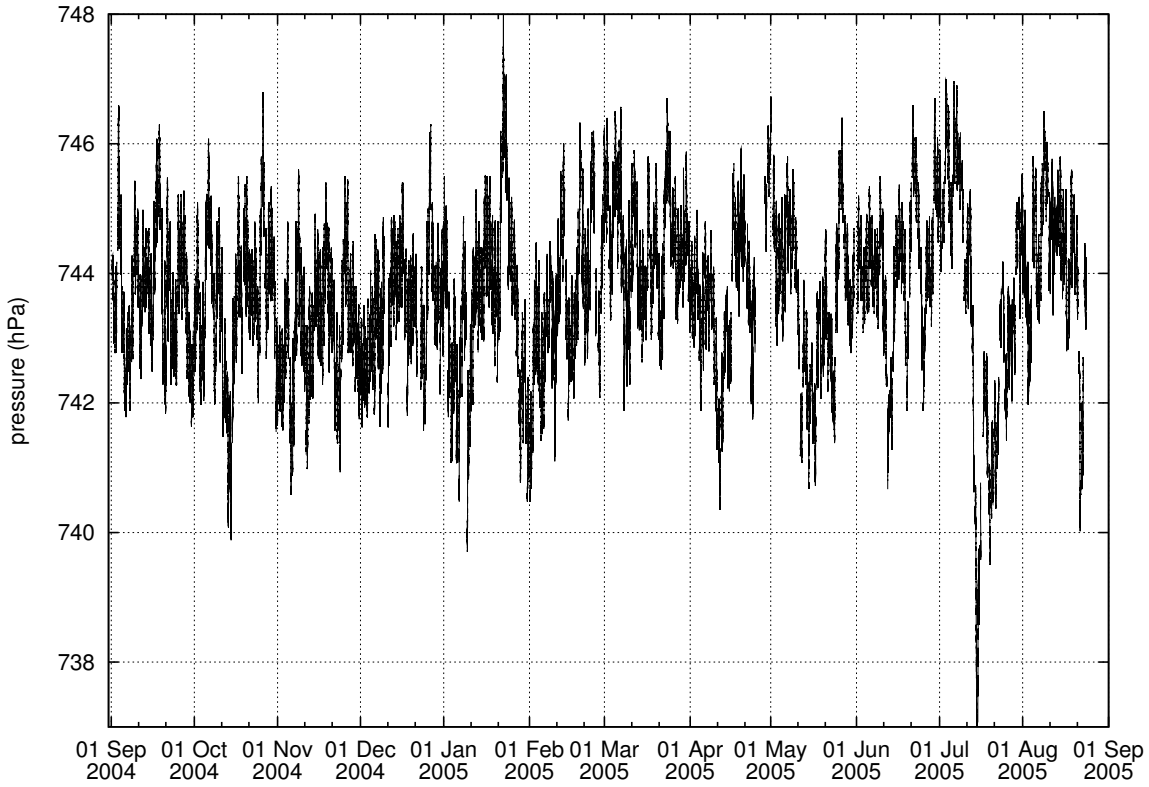

Figure 56: The ambient pressure on Paranal collected by the Paranal weather station over one year.

ground (Fig. 59 and [94]), which means one could not easily extrapolate the water vapor column from the ground data. The mesh size of the satellite rastering inevitably yields a hybrid mix of sea, shore and desert. The simple fit shown in Fig. 59 between the ground humidity and PWV in an exponential scale height model produces a scale height which appears too small. Reasons have been summarized as follows [143]: "*Firstly, exponential decay models assume that water vapour drops at a consistent rate with height. At Paranal, particularly in summer this is not the case. Typically there is a layer of moist air below the inversion and dry air above. So in the first instance when trying to compute PWV from a surface measurement only, cases where the inversion is above the site should be excluded.*

Secondly, it must be born in mind that trying to infer the integrated PWV from one surface meaurement is fraught with uncertainty. The accuracy of such a measurement can hardly be compared to the satellite measurement.

Lastly, within the dry air above the inversion the exponential decay assumption is reasonably valid but the "standard" model would not be applicable since the airmass at Paranal is subtropical. So it is expected that the scale height for the standard atmosphere would not be found. One can probably read up somewhere how the WV scale height in a standard atmosphere compares to a subtropical atmosphere (above the inversion). "

From balloon sounding closer to the Andes [156] at altititudes near 5000 m above sea level one may also (in the sense of statistical evidence poorly) obtain water vapor scale heights of approximately 2 km.

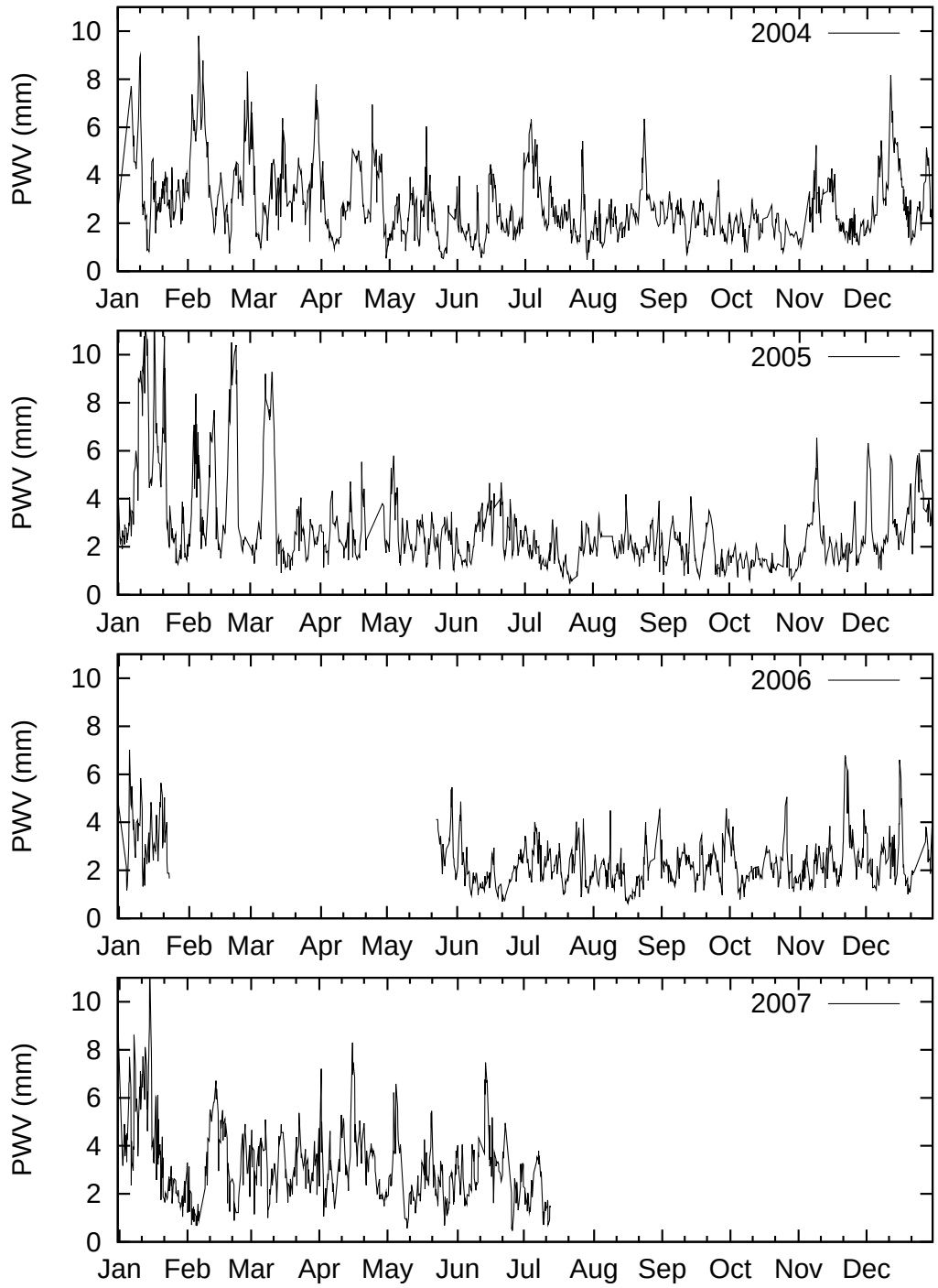

Figure 57: This statistics of the precipitable water vapor on Paranal is plotted from the file `par_fapp.txt` in the bundle `latest_forecasts.tar.gz` available from the ESO web site [71, 142], reduced to data with UTC time stamps of 21, 0, 3 and 6 hrs (at nighttime). The gap of a few months in 2006 occurs because the accumulation of historical data in the file had stopped and a new one had been started, which we did not notice.

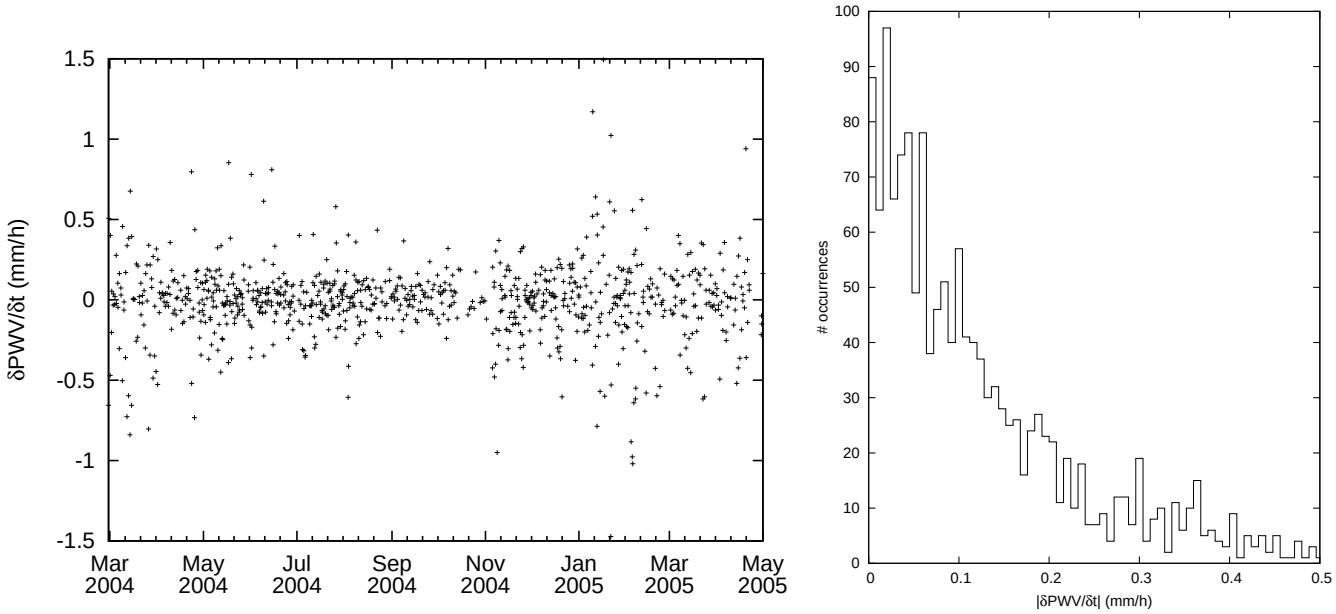

Figure 58: The velocity of the change of the PWV shown here in units of mm per hour is derived from 14 months of Fig. 57 by computing the divided differences of consecutive measurements. Integrating over the counts of the graph at the right, we conclude that the probability of a change slower than 0.16 mm/h is 69.6%, the probability of a change slower than 0.48 mm/h is 95.5%.

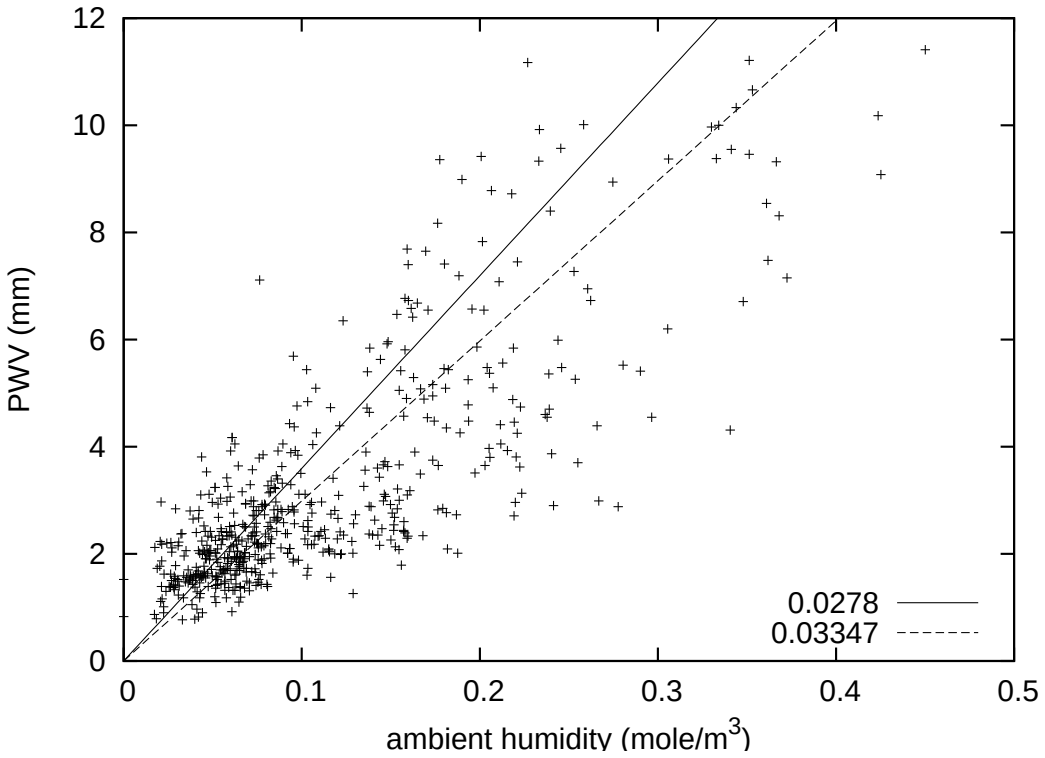

Figure 59: The ambient humidity measured by the weather station is correlated with the PWV data of Fig. 57 for the time between Sep 2004 and Feb 2005. (The satellite data are reported once each three hours and the weather station data not provided from 12 UTC until the evening, which means 5 data points per night are plotted, typically.) The solid straight line demonstrates the factor 0.0278 derived in the text from a 2 km scale height; the dashed is a least squares fit with a factor of 0.03347 which would indicate a scale height of 1.66 km.

6.6 Notations

a	Zernike coefficient
α	molar susceptibility
b, b^*	baseline length (effective length above atmosphere), number of bits
c	speed of light in vacuum
d	beam lateral distance
δ, $\delta_\parallel$, $\delta_\perp$	phase at reflection (for p and s polarization)
D, D_t, $\hat{D}$	OPD (in the tunnel, estimated), with or without factor n
$\Delta(\dots)$	absolute error of…
E	electrical field, photon energy
e	(correlated) spectral energy density
ϵ	dielectric permittivity of the vacuum
$\varepsilon(\dots)$	relative error of …
f, f_w, f_a	molar density (for water and dry air)
F	figure of merit of estimator
G	(tangens of) direction of ∇n relative to beam direction
h	Planck constant
H	(relative) humidity
I	intensity
J_0, K_0	Bessel Functions
k, $\bar{k}$	wave vector modulus, $2\pi/\lambda$, and its mean
k_B	Boltzmann constant
K	scale height (of susceptibility)
l	geometric differential path length
L	geometric path length
λ	wavelength
M	metrology OPD
m_t, m_f	angular magnification factor
n, ∇n, n_g	refractive index, its gradient, group refractive index
N	mirror count
NA	numerical aperture
$\tilde{\nu}$	wave number ($1/\lambda$)
ν	frequency
p	pressure, pupil radius at FSU
ϕ	beam tilt angle
φ, $\hat{\varphi}$	ABCD broadband phase (phase at effective wave number)
P	projected baseline
Ψ	beam tilt angle
r	distance to earth center
R	angle of arrival, molar gas constant, angle of refraction, (amplitude) reflection coefficient
$\mathrm{Re}(\dots)$	real part of …
ρ	earth radius
σ^2	variance
t, t_e	time, detector integration time
T	absolute temperature, (amplitude) transmission coefficient
θ	angle of incidence (towards normal)

ϑ	Zernike phase across pupil
U, V, W	Paranal platform coordinates
ω	angular frequency, $2\pi\nu$
x	direction of beam propagation
X	differential OPD
χ, χ_0	susceptibility (at reference height)
z, z_0, Δz	zenith angle (apparent zenith angle, difference between stations)
Z	baseline angle from earth center

Most data shown in this script have been produced by programs written in C++, some in C or `Maple 9`. Plots have generally created with `gnuplot`, diagrams with `xfig`. The manuscript is typeset with LaTeX.

PRIMA datare  ion

___oOo___